



IntechOpen

Cerium Oxide
Applications and Attributes

Edited by Sher Bahadar Khan and Kalsoom Akhtar



CERIUM OXIDE - APPLICATIONS AND ATTRIBUTES

Edited by **Sher Bahadar Khan**
and **Kalsoom Akhtar**

Cerium Oxide - Applications and Attributes

<http://dx.doi.org/10.5772/intechopen.75239>

Edited by Sher Bahadar Khan and Kalsoom Akhtar

Contributors

Ivana L. Lehr, Silvana Saidman, Ana Paula Loperena, Shobit Omar, Lucian Pîslaru-Dănescu, Gabriela Telipan, Ioana Ion, Virgil Marinescu, Miren Aguirre, María Paulis, Jose R. Leiza, Kai Li, Ji Chen, Dan Zou, Sher Bahadar Khan, Kalsoom Akhtar

© The Editor(s) and the Author(s) 2019

The rights of the editor(s) and the author(s) have been asserted in accordance with the Copyright, Designs and Patents Act 1988. All rights to the book as a whole are reserved by INTECHOPEN LIMITED. The book as a whole (compilation) cannot be reproduced, distributed or used for commercial or non-commercial purposes without INTECHOPEN LIMITED's written permission. Enquiries concerning the use of the book should be directed to INTECHOPEN LIMITED rights and permissions department (permissions@intechopen.com). Violations are liable to prosecution under the governing Copyright Law.



Individual chapters of this publication are distributed under the terms of the Creative Commons Attribution 3.0 Unported License which permits commercial use, distribution and reproduction of the individual chapters, provided the original author(s) and source publication are appropriately acknowledged. If so indicated, certain images may not be included under the Creative Commons license. In such cases users will need to obtain permission from the license holder to reproduce the material. More details and guidelines concerning content reuse and adaptation can be found at <http://www.intechopen.com/copyright-policy.html>.

Notice

Statements and opinions expressed in the chapters are these of the individual contributors and not necessarily those of the editors or publisher. No responsibility is accepted for the accuracy of information contained in the published chapters. The publisher assumes no responsibility for any damage or injury to persons or property arising out of the use of any materials, instructions, methods or ideas contained in the book.

First published in London, United Kingdom, 2019 by IntechOpen

eBook (PDF) Published by IntechOpen, 2019

IntechOpen is the global imprint of INTECHOPEN LIMITED, registered in England and Wales, registration number: 11086078, The Shard, 25th floor, 32 London Bridge Street
London, SE19SG – United Kingdom

Printed in Croatia

British Library Cataloguing-in-Publication Data

A catalogue record for this book is available from the British Library

Additional hard and PDF copies can be obtained from orders@intechopen.com

Cerium Oxide - Applications and Attributes

Edited by Sher Bahadar Khan and Kalsoom Akhtar

p. cm.

Print ISBN 978-1-78985-023-9

Online ISBN 978-1-78985-024-6

eBook (PDF) ISBN 978-1-83881-820-3

We are IntechOpen, the world's leading publisher of Open Access books Built by scientists, for scientists

3,900+

Open access books available

116,000+

International authors and editors

120M+

Downloads

151

Countries delivered to

Our authors are among the
Top 1%

most cited scientists

12.2%

Contributors from top 500 universities



WEB OF SCIENCE™

Selection of our books indexed in the Book Citation Index
in Web of Science™ Core Collection (BKCI)

Interested in publishing with us?
Contact book.department@intechopen.com

Numbers displayed above are based on latest data collected.
For more information visit www.intechopen.com



Meet the editors



Dr. Sher Bahadar Khan received his PhD in chemistry from HEJ, Karachi University, Pakistan. After completion of his PhD, he began his postdoctoral career in nanochemistry and nanotechnology and continued to work as a postdoctoral research fellow until February 2010 at Yonsei University, South Korea. In March 2010, he joined the Center for Advanced Materials and Nano-engineering, Department of Chemistry, Najran University, as an assistant professor and continued his work until August 31, 2011. He joined the Chemistry Department, King Abdulaziz University, Jeddah, Saudi Arabia, as an assistant professor in September 2011. Currently, he is a full professor and conducting research into nanochemistry and nanotechnology, which comprises drug delivery, solar cells, development of active photocatalysts, and fabrication of perceptive biosensors and chemisensors using metal oxide nanomaterials and their green environmental nanohybrids. He is the author of six books, six patents, and 270 research papers with more than 800 impact factors, 4000 citations, and a 35 h-index.

Dr. Kalsoom Akhtar received her PhD from the Chemistry Department, Ewha Womans University, Seoul, Korea. Dr. Akhtar is an assistant professor at the Chemistry Department, King Abdulaziz University, and is conducting research into organic chemistry and nanochemistry, which comprises photocatalysts, organic synthesis, and metal oxide nanomaterials. She is the author of two books and 65 research papers.

Contents

Preface XI

- Chapter 1 **Introductory Chapter: Cerium Oxide - Applications and Attributes 1**
Sher Bahadar Khan and Kalsoom Akhtar
- Chapter 2 **Extraction and Recovery of Cerium from Rare Earth Ore by Solvent Extraction 5**
Kai Li, Ji Chen and Dan Zou
- Chapter 3 **Cerium Oxides for Corrosion Protection of AZ91D Mg Alloy 23**
Ana Paula Loperena, Ivana Leticia Lehr and Silvana Beatriz Saidman
- Chapter 4 **Doped Ceria for Solid Oxide Fuel Cells 43**
Shobit Omar
- Chapter 5 **Prototyping a Gas Sensors Using CeO₂ as a Matrix or Dopant in Oxide Semiconductor Systems 61**
Lucian Pîslaru-Dănescu, Gabriela Telipan, Ioana Ion and Virgil Marinescu
- Chapter 6 **Waterborne Acrylic/CeO₂ Nanocomposites for UV Blocking Clear Coats 95**
Miren Aguirre, María Paulis and Jose R. Leiza

Preface

Cerium oxide (CeO_2), which is one of important transition metal oxides, acts as an n-type semiconductor material. It is clear from the title that this book is related to CeO_2 . CeO_2 has a cubic fluorite structure, in which each cerium atom is surrounded by eight equivalent oxygen atoms and each oxygen atom is surrounded by a tetrahedron of four cerium atoms. CeO_2 has shown various applications, particularly adsorption, catalysis, photocatalysis, sensing, fuel cells, hydrogen production, semiconductor devices, as well as biomedical uses. CeO_2 is also used in petroleum refining and emission controlling systems in gasoline engines, as well as a diesel fuel-borne catalyst to reduce particulate matter emissions. In recent years, CeO_2 nanoparticles have gained greater consideration in the biomedical research community since it can be used as an inhibiting cellular agent along with its antimicrobial and antioxidant activities. Because of the dramatic and widespread industrial uses of CeO_2 materials, it was thought appropriate to present recent developments in the applications and attributes of CeO_2 in the form of a book to the scientific community. This book contains six chapters, which describe the structure, different uses, applications, and attributes of CeO_2 .

The first chapter is “Cerium oxides for corrosion protection of AZ91D Mg alloy” by A. P. Loperena et al. The chapter describes CeO_2 -based coatings as an environmentally friendly option to enhance the corrosion resistance of magnesium alloys. The formation of a coating from a solution containing cerium nitrate was studied for controlling the biodegradation rate of AZ91D magnesium alloy in simulated physiological solution.

The second chapter is “Doped CeO_2 for solid oxide fuel cells” by Shobit Omar. It describes the highlights of various activities regarding doped CeO_2 materials in fuel cell applications and the mechanisms underlying the oxygen-ion conduction process in doped ceria.

The third chapter is “Prototyping a gas sensor using CeO_2 as a matrix or dopant in oxide semiconductor systems” by Lucian Pîslaru-Dănescu et al. In this chapter, two important aspects of using CeO_2 in the field of gas sensors are discussed. First, the use of binary semiconductor oxides $\text{CeO}_2\text{-Y}_2\text{O}_3$ for CO_2 detection in the range of 0–5000 ppm. Second, the use of CeO_2 as a dopant in a hydride composite, consisting of reduced graphene oxide/ ZnO , to increase sensibility in NO_x detection at low concentration in the range of 0–10 ppm.

The fourth chapter is “Waterborne acrylic/ CeO_2 nanocomposites for UV blocking clear coats” by Miren Aguirre et al. In this chapter, the authors describe the UV absorbing capacity of CeO_2 nanoparticles and the film-forming capacity of acrylic polymers. It presents the synthetic route to produce waterborne acrylic/ CeO_2 hybrid nanocomposites for UV absorb-

ing coating applications, which leads to encapsulated morphology of CeO₂ nanoparticles into the polymer particles resulting in lack of agglomeration during film formation. The photoactivity behavior of CeO₂ nanoparticles is also discussed.

The fifth chapter is “Extraction and recovery of cerium from rare earth ore by solvent extraction” by Kai Li et al. The authors describe the solvent extraction and recovery of cerium found in a variety of minerals and present in the highest concentration in light rare earth ores. The main approach used is based on the acid-leaching process of rare earth minerals, which produces the leaching solution as well as high purity CeO₂ products.

The sixth chapter is “Pd-supported catalysts over mixed oxides based on cerium for environmental catalysis purposes” by Victor Ferrer. This chapter presents studies related to the use of CeO₂ as a redox promoter in the oxidation reactions of hydrocarbon and the reduction of nitrogen oxides, which are carried out in catalytic converters installed in vehicles. The study also discusses the improvement of CeO₂ redox properties by the incorporation of elements such as terbium or zirconium in the cerium network, creating a mixed oxide with better performance. Catalytic activity resulting from the CH₄ and CO oxidation reactions and reduction of NO by CO in catalysts using Pd as an active phase are also studied.

Prof. Dr. Sher Bahadar Khan and Prof. Dr. Kalsoom Akhtar

Chemistry Department
Faculty of Science
King Abdulaziz University
Jeddah, Saudi Arabia

Introductory Chapter: Cerium Oxide - Applications and Attributes

Sher Bahadar Khan and Kalsoom Akhtar

Additional information is available at the end of the chapter

<http://dx.doi.org/10.5772/intechopen.82757>

1. Introduction

Cerium belongs to lanthanide series and available most abundantly in the crust of the earth with an average concentration of 50 ppm as a rare earth element. Elemental cerium is a flexible and malleable lustrous metal. Cerium metal is iron-gray in color and is highly reactive. It is also known as a strong oxidizing agent and exists as cerium oxide in association with oxygen atoms. It exists as either cerous (Ce^{3+} , trivalent state) or ceric (Ce^{4+} , tetravalent state) in the form of compounds [1].

It is clear from the title that this book is related to cerium oxide (CeO_2) which is one of the important transition metal oxides acting as n-type semiconductor materials. It possesses several features resulted from the combination of high amount of oxygen in its structure and the facile change between the reduced and oxidized states (Ce^{3+} and Ce^{4+}) [2]. The CeO_2 has cubic fluorite structure, in which each cerium atom is surrounded by eight equivalent oxygen atoms and each oxygen atom is surrounded by a tetrahedron of four cerium atoms. Ideally, CeO_2 should have a formal charge of -2 and distance between oxygen–oxygen atoms should be 2.705 \AA , in which the formal charge of cerium ions is $+4$ [3].

The main unique characteristics of cerium oxide involve a band gap of $3\text{--}3.6 \text{ eV}$, high value of dielectric constant up to $\kappa = 23\text{--}26$, high refractive index of $n: 2.2\text{--}2.8$, and high dielectric strength reached to 2.6 MV cm^{-1} [4]. Such properties qualify cerium oxide-based materials to be employed in various applications, especially when they are in nanosized particles. The cerium oxide is a famous member of nanostructured materials having a wide range of applications. Cerium oxide materials/nanomaterials have been utilized in numerous fields including adsorption, catalysis, photocatalysis, sensing, fuel cells, hydrogen production, semiconductor devices as well as biomedical uses [5–10].

Commercial uses of CeO₂ could be utilized in the pure form or in a concentrated dose as a polishing powder for glasses as well as ophthalmic lenses or precision optics. Cerium oxide is also employed as a glass constituent for preventing solarization and discoloration, particularly in television screens. The CeO₂ contributes in heat-resistant alloy and ceramic coatings. Cerium oxide is also used in petroleum refining and emission controlling system in gasoline engines as well as a diesel fuel-borne catalyst to reduce particulate matter emissions. In recent years, CeO₂ nanoparticles have gained more consideration in biomedical research community since they could be used as inhibiting cellular agent along with their antimicrobial and anti-oxidant activity [1, 5].

Owing to the dramatical and widespread industrial uses of cerium oxide materials, the National Institute of Environmental Health Sciences is suggested and nominated CeO₂ for toxicological characterization because of its limited toxicity data, and a lack of toxicological studies for nanoscale CeO₂. CeO₂, which is one of important transition metal oxides, acts as n-type semiconductor materials that have diverse applications such as adsorption, catalysis, photocatalysis, sensing, fuel cells, hydrogen production, semiconductor devices as well as biomedical uses.

Author details

Sher Bahadar Khan^{1,2*} and Kalsoom Akhtar¹

*Address all correspondence to: sbkhan@kau.edu.sa

1 Chemistry Department, Faculty of Science, King Abdulaziz University, Jeddah, Saudi Arabia

2 Center of Excellence for Advanced Materials Research (CEAMR), King Abdulaziz University, Jeddah, Saudi Arabia

References

- [1] EPA. Cerium Oxide and Cerium Compounds, Washington, DC, 2009
- [2] Nakagawa K, Tezuka Y, Ohshima T, Katayama M, Ogata T, Sotowa K-I, et al. Formation of cerium carbonate hydroxide and cerium oxide nanostructures by self-assembly of nanoparticles using surfactant template and their catalytic oxidation. *Advanced Powder Technology*. 2016;27:2128-2135
- [3] Arunkumar P, Meena M, Babu KS. A review on cerium oxide-based electrolytes for ITSOFC. *Nanomaterials and Energy*. 2012;1:288-305
- [4] Vangelista S, Piagge R, Ek S, Sarnet T, Ghidini G, Martella C, et al. Structural, chemical and optical properties of cerium dioxide film prepared by atomic layer deposition on TiN and Si substrates. *Thin Solid Films*. 2017;636:78-84

- [5] Rajeshkumar S, Naik P. Synthesis and biomedical applications of cerium oxide nanoparticles—A review. *Biotechnology Reports*. 2018;**17**:1-5
- [6] Dhall A, Self W. Cerium oxide nanoparticles: A brief review of their synthesis methods and biomedical applications. *Antioxidants*. 2018;**7**:97-109
- [7] Khan SB, Faisal M, Rahman MM, Jamal A. Exploration of CeO₂ nanoparticles as a chemi-sensor and photo-catalyst for environmental applications. *Science of the Total Environment*. 2011;**409**:2987-2992
- [8] Faisal M, Khan SB, Rahman MM, Jamal A, Akhtar K, Abdullah MM. Role of ZnO-CeO₂ nanostructures as a photo-catalyst and chemi-sensor. *Journal of Materials Science & Technology*. 2011;**27**:594-600
- [9] Khan SB, Faisal M, Rahman MM, Akhtar K, Asiri AM, Khan A, et al. Effect of surfactant on the particle size, photocatalytic activity and sensing properties of CeO₂ nanoparticles. *International Journal of Electrochemical Sciences*. 2013;**8**:7284-7297
- [10] Khan SB, Karimov KS, Chani MTS, Asiri AM, Akhtar K, Fatima N. Impedimetric sensing of humidity and temperature using CeO₂-Co₃O₄ nanoparticles in polymer hosts. *Microchimica Acta*. 2015;**182**:2019-2026

Extraction and Recovery of Cerium from Rare Earth Ore by Solvent Extraction

Kai Li, Ji Chen and Dan Zou

Additional information is available at the end of the chapter

<http://dx.doi.org/10.5772/intechopen.79225>

Abstract

Rare earth elements are widely found in many minerals, some of which, such as bastnaesite, monazite, and xenotime, are of great commercial value. Cerium (Ce) is the rare earth element with the highest content in light rare earth ore. Solvent extraction is the most effective and efficient method to recover and separate Ce from other light rare earth elements. After acid leaching of rare earth minerals, leaching solution was obtained, and cerium oxide of products of high purity was obtained by extraction and stripping. It is well known that Ce(IV) can be easily separated from the other RE(III) by adopting the traditional solvent extraction. Based on this principle, the clean process of oxidation roasting and Ce(IV) separation for Sichuan bastnaesite was developed. And then, a preliminary flow sheet of two-step oxidation and extraction of Ce(IV) for Bayan Obo mixed rare earth ores was further proposed.

Keywords: cerium oxide, solvent extraction, rare earth ore, complexation

1. Introduction

Rare earth (RE) elements exist in a variety of minerals, some of which, such as bastnaesite, monazite, and Bayan Obo mixed rare earth ores, are of great significance and commercial value [1–3]. As for the rare earth resources in the world, bastnaesite deposits in China and the United States account for the largest proportion. The carbonatite-hosted bastnaesite deposits at Mountain Pass, the bastnaesite deposits in Sichuan Province, and the large deposits in Bayan Obo area are the most noteworthy deposits. Monazite deposits in Australia, Brazil, China, India, Malaysia, South Africa, Sri Lanka, Thailand, and the United States are the second largest

deposits [4–8]. The Bayan Obo mixed rare earth ores, which is mainly composed of bastnaesite and monazite, is the largest light rare earth resource in the world [3, 9]. The Bayan Obo deposit is actually the tailings of the iron ore processing scheme of Fe-RE-Nb deposit [10, 11].

Cerium (Ce) is the RE element present in the highest concentration in light RE ores, $\text{CeO}_2/\Sigma\text{REO}$ reaches 50% in bastnaesite (REFCO_3), while $\text{CeO}_2/\Sigma\text{REO}$ is approximately as high as 45–50% in monazite (REPO_4) [12]. **Table 1** gives the chemical compositions of different light RE concentrates [12]. Cerium atoms' electronic configuration is $[\text{Xe}]4f^15d^16s^2$. Losing two 6s electrons and one 5d electron, it forms the most common Ce(III). Ce(III) has the tendency to lose electron to become $4f^0$ and forms Ce(IV) [13]. Ce(IV) can exist stably in the aqueous solution because of the lowest standard electrode potential of Ce(IV)/Ce(III) [14]. Ce(IV) exhibits a markedly different chemical behavior compared to other RE(III). The use of the variable valence properties of cerium and its stable structure is of great significance in RE separation [15]. Solvent extraction is reported to be one of the most effective techniques to extract Ce(IV) [16]. When Ce(III) was oxidized into Ce(IV), it can be easily separated from RE(III) because of high separation factor values of Ce(IV) to Th(IV) (>100) and RE(III) (>600) [17].

Compared with other rare earth elements, Ce(IV) has strong complexation and coordination ability because of its small ionic radius [18]. Ce(IV) can form stable complexes with F^- , NO_3^- , HSO_4^- , and H_2PO_4^- in solution, which are easy to be extracted by organic extractants [19–21]. Utilizing complex properties of Ce(IV) with these anions, the recovery of Ce and these associated resources from rare earth ore by solvent extraction can be realized.

A number of extractants such as acidic organophosphorus extractants [22–27], neutral organophosphorus extractants [28–36], amines [37], bifunctional ionic liquid extractants (Bif-ILEs) [38–40], and others [41–48] have been used for the extraction and separation of Ce. When Ce was extracted into organic phase, pure cerium solution can be obtained by stripping, and then cerium products can be obtained by adding ammonium carbonate, oxalic acid, ammonia water, and so on. The high purity cerium oxide can be produced by calcination of these cerium products.

In China, there are three main RE ores, about 80% mixed RE ores in Bayan Obo, 10% bastnaesite in Sichuan and Shandong, and 2.9% ion adsorption ores in South of China. Bayan Obo ores, the largest light rare earth sources in the world, are known as the most refractory rare earth minerals for processing due to the complicated mineral structures and compositions [49]. There are 7–8% fluorine element (F) and 4–6% phosphorus element (P) in Bayan Obo mixed RE ore [15]. The classical process of decomposing mixed RE concentrate by roasting with concentrated sulfuric acid at a high temperature cannot recover F and P, which could cause environmental pollution and waste of resources [50]. Our group proposed a process for Bayan Obo mixed RE

	REO	$\text{CeO}_2/\Sigma\text{REO}$	F	P_2O_5
Bayan Obo mixed ore	60%	50%	7–8%	6–7%
Bastnaesite (Sichuan)	60%	50%	8–10%	
Monazite (Guangdong)	55–65%	45–50%		25–30%

Table 1. Chemical compositions of different light RE concentrates.

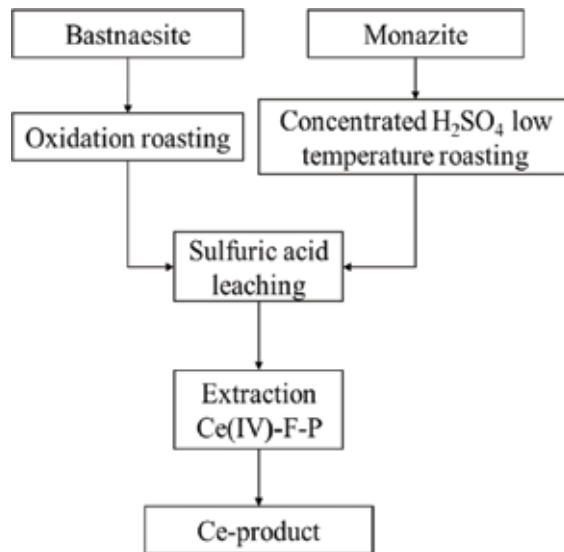


Figure 1. Oxidation and separation of Ce(IV) [18].

ore by utilizing the property of valence change of cerium. The diagram of this process is shown in **Figure 1**. When Ce(III) was oxidized to Ce(IV), F(I) and P can be easily recovered from leaching liquor by solvent extraction in virtue of the complex properties of Ce(IV) with F(I) and P [18]. After extraction, Ce products can be obtained by reductive stripping.

2. Aqueous chemistry of Ce(IV)

2.1. Ce(IV) in aqueous solution

Ce is the only lanthanide element that can form stable molecular complexes in the +4 oxidation state. The stability of the +4 state of cerium is attributed to the $4f^0$ electron configuration [51]. However, much less is known about the properties of Ce(IV) aqueous species than those of Ce(III). For example, the hydration structure of Ce(II) has been extensively studied by many methods [52–58]. In most cases, it is a part of the systematic study of the trivalent rare earth series. In contrast, even for the simplest aqua species of purely hydrated complex, there is little success in the identification of Ce(IV) aqua complexes in solution. In fact, in the scientific literature, Ce(IV) aqua species are often described only as “Ce(IV)” or “Ce(IV) complex,” without specifying their chemical species or composition, simply because of a lack of information [59]. Moreover, because of their high electric charge, Ce(IV) has a strong tendency toward hydrolysis in aqueous solution and undergoes polynucleation or further, leading to colloid formation [60]. Several precedent studies have also implied the formation of soluble polymeric species with oxo- and/or OH-bridging [61]. Based on an extended X-ray absorption fine structure (EXAFS) study and density functional theory (DFT) calculations, Ikeda-Ohno et al. have demonstrated that the Ce(IV) ion in perchloric acid exists in the form of oxo-bridged dimer (**Figure 2**) [59].

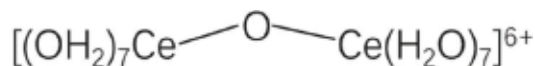


Figure 2. A proposed structure of the cationic dinuclear Ce(IV) species present in perchloric acid.

Using synchrotron X-ray and Raman spectroscopies and EXAFS, Ellis et al. also found that in strong acidic nitrate solution, ammonium ceric nitrate is a dinuclear Ce(IV) complex with a bridging oxo ligand, formulated as $[(\text{H}_2\text{O})_x\text{Ce}^{\text{IV}}-\text{O}-\text{Ce}^{\text{IV}}(\text{OH}_2)_x]^{6+}$ ($x = 6$ or 7) [62]. On the contrary, the present quantum chemical calculations confirm that the Ce^{4+} coordination number is 9 and the relative free energies of Ce^{4+} is the 10- and 8-coordinate isomers in aqueous solutions.

2.2. Ce(IV) complexes with anions in aqueous solution

Ce(IV) is unstable in perchloric acid aqueous solution because its standard electrode potential in perchloric acid aqueous solution is 1.61 V [19]. Therefore, when water decomposes and releases oxygen, Ce(IV) would be slowly reduced to Ce(III). In addition, Ce(IV) is very easy to hydrolyze and polymerize like other tetravalent cations. It is necessary to maintain high acidity in the medium to avoid it. Due to these difficulties, the data of the stability constants of Ce(IV) complexes are very scarce.

Although the studies on nitrate-cerium complexes started earlier, there is contradictory information about these complexes in the relevant literature [63–66]. It was found by potentiometric method that when $[\text{NO}_3^-] < 3.2$ mol/L, there was only one complex in the form of $\text{Ce}(\text{NO}_3)_3^{3+}$ in nitric acid aqueous solution [67]. The other two methods, the spectrophotometry and the extraction method, indicate that the ligand number of nitrate-cerium complexes may vary from 1 to 6. The distribution of Ce(IV) species in aqueous media was studied by measuring the total optical absorbance of Ce(IV) species in different nitric acid-perchloric acid mixture solutions. The stability constants of the nitrate-cerium complexes were determined spectrophotometrically [67].

There are considerable evidences of complex formation between ceric ions and sulfate ions in aqueous solution. Jones et al. have measured the migration in high sulfur concentration solutions and found that the color migrated to the anode. Some researchers [68–70] have measured the electromotive force of the cerium sulfuric acid solution; the results show that a complex is certainly formed, but its nature cannot be determined clearly. Besides, evidence for complexing has been found by Moore et al. [71] from kinetic studies on the reaction of Ce(IV) with arsenite ions. The first complex of Ce(IV) and sulfate in perchloric acid solution was studied by spectroscopic method [72]. The results show that the instability constant of the first complex varies with the concentration of total Ce(IV) ion plus sulfate and a higher complex was also found in this system. Hardwick et al. [73] made a spectral study on the association of Ce(IV) with sulfate. The results show that Ce(IV) interacts with one, two, and three sulfate ions in turn to form complexes. As is expected, as the number of sulfate ions in the complexes increases, the trend of association becomes smaller. Nevertheless, there were no higher complexes of more than three sulfate complexes with Ce(IV).

The stability constants of the fluoride complexes of cerium(IV) in 1 M (HClO_4 , NaClO_4) medium have been measured potentiometrically using a fluoride ion-selective electrode. This procedure ensures the stability of the oxidation state and prevents hydrolysis and polymerization of Ce(IV). Logarithms of the average values of β_1 , β_2 , β_3 , and β_4 were estimated to be 7.57 ± 0.04 , 14.50 ± 0.03 ,

20.13 ± 0.37, and 24.14 ± 0.10, respectively [19]. Besides, in sulfuric acid medium, Qiao studied the complexation behavior of fluorine (I) with Ce(IV). The results show that Ce(IV) and F(I) could form a stable complex in the form of [CeF₂²⁺] and logarithm of the average values of β was 10.67 [20].

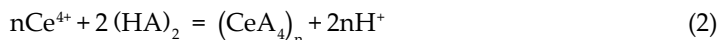
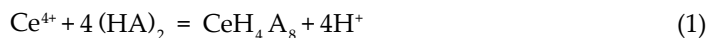
3. Solvent extraction of Ce(IV)

Many extractants have been reported and applied in nitric acid and sulfuric acid for Ce(IV) extraction, for example, acidic organophosphorus extractants [22–27], neutral organophosphorus extractants [28–36], amines [37], and bifunctional ionic liquid extractants (Bif-ILEs) [38–40]. Among them, tributyl phosphate (TBP), di-(2-ethylhexyl) 2-ethylhexyl phosphate (DEHEHP), di-(2-ethylhexyl) phosphate (P204), 2-ethylhexylphosphoric acid mono 2-ethylhexylester (P507), and Cyanex 923 are the most commonly used extractants for Ce(IV) extraction (listed in **Table 2**). Synergistic extraction [26, 35] is also an important method to enhance the extraction efficiency. It was reported that P204 + P507 and P204 + Cyanex 923 had synergistic extraction effects for Ce(IV) extraction from sulfuric acid medium.

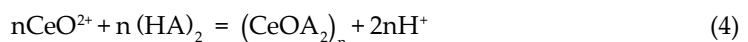
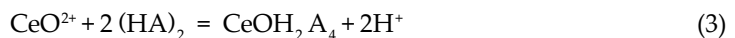
3.1. Acidic organophosphorus extractants

Several acidic organophosphorus extractants [22–27] were used to extract cerium(IV); among these extractants, P204 or P507 is a great extractant for Ce(IV) with a high capacity, extraction efficiency, and selectivity. Peppard et al. studied the extraction of Ce(IV) from HNO₃ solution with P204 in 1957. Tedesco et al. studied the extraction of cerium in kerosene from sulfuric acid solution by di(2-ethylhexyl) phosphate (P204, HA). The effects of DEHPA concentration and pH on the extraction of cerium were determined. However, the mechanism of extraction of Ce(IV) by P204 is not clear. Tedesco et al. considered that the possible extraction mechanism is as follows [22]:

When pH < 1.0



when pH = 1.7–2.0



When the R-O group in dialkyl phosphoric acid molecule is replaced by R group, such as P507, its pKa value increases and its acidity increases. The distribution ratio of rare earth elements extracted by P507 is lower than that of P204. Li et al. [24] have studied the separation of Ce(IV) with P507 in nitric acid system and sulfuric acid system. The mechanism of extraction of Ce(IV) in sulfuric acid system by P507 is as follows:

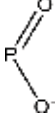
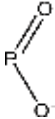
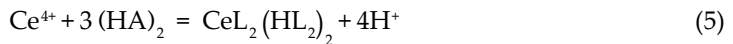
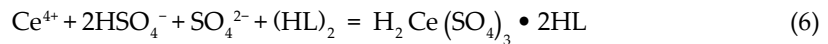
	Extractants	Functional group	Ref.
Neutral organophosphorus	TBP	P=O	[15]
	DEHEHP		[28, 29]
	Cyanex 923		[30–34]
Acidic organophosphorus	P507		[25, 26]
	P204		[23, 24]
Amines	N1923	RNH ₂	[37]
Bif-ILs	[A336][P507]		[39]
	[A336][P204]		[38]

Table 2. The commonly used extractants for Ce(IV) extraction.

Low acidity:



High acidity:



However, it is difficult to extract F⁻ from sulfuric acid solution by P204 and P507 [30]. The addition of boric acid and other masking agents eliminates the effect of F⁻ [74], which would introduce impurities and increase cost.

3.2. Neutral organophosphorus extractants

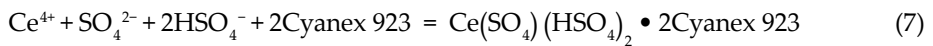
Neutral organophosphorus extractants were applied widely in recently years for Ce(IV) extraction. Tri-butyl-phosphate (TBP) was used to recover Ce(IV) from high acidic HNO₃ solutions by adding an appropriate quantity of H₃BO₃, and high-purity CeO₂ was recovered [75]. However, high extraction acidity and severe co-extraction of mineral acids make TBP extraction of Ce(IV) not superior. Besides, a low extraction efficiency was also a serious problem for Ce(IV) extraction compared with others. Therefore, a new extractant named di-(2-ethylhexyl) 2-ethylhexyl phosphonate (DEHEHP) was used to extract and recover Ce(IV) from HNO₃ solution by Li's group [28, 29]. However, a low extractability and a low loading capacity limit the application of this extractant. In addition, the problem of reduction of cerium(IV) in DEHEHP extraction was also a challenge. Because of its low solubility in aqueous phase, liable hydroxylation, high miscibility with ordinary organic diluents, and low extraction acidities compared to other neutral organophosphorus extractants,

Cyanex 923 (a mixture of straight-chain alkylated phosphine oxides) is considered to be the most used extractant in Ce(IV) extraction [76].

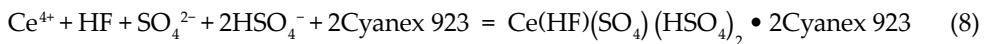
In recent years, our group has used extractant Cyanex 923 to extract and separate Ce(IV) from nitric acid system and sulfuric acid system. Lu et al. [30, 31] studied the extraction and separation of Ce(IV), Th(IV), RE(III), and Fe(III) from sulfuric acid system by Cyanex 923. The experimental results show that the order of extracting metal ions in H₂SO₄ media was Ce(IV) > Th(IV) > RE(III) > Fe(III).

Liao et al. had studied the thermodynamics and kinetics of Cyanex 923 extraction of Ce(IV) from the liquor of bastnaesite in detail. The results showed that Cyanex 923 could effectively extract Ce(IV) from sulfuric acid system. The extraction mechanism was as follows:

Cyanex 923 extracts Ce(IV) from a sulfuric acid solution without fluorine:



Cyanex 923 extracts Ce(IV) from a sulfuric acid solution with fluorine:

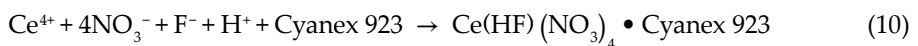


Li et al. studied the extraction and recovery Ce(IV) from nitrate solutions by Cyanex 923. The extraction mechanism was as follows:

Without fluorine:



With fluorine:



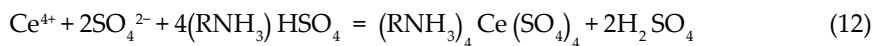
3.3. Amines extractants

The mechanism of extracting Ce(IV) from sulfuric acid solution with primary amine extractant N1923 was studied by Li et al. It was found that the mechanism of extraction of Ce(IV) by N1923 had a great relationship with acidity.

Low acidity:



High acidity:



3.4. Bifunctional ionic liquid extractants

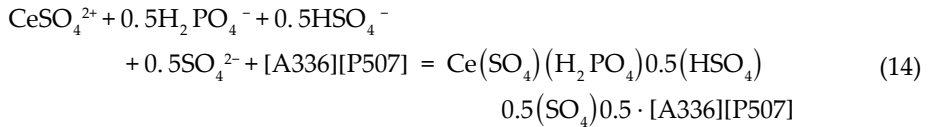
In recent years, quaternary ammonium salts have been widely used in ionic liquids, including surfactants, extractants, catalysis and biodegradation, and many other fields [77–79]. Common ionic liquids are divided into four categories, including imidazole, pyridines, quaternary ammonium salts, and quaternary phosphine salts [80]. Among them, ammonium and phosphorus ionic liquid extractants were investigated in REs separation because of this low price and little toxicity [81]. The neutral complexation mechanism of Bif-IEEs has higher extractability and selectivity, and lower acid and base consumption and no emission of ammonia, nitrogen, Na^+ or Ca^{2+} wastewater.

A series of high purity quaternary ammonium salt ionic liquids ([A336][P507], [A336][P204], [A336][C272]) have been synthesized by Chen's team using the simple and efficient acid-base neutralization method. The synthetic route is given in **Figure 3** [82].

[A336][P507] as shown in **Figure 4** can be used for the separation of Ce(IV) from sulfuric acid solution [39]. Zhang has studied the extraction equilibrium of Ce(IV) from sulfuric acid by using [A336][P507], the extraction mechanism was as follows [39]:



Zhang [21] has investigated the extraction of Ce(IV) in $\text{H}_2\text{SO}_4/\text{H}_3\text{PO}_4$ system [42]. The possible extraction equilibrium is shown in Eq. (5):



3.5. Synergistic extraction system

Synergistic extraction is an important method to enhance the extraction efficiency [26, 35] and has been applied for the extraction and separation of rare earths [83]. Recently, Li et al. have reported the synergistic extraction of lanthanum and Y using a mixture of Cyanex 272(BTMPPA) and 1-phenyl-3-methyl-4-benzoyl-pyrazolone-5 (HPMBP) [84]. Sun et al.

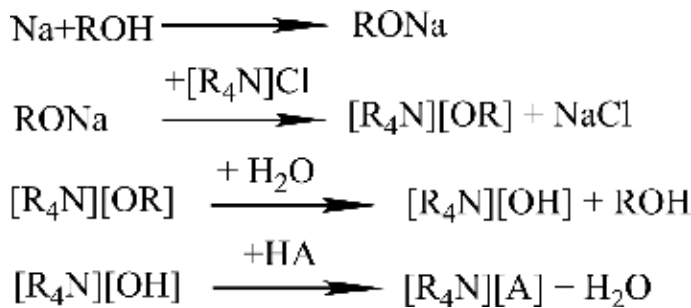


Figure 3. Synthesis route of quaternary ammonium salt bifunctional ionic liquid extractant [82].

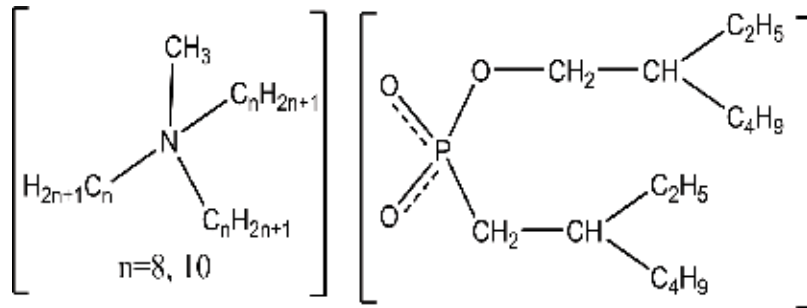
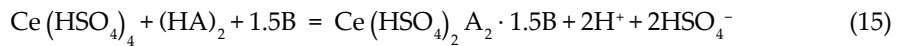


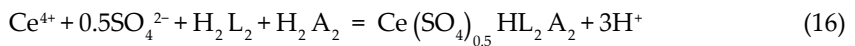
Figure 4. Chemical structures of [A336][P507].

have found the enhanced extraction and separation of yttrium from heavy rare earth using BTMPPA (Cyanex 272) and bis(2,4,4- three methyl amyl) phosphoric acid (CA-12) [85]. In addition, Reddy et al. have studied the synergistic extraction of rare earth elements by Cyanex 923 and Cyanex 301 [86]. These findings have contributed to the study of a new mixed system using Cyanex 923 as an extractant to recover Ce(IV).

Li et al. [35, 36] reported the extraction of Cyanex 923 + P204 for Ce(IV) in sulfuric acid system. The experimental results show that Cyanex 923 + P204 has a positive correlation with the extraction of Ce(IV) solution. The largest synergistic coefficient of Ce(IV) is obtained at the mole fraction $X_{\text{Cyanex 923}} = 0.8$. The synergistic enhancement coefficients (R_{max}) obtained for Ce(IV) are 23.12 in Ce(IV) solution. The synergistic extraction can be expressed as



The synergistic extraction of cerium(IV) from sulfuric acid medium using a mixture of 2-ethylhexyl phosphoric acid mono 2-ethylhexyl ester (HEH/EHP, HL) and Di-(2-ethyl hexyl) phosphoric acid (HDEHP, HA) as extractants was studied [26]. The results showed that HEH/EHP = 0.6 was extracted as an organic phase in the form of $\text{Ce}(\text{SO}_4)0.5\text{HL}_2\text{A}_2$. The synergistic extraction reaction is as follows:



4. Preparation of Ce product

Cerium and its compounds are widely used in many fields. For example, monocrystalline CeO_2 due to its excellent redox ability has an important application value in the fields of CO catalytic oxidation, organic synthesis catalysis, photocatalysis, biological oxidation resistance, and so on. Generally speaking, the preparation of Ce products can be divided into two main methods: one is the sulfuric acid double salt precipitation method and the other is the method of solvent extraction. The process of sulfuric acid double salt precipitation is as follows:

Sulfuric acid rare earth solution containing Ce(IV) → reduces Ce⁴⁺ to form Ce³⁺ → NaOH base decomposition → HCl solubilization → Oxalic acid precipitation → Calcination.

However, the process of this method is long; there are many steps of solid-liquid separation, the yield of rare earth is low (65–67%) and the purity of CeO₂ product is low (95–99%). In addition, the associated resources such as F, P, and Th in sulfuric acid leach liquor were not recovered effectively, resulting in waste of resources and radioactive pollution. In contrast, however, solvent extraction has many advantages. The loaded organic phases could be used to prepare nano-size CeF₃ and CePO₄ by reductive stripping.

Our group developed a method to prepare high-purity CeF₃ nano-powder. This method was to extract from the sulfuric acid liquor of bastnaesite to obtain the loaded organic phase firstly, and then the CeF₃ can be obtained by reduction stripping used H₂O₂. The purity of CeO₂ can be reached to 99.99% [87]. The preparation of CePO₄ nanoparticle was also invented by our group. This method was to extract Ce(IV) by [A336][P507] in H₂SO₄/H₃PO₄ system, and then the CePO₄ can be obtained by reduction stripping also using H₂O₂ [26].

5. Conclusions and outlook

Based on the introduction of solution chemistry and extraction chemistry of cerium(IV) and preparation of cerium products, the mechanism, methods, and objectives of extraction and recovery of cerium from rare earth ore are described in detail in this chapter. It is of great significance to make use of the changeable valence properties and the strong complexation and coordination ability of Ce⁴⁺ in REs separation. The cerium in rare earth ores can be efficiently oxidized to Ce(IV) and can be separated and recovered by solvent extraction easily. According to these studies, Li and our group established an important process to recover Ce(IV) by Cyanex 923 from rare earth ore. The Ce(III) in rare earth ore can be effectively oxidized into Ce(IV) by oxidizing roasting Baotou mixed rare earth ore. The complexation property between Ce(IV) with F and/or P in acidic solution can help to separate and recover Ce(IV), F, and P by solvent extraction. This invention can realize the comprehensive utilization of resources and avoid resource waste and environmental pollution by utilizing the associated resources of the Baotou rare earth ore to recover the Ce. It also provides a convenient condition for the subsequent separation of Th and other RE(III). More efforts on the studies of mechanism, process intensification, and equipment will be needed in the future.

Author details

Kai Li^{1,2}, Ji Chen^{1*} and Dan Zou¹

*Address all correspondence to: jchen@ciac.jl.cn

1 State Key Laboratory of Rare Earth Resources Utilization, Changchun Institute of Applied Chemistry, Chinese Academy of Sciences, Changchun, PR China

2 University of Science and Technology of China, Hefei, Anhui, China

References

- [1] Clark AM. Mineralogy of the rare earth element. In: Henderson P, editor. Rare Earth Element Geochemistry. Developments in Geochemistry, Elsevier; 1984. pp. 36-38. DOI: 10.1016/B978-0-444-42148-7.50007-1
- [2] Jordens A, Cheng YP, Waters KE. A review of the beneficiation of rare earth element bearing minerals. Minerals Engineering. 2013;**41**:97-114. DOI: 10.1016/j.mineng.2012.10.017
- [3] Zou D, Chen J, Cui HM, Liu Y, Li DQ. Wet air oxidation and kinetics of Cerium(III) of rare earth hydroxides. Industrial and Engineering Chemistry Research. 2014;**53**:13790-13796. DOI: 10.1021/ie502241t
- [4] Liu YJ. Present state and main task of development of rare earth industry in China. Journal of The Chinese Rare Earth Society. 2008;**25**:257-262. (in Chinese)
- [5] Chi RA, Tian J. Review of weathered rare earth ore. Journal of the Chinese Rare Earth Society. 2007;**25**:641-652. (in Chinese)
- [6] Wang GZ. Current status of rare earths resources development and strategy in China. Si Chuan Rare Earth. 2009;**3**:4-7. (in Chinese)
- [7] Yang R, Wang W, Zhang X, Liu L, Wei H, Bao M, Wang J. A new type of rare earth elements deposit in weathering crust of Permian basalt in western Guizhou. NW China. Journal of Rare Earths. 2008;**26**:753-759. DOI: 10.1016/S1002-0721(08)60177-5
- [8] Xie F, Zhang TA, Dreisinger D. A critical review on solvent extraction of rare earths from aqueous solutions. Minerals Engineering. 2014;**56**:10-28. DOI: 10.1016/j.mineng.2013.10.021
- [9] Wu WY, Bian X, Sun SC, Tu GF. Study on roasting decomposition of mixed rare earth concentrate in CaO-NaCl-CaCl₂. Journal of Rare Earths. 2006;**24**:23-27. DOI: 10.1016/S1002-0721(07)60313-5
- [10] Wu CY. Bayan Obo Controversy: Carbonatites versus Iron oxide-Cu-Au-(REE-U). Resource Geology. 2008;**58**:348-354. DOI: 10.1111/j.1751-3928.2008.00069.x
- [11] Zhang J, Edwards C. A review of rare earth mineral processing technology. In: Proceedings of 44th Annual Meeting of the Canadian Mineral Processors; Ottawa, Ontario, Canada; January 17-19, 2012. Ottawa: CIM; 2012. pp. 79-102
- [12] Xu GX. Rare Earths. Metallurgical Industry Press: Beijing; 1995. p. 401
- [13] Firor RL, Seff K. Europium (IV), a new oxidation state for europium. Crystal structure of dehydrated europium(II)-exchanged sodium zeolite A, Eu_{4.5}Na₃-A, partially oxidized by oxygen. Journal of the American Chemical Society. 1978;**100**:976. DOI: 10.1021/ja00471a056
- [14] Nugent LJ, Baybarz RD, Burnett JL, Ryan JL. Electron-transfer and fd absorption bands of some lanthanide and actinide complexes and the standard (II-III) oxidation potential for each member of the lanthanide and actinide series. The Journal of Physical Chemistry. 1973;**77**:1528. DOI: 10.1021/j100631a011

- [15] Zou D, Chen J, Li DQ. Separation chemistry and clean technique of cerium (IV): A review. *Journal of Rare Earths*. 2014;**32**:681-685. DOI: 10.1016/S1002-0721(14)60125-3
- [16] Kokare BN, Mandhare AM, Anuse MA. Liquid-liquid extraction of cerium (IV) from salicylate media using N-7V-octylaniline in xylene as an extractant. *Journal of the Chilean Chemical Society*. 2010;**55**:431-435. DOI: 10.4067/S0717-97072010000400004
- [17] Zuo Y, Liu Y, Chen J, Li DQ. Extraction and recovery of cerium(IV) along with fluorine(I) from bastnaesite leaching liquor by DEHEHP in $[C_8mim]PF_6$. *Journal of Chemical Technology and Biotechnology*. 2009;**84**:949-956. DOI: 10.1002/jctb.2116
- [18] Li K, Chen J, Zou D. Recovery of fluorine utilizing complex properties of cerium(IV) to obtain high purity CeF_3 by solvent extraction. *Separation and Purification Technology*. 2018;**191**:153-160. DOI: 10.1016/j.seppur.2017.09.010
- [19] Sawant RM, Rastogi RK, Mahajan MA, Chaudhuri NK. Stabilization of tetravalent cerium in perchloric acid medium and measurement of the stability constants of its fluoride complexes using ion selective potentiometry. *Talanta*. 1996;**43**:89. DOI: 10.1016/0039-9140(95)01719-4
- [20] Qiao J, Zhang CR, Liu ZG, Hao XK. Complexation behavior of fluorine (I) with cerium (IV) in solution. *Journal of the Chinese Rare Earth Society*. 1997;**18**:64
- [21] Zhang L, Chen J, Jin WQ, Deng YF, Tian J, Zhang Y. Extraction mechanism of cerium(IV) in H_2SO_4/H_3PO_4 system using bifunctional ionic liquid extractants. *Journal of Rare Earths*. 2013;**19**:1195-1201. DOI: 10.1016/S1002-0721(12)60426-8
- [22] Tedesco PH, De Rumi VB, Quintana JAG. Extraction of tetravalent metals with di(2-ethylhexyl)phosphoric acid-III cerium. *Journal of Inorganic and Nuclear Chemistry*. 1967;**29**:2813-2817. DOI: 10.1016/0022-1902(67)80021-6
- [23] Li DQ, Wang ZH, Zeng GF, Xue ZY. Solvent extraction of Ce(IV) with HEH(EHP) from sulfuric acid solution. *Journal of the Chinese Rare Earth Society*. 1984;**2**:9-18
- [24] Long ZQ, Huang XW, Huang WM, Zhang GC. Ce^{4+} extraction mechanism from rare earth sulfate solution containing fluorine with DEHPA. *Journal of the Chinese Rare Earth Society*. 2000;**18**:18-20
- [25] Zhu ZW, Zhao N, Long ZQ, Li DD, Cui DL, Zhang GC. New environment friendly approach for bastnaesite metallurgic treatment(I): Extraction of tetravalent cerium from sulphuric acid medium with di(2-ethylhexyl)phosphoric acid. *Journal of Rare Earths*. 2005;**23**:178-182
- [26] Luo XH, Huang XW, Zhu ZW, Long ZQ, Liu Y. Synergistic extraction of cerium from sulfuric acid medium using mixture of 2-ethylhexyl phosphoric acid mono 2-ethylhexyl ester and di(2-ethyl hexyl) phosphoric acid as extractant. *Journal of Rare Earths*. 2009;**27**:119-122. DOI: 10.1016/S1002-0721(08)60204-5
- [27] Qiao J, Long ZG, Zhang CR, Hao XK. Process for separating cerium(IV) from the sulfate system containing several components through extracting with 2-ethylhexyl 2-ethyl hexyl phosphoric acid on industrial-scale. *Journal of the Chinese Rare Earth Society*. 1999;**20**:119-123

- [28] Zhao JM, Zuo Y, Li DQ. Extraction and separation of cerium(IV) from nitric acid solutions containing thorium(IV) and rare earths(III) by DEHEHP. *Journal of Alloys and Compounds*. 2004;**74**:438-441. DOI: 10.1016/j.jallcom.2003.11.057
- [29] Zhao JM, Meng SL, Li DQ. Coordination reactions in the extraction of cerium(IV) and fluorine(I) by DEHEHP from mixed nitric acid and hydrofluoric acid solutions. *Solvent Extraction and Ion Exchange*. 2004;**22**:813-831. DOI: 10.1081/SEI-200030288
- [30] Lu J, Wei ZG, Li DQ, Ma GX, Jiang ZC. Recovery of Ce(IV) and Th(IV) from rare earths(III) with Cyanex 923. *Hydrometallurgy*. 1998;**50**:77-87. DOI: 10.1016/S0304-386X(98)00051-6
- [31] Lu J, Li DQ, Jiang ZC. Separation of Ce(IV) and Th(IV) from RE(III) in HNO₃ solution by Cyanex923 extractant. *Acta Metallurgical Sinica (English Letters)*. 1999;**12**:191-197
- [32] Yu GH, Yue ST, Li DQ, Feng YY. Kinetic study of Ce⁴⁺ extraction with Cyanex923. *Journal of Rare Earths*. 2004;**19**:250-254
- [33] Liao WP, Yu GH, Li DQ. Solvent extraction of cerium(IV) and fluorine(I) from sulphuric acid leaching of bastnaesite by Cyanex 923. *Solvent Extraction and Ion Exchange*. 2001;**19**:243-259. DOI: 10.1081/SEI-100102694
- [34] Liao WP, Yu GH, Yue ST, Li DQ. Kinetics of cerium(IV) extraction from H₂SO₄-HF medium with Cyanex 923. *Talanta*. 2002;**56**:613-618. DOI: 10.1016/S0039-9140(01)00627-0
- [35] Zhang ZF, Li HF, Guo FQ, Meng SL, Li DQ. Synergistic extraction and recovery of cerium(IV) and fluorine from sulfuric solutions with Cyanex 923 and di-2-ethylhexyl phosphoric acid. *Separation and Purification Technology*. 2008;**63**:348-352. DOI: 10.1016/j.seppur.2008.05.023
- [36] Zhang ZF, Guo FQ, Meng SL, Jia Q, Li HF, Li DQ. Simultaneous recovery of cerium and fluorine from bastnaesite leach liquor by mixtures of Cyanex 923 and HEH(EHP). *Industrial and Engineering Chemistry Research*. 2010;**49**:6184-6188. DOI: 10.1021/ie9017385
- [37] Li DQ, Wang ZH, Zeng GF. The mechanism of extraction of Ce(IV) from sulfuric acid solution by primary amine N1923. *Journal of Radioanalytical and Nuclear Chemistry*. 1984;**6**:153-160
- [38] Yang HL, Chen J, Zhang DL, Wang W, Cui HM, Liu Y. Kinetics of cerium(IV) and fluoride extraction from sulfuric solutions using bifunctional ionic liquid extractant (Bif-ILE) [A336][P204]. *Transactions of Nonferrous Metals Society of China*. 2014;**24**:1937-1945. DOI: 10.1016/S1003-6326(14)63274-X
- [39] Zhang DL, Wang W, Deng YF, Zhang JP, Zhao H, Chen J. Extraction and recovery of cerium(IV) and fluorine(I) from sulfuric solutions using bifunctional ionic liquid extractants. *Chemical Engineering Journal*. 2012;**179**:19-25. DOI: 10.1016/j.cej.2011.06.021
- [40] Zuo Y, Liu Y, Chen J, Li DQ. The separation of cerium(IV) from nitric acid solutions containing thorium(IV) and lanthanides(III) using pure [C8mim]PF₆ as extracting phase. *Industrial and Engineering Chemistry Research*. 2008;**47**:2349-2355. DOI: 10.1021/ie071486w

- [41] Revanasiddappa HD, Kumar K, TN. Spectrophotometric determination of cerium with leuco xylene cyanol FF. *Analytical Sciences the International Journal of the Japan Society for Analytical Chemistry*. 2002;**18**:1275. DOI: 10.2116/analsci.18.1275
- [42] Dudwadkar NL. Radiochemical separation and purification of Ce from purex high-level waste. *Separation Science and Technology*. 2004;**39**:3143-3150. DOI: 10.1081/SS-200032981
- [43] Shimada A, Yaita T, Narita H. Extraction studies of lanthanide (III) ions with N, N'-dimethyl-N,N'-diphenylpyridine-2,6-dicarboxamide (DMDPhPDA) from nitric acid solutions. *Solvent Extraction and Ion Exchange*. 2004;**22**:147-161. DOI: 10.1081/SEI-120030392
- [44] Agrawal YK, Vora SB, Shah G. Solvent extraction, separation and recovery of lanthanum(III) and cerium(IV) from monazite sand by N-phenylbenzo-18-crown-6 hydroxamic acid. *Indian Journal of Chemistry*. 2005;**44**:497-503
- [45] Singh DK, Singh H, Mathur JN. Extraction of rare earths and yttrium with high molecular weight carboxylic acids. *Hydrometallurgy*. 2006;**81**:174-181. DOI: 10.1016/j.hydromet.2005.12.002
- [46] Agrawal YK. Liquid-liquid extraction, separation, preconcentration, and ICP-AES determination of lanthanum and cerium with n-phenyl-(1,2-methanofullerene c60)61-formohydroxamic acid. *Fullerene Science and Technology*. 2004;**12**:545-570. DOI: 10.1081/FST-200026937
- [47] El-Sweify FH, Kamel MM. Studies on the extraction behavior of Zr(IV), Ce(III), Th(IV) and U(VI) from aqueous solutions of Arsenazo-I with HDEHP, HTTA, TDA and TCMA. *Journal of Radioanalytical and Nuclear Chemistry*. 1996;**207**:369-382. DOI: 10.1007/BF02071242
- [48] Jain VK, Pillai SG, Kanaiya PH. Octafunctionalized calix[4]resorcinarene-N-fenil-acetohydroxamic acid for the separation, preconcentration and transport studies of cerium(IV). *Journal of the Brazilian Chemical Society*. 2006;**17**:1316-1322. DOI: 10.1590/S0103-50532006000700018
- [49] Huang XW, Long ZQ, Wang LS. Technology development for rare earth cleaner hydrometallurgy in China. *Rare Metals*. 2015;**34**:215-222. DOI: 10.1007/s12598-015-0473-x
- [50] Zhu GC, Chi RA, Shi WZ, Xu Z. Chlorination kinetics of fluorine-fixed rare earth concentrate. *Minerals Engineering*. 2003;**16**:671-674. DOI: 10.1016/S0892-6875(03)00129-8
- [51] Cotton S. *Lanthanide and Actinide Chemistry*. Chichester, England: John Wiley and Sons; 2006
- [52] Kanno H, Hiraishi J. Anomalous concentration dependence of the inner-sphere hydration number change in aqueous europium (III) chloride and gadolinium chloride solutions. *The Journal of Physical Chemistry*. 1982;**86**:1488-1490
- [53] Caminiti R, Cucca P. Hydration phenomena in a concentrated aqueous solution of Ce (NO₃)₃. X-ray diffraction and Raman spectroscopy. *Zeitschrift für Naturforschung A*. 1983;**38**:533-539. DOI: 10.1515/zna-1983-0509

- [54] Allen PG, Bucher JJ, Shuh DK. Coordination chemistry of trivalent lanthanide and actinide ions in dilute and concentrated chloride solutions. *Inorganic Chemistry*. 2000;**39**: 595-601. DOI: 10.1021/ic9905953
- [55] Ohta A, Kagi H, Tsuno H. Influence of multi-electron excitation on EXAFS spectroscopy of trivalent rare-earth ions and elucidation of change in hydration number through the series. *American Mineralogist*. 2008;**93**:1384-1392. DOI: 10.2138/am.2008.2628
- [56] Persson I, Angelo P, De Panfilis S. Hydration of lanthanoid (III) ions in aqueous solution and crystalline hydrates studied by EXAFS spectroscopy and crystallography: The myth of the "gadolinium break". *Chemistry – A European Journal*. 2008;**14**:3056-3066. DOI: 10.1002/chem.200701281
- [57] D'Angelo P, Zitolo A, Migliorati V, et al. Revised ionic radii of lanthanoid (III) ions in aqueous solution. *Inorganic Chemistry*. 2011;**50**:4572-4579. DOI: 10.1021/ic200260r
- [58] Ciupka J, Cao-Dolg X, Wiebke J, et al. Computational study of lanthanide (III) hydration. *Physical Chemistry Chemical Physics*. 2010;**12**:13215-13223. DOI: 10.1039/C0CP00639D
- [59] Ikedaohno A, Tsushima S, Hennig C, et al. Dinuclear complexes of tetravalent cerium in an aqueous perchloric acid solution. *Dalton Transactions*. 2012;**41**:7190. DOI: 10.1039/c2dt12406h
- [60] Baes CF Jr, Mesmer RE. *The Hydrolysis of Cations*. New York: Wiley; 1976
- [61] Louwrier KP, Steemers T. Study of hydrolysis of cerium (IV) in perchlorate solution by light scattering. *Inorganic and Nuclear Chemistry Letters*. 1976;**12**:185-189
- [62] Demars TJ, Bera MK, Seifert S, et al. Revisiting the solution structure of ceric ammonium nitrate. *Angewandte Chemie, International Edition*. 2015;**54**:7644-7648. DOI: 10.1002/ange.201502336
- [63] Duke FR, Forist AA. The theory and kinetics of specific oxidation: III. The cerate-2,3-butanediol reaction in nitric acid solution. *Journal of the American Chemical Society*. 1949;**71**:2790-2792. DOI: 10.1021/ja01176a056
- [64] Blaustein BD, Gryder JW. An investigation of the species existing in nitric acid solutions containing cerium (III) and cerium (IV). *Journal of the American Chemical Society*. 1957;**79**:540-547. DOI: 10.1021/ja01560a012
- [65] Krishna B, Tewari KC. Kinetics and mechanism of oxidation of mandelic, DL-malic, and lactic acid by ceric sulphate. *Journal of the Chemical Society*. 1961;**0**:3097-3100. DOI: 10.1039/JR9610003097
- [66] Amjad Z, McAuley A. Metal-ion oxidations in solution. Part 17. The kinetics and mechanism of the oxidation of malonic acid by cerium (IV) in perchloric acid media. *Journal of the Chemical Society Dalton Transactions*. 1977;**3**:304-308
- [67] Bayülken S, Sarac AS. Distribution of Ce (IV) species in HNO₃-HClO₄ media and determination of stability constants of the nitrate complexes. *Turkish Journal of Chemistry*. 1996;**20**(2):111-117

- [68] Kunz AH. The reduction potential of the ceric-cerous electrode. *Journal of the American Chemical Society*. 1931;**53**:98-102. DOI: 10.1021/ja01352a014
- [69] Noyes AA, Garner CS. Strong oxidizing agents in nitric acid solution. I. Oxidation potential of cerous–ceric salts. *Journal of the American Chemical Society*. 1936;**58**:1265-1268. DOI: 10.1021/ja01298a051
- [70] Smith GF, Getz CA. Cerate oxidimetry. *Industrial and Engineering Chemistry, Analytical Edition*. 1938;**10**(4):191-195
- [71] Moore JW, Anderson RC. Kinetics of the reaction of cerium(IV) and arsenic (III) ions. *Journal of the American Chemical Society*. 1944;**66**:1476-1479. DOI: 10.1021/ja01237a017
- [72] Moore RL, Anderson RC. Spectrophotometric studies on cerium (IV) sulfate complex ions. *Journal of the American Chemical Society*. 1945;**67**:167-171. DOI: 10.1021/ja01218a005
- [73] Hardwick TJ, Robertson E. Association of ceric ions with sulphate (a spectral study). *Canadian Journal of Chemistry*. 1951;**29**:828-837. DOI: 10.1139/v51-095
- [74] Huang X W, Zhang G C. A Process of Extracting and Separating Ce from RE-Sulfuric Acid Liquor Containing Fluorine. *China Patent*: CN 95103694.7. 1995
- [75] Hafner L. German patent 2, 633, 115. *Chemical Abstracts*. 1977;**86**:124825t
- [76] Gupta B, Malik P, Deep A. Extraction of uranium, thorium and lanthanides using Cyanex923: Their separations and recovery from monazite. *Journal of Radioanalytical and Nuclear Chemistry*. 2002;**251**:451-456. DOI: 10.1023/A:1014890427073
- [77] Pretti C, Chiappe C, Pieraccini D, Gregori M, Abramo F, Monni G. Acute toxicity of ionic liquids to the zebrafish (*danio rerio*). *Green Chemistry*. 2005;**8**:238-240. DOI: 10.1039/b511554j
- [78] Wilkes JS, Zaworotko MJ. Air and water stable 1-ethyl-3-methylimidazolium based ionic liquids. *Journal of the Chemical Society, Chemical Communications*. 1992;**13**:965-967. DOI: 10.1039/C39920000965
- [79] Liu Y, Guo L, Zhu L, et al. Removal of Cr(III, VI) by quaternary ammonium and quaternary phosphonium ionic liquids functionalized silica materials. *Chemical Engineering Journal*. 2010;**158**:108-114. DOI: 10.1016/j.cej.2009.12.012
- [80] Liu J, Jiang G, Liu J, et al. Application of ionic liquids in analytical chemistry. *Trends in Analytical Chemistry*. 2005;**24**:20-27. DOI: 10.1016/j.trac.2004.09.005
- [81] Liu YH, Chen J, Li DQ. Application and perspective of ionic liquids on rare earths green separation. *Separation Science and Technology*. 2012;**47**:223-232. DOI: 10.1080/01496395.2011.635171
- [82] Sun XQ, Ji Y, Liu Y, Chen J, Li DQ. An engineering purpose preparation strategy for ammonium-type ionic liquid with high purity. *AIChE Journal*. 2010;**56**:989. DOI: doi.org/10.1002/aic.12039

- [83] Sun XB, Wang JP, Li D, Li HF. Synergistic extraction of rare earths by mixture of bis (2, 4, 4-trimethylpentyl) phosphine acid and sec-nonylphenoxy acetic acid. *Separation and Purification Technology*. 2006;**50**(1):30-34. DOI: 10.1016/j.seppur.2005.11.004
- [84] Sun J, Li DQ. Synergistic extraction of rare earths (III) by mixture of BTMPPA and HPMBP. *Chinese Journal of Applied Chemistry*. 1994;**11**:49-53
- [85] Sun XB, Zhao JM, Meng SL, Li DQ. Synergistic extraction and separation of yttrium from heavy rare earths using mixture of sec-octylphenoxy acetic acid and bis (2,4,4-trimethylpentyl) phosphinic acid. *Analytica Chimica Acta*. 2005;**533**(1):83-88. DOI: 10.1016/j.aca.2004.11.005
- [86] Reddy MLP, Bharathi JRB, Peter S, Ramamohan TR. Synergistic extraction of rare earths with bis (2, 4, 4-trimethyl pentyl) dithiophosphinic acid and trialkyl phosphine oxide. *Talanta*. 1999;**50**:79-85. DOI: 10.1016/S0039-9140(99)00106-X
- [87] Li DQ, Li HF, Guo FQ, Zhang ZF. A Method of Preparation of High-Purity CeF₃ Nano Powder. China Patent: CN 200410010618.2; 2004

Cerium Oxides for Corrosion Protection of AZ91D Mg Alloy

Ana Paula Loperena, Ivana Leticia Lehr and
Silvana Beatriz Saidman

Additional information is available at the end of the chapter

<http://dx.doi.org/10.5772/intechopen.79329>

Abstract

Die-cast AZ91D magnesium alloy (8.9 wt.% Al, 0.6 wt.% Zn, 0.2 wt.% Mn, and balance Mg), as novel alternative biodegradable material, has received great attention due to their potential use in biomedical implants. However, their poor corrosion resistance in physiological fluids restricts practical applications. Cerium-based coatings have been studied as an environmental friendly option to enhance the corrosion resistance of magnesium alloys. In order to control the biodegradation rate of AZ91D magnesium alloy in simulated physiological solution, the formation of a coating from a solution containing cerium nitrate ($\text{Ce}(\text{NO}_3)_3$) was studied. The effect of different additives in the treatment solution (ascorbic acid, citric acid, and sodium citrate) on the anticorrosive properties of the coatings was evaluated. The characterization of the coatings was done using electrochemical techniques and SEM/EDS, XRD, and XPS analyses. The corrosion properties were examined in Ringer solution by polarization studies, open circuit measurements, and faradaic impedance spectroscopy. Results showed that the incorporation of additives improves the anticorrosive properties of the Ce-based film. The coating modified with ascorbic acid provides the best corrosion resistance. According to XPS results, the film is mainly composed by Mg oxides or hydroxides and Ce oxides.

Keywords: cerium oxide, corrosion resistance, AZ91D magnesium alloy, coating, physiological solution

1. Introduction

Magnesium and its alloys are biodegradable and biocompatible materials which exhibit an attractive combination of low density and high strength/weight ratio making them ideal candidates for biomedical applications like substitution and generation of tissues [1]. Temporary

implants of biodegradable materials eliminate the need of a second surgery for implant removal since they are destined to corrode and dissolve postoperatively [2]. However, magnesium-based materials present poor corrosion resistance in physiological environments limiting their applications in the biomedical field. AZ91D magnesium alloy is one of the most commonly used materials, and its corrosion resistance depends on the presence of impure elements acting as active cathode on the microstructure [3].

In order to improve the corrosion resistance of magnesium alloys, some environmentally friendly chemical treatments has been developed [4]. Among them, coatings based on rare earth elements appear as a promising system. Cerium has been studied as alternative to generate protective films. Several researches demonstrated that treatments with cerium salts solutions inhibited the metal corrosion. The formation of cerium oxides and hydroxides on the metal surfaces is generally the reason of this inhibition process because it gives rise to a blocking effect and reduces the rate of reduction reactions [1, 5, 6]. It is known that magnesium alloys oxidation is accompanied with the reduction of hydrogen ions as cathodic reaction. This hydrogen discharge promotes the reaction of Ce^{3+} and Ce^{4+} species with OH^- to form insoluble salts of $Ce(OH)_3$ and $Ce(OH)_4$ due to the increase of the pH in the interface between the substrate and the electrolyte solution [7, 8]. On the other hand, it has been reported that dissolved oxygen can promote the oxidation of Ce^{3+} to Ce^{4+} species. Yu et al. have reported that the cerium precipitation reaction could be affected by the presence of oxygen when the pH solution is in the proper range (pH 4–6) [9]. In addition, Yang et al. demonstrated that the presence of oxygen in the cerium solution promotes the anodic formation of CeO_2 which is better for the formation of compact ceria films [10].

It has been showed that the addition of additives in a cerium solution improves the corrosion resistance of magnesium alloys [11]. Scholes et al. show that the addition of H_2O_2 to the cerium solution is intimated and involved in the deposition process. Hydrogen peroxide acts as oxidant agent and when it is added to the conversion solution, Ce^{3+} ions oxidize to Ce^{4+} . Several studies expose a model of the mechanism by which the cerium-based coatings are formed in the presence of H_2O_2 [12–14]. The addition of hydrogen peroxide in the cerium conversion solution promotes the formation of a cerium hydroxide/oxide coating containing mainly Ce(IV) species which are associated with higher degrees of protection. Chen et al. [15] expose that the concentration of H_2O_2 added to the solution has an important role. In adequate concentrations, H_2O_2 can accelerate the conversion reaction in the formation process; however, if the content of the oxidant exceeds some break value, the coating formed will not be protective for the substrate [6]. In addition, it has been demonstrated that the addition of hydrogen peroxide (H_2O_2) to cerium salts solutions leads to the formation of yellow color coatings due to the presence of Ce(IV). Dabalà et al. report that as the amount of H_2O_2 in the cerium conversion solution increases, more intense yellow color of the coating is obtained on the magnesium alloy surface [6].

With the objective to reduce the velocity of corrosion of AZ91D Mg alloy in physiological simulated solution, the generation of cerium-based coatings on AZ91D Mg alloy was studied in this work. The influence of both the presence of additives in the treatment solution and employed technique on the properties of the coatings was evaluated. Electrochemical and

surface analysis techniques such as SEM, EDS, X-ray diffraction, and X-ray photoelectron spectroscopy (XPS) were employed for characterization of the coatings. The anticorrosive performance of the films was investigated in Ringer solution at 37°C by polarization studies, open circuit measurements, and faradaic impedance spectroscopy.

2. Coating formation

All measurements presented in this chapter were obtained using working electrodes prepared from AZ91D magnesium alloys rods embedded in a Teflon holder with an exposed area of 0.070 cm² [16]. The potentials were measured against a saturated Ag/AgCl and a platinum sheet was used as a counter electrode. All chemicals were reagent grade and solutions were made with twice distilled water.

Optimal conversion parameters such as applied potential, pH of the solution, and additives concentrations were determined in order to obtain protective cerium coatings on AZ91D Mg alloy. Potentiodynamic polarization tests in Ringer solution at 37°C were performed to evaluate the corrosion behavior of the electrodes treated in different cerium-based solutions. Thus, the best formation conditions were established.

First, the formation of coating by immersion of AZ91D alloy in a 50 mM Ce(NO₃)₃ solution of pH 4.7 at 50°C under open circuit potential conditions was investigated. After 30 min, a discontinuous and not adherent white coating was obtained on the substrate. Different potentials were applied to the working electrode employing the same electrolyte solution in order to check the effects of polarization. **Figure 1** presents the polarization curves in Ringer solution obtained for cerium coatings synthesized at different potentials on AZ91D alloy. The curve for

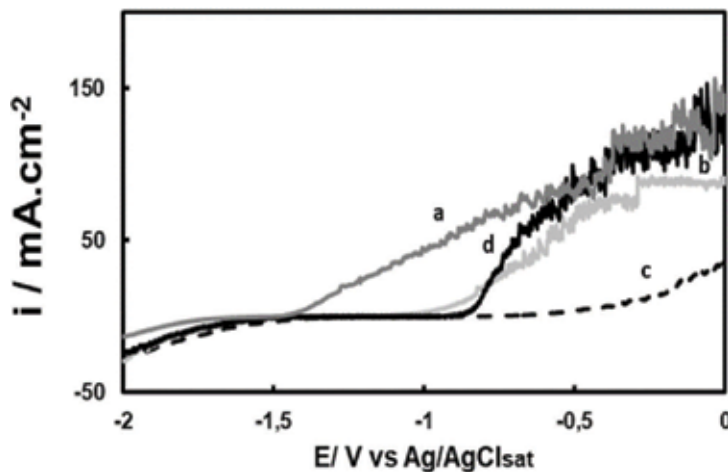


Figure 1. Polarization curves in Ringer solution at 37°C for: (a) AZ91D Mg alloy uncoated and covered with RCe films electrosynthesized in a solution containing 50 mM Ce(NO₃)₃ during 30 min at (b) -0.60 V, (c) -0.75 V, and (d) -0.90 V. The scan rate was 0.001 V s⁻¹.

the bare alloy shows an active dissolution process which starts at -1.478 V (**Figure 1**, curve a). When the substrate is covered by the coating, this process is retarded. The major improvement in corrosion resistance is observed for the film formed at -0.750 V (**Figure 1**, curve c). The corresponding curve exhibits the lowest current densities in the applied potential range. A shift to more positive potentials was also observed indicating that the corrosion reaction of AZ91D alloy is retarded by the presence of the coating. Thus, this potential was selected for further experiments.

Uniform white coatings were obtained on the AZ91D alloy in a 50 mM $\text{Ce}(\text{NO}_3)_3$ solution at -0.75 V during 30 min. For simplicity purposes this film will be called RCe. It has been demonstrated that the use of additives in the treatment solution could improve the anticorrosive performance of the RCe films [11]. Thus, the effect of the addition of different hydrogen peroxide concentrations (1–20 mM) in the cerium-based baths was evaluated. A more uniform film was formed from the solution containing 50 mM $\text{Ce}(\text{NO}_3)_3$, 6 mM H_2O_2 , and pH 3.6. This additive produces the oxidation of Ce^{3+} to Ce^{4+} favoring the incorporation of cerium(IV) in the film [15]. A yellow coating is observed on the substrate after the potentiostatic formation. This coating will be called RCe- H_2O_2 . According to the literature, cerium(IV) is responsible of the appearance of the yellow coating [17], while the presence of Ce_2O_3 or $\text{Ce}(\text{OH})_3$ is related to the white color.

It is known that both Mg and Al are immediately oxidized during immersing of AZ91D alloy in a solution containing $\text{Ce}(\text{NO}_3)_3$ and H_2O_2 . The stable species of Mg in solutions with pH value less than 8.5 is Mg^{2+} while in the case of aluminum is Al^{3+} for solutions with pH value less than 4 [18]. Proton, oxygen, and H_2O_2 reductions can occur simultaneously with the oxidation of the substrate. Based on the experimental conditions of our work, H_2O_2 is the main oxidizing agent, in accordance with the proposition of Yu et al. [9]. Moreover, the addition of H_2O_2 to the treatment solution is necessary for the development of a yellowed coating which is associated with the presence Ce^{4+} species. As was mentioned above, H_2O_2 is a strong oxidizing agent, and its presence in the cerium solution can promote the oxidation which accelerates the precipitation of the conversion coating. On the other hand and, as was stated, the presence of H_2O_2 can produce the oxidation of Ce(III) to Ce(IV). Ce(III) and Ce(IV) species react with OH^- to form insoluble salts of $\text{Ce}(\text{OH})_3$ and $\text{Ce}(\text{OH})_4$ as film components. As the pH in the interface between the substrate and the solution increases as a result of the hydrogen discharge, the precipitation reaction is favored. On the other hand, it has been informed that when H_2O_2 concentration is around 80 mg/L, an increase in the deposition rate of insoluble salts occurs, and in effect, a porous coating is formed on the substrate surface [15]. Thus, the incorporation of a proper amount of H_2O_2 in the treatment bath improves the corrosion performance of Ce-based film on AZ91D alloys.

Polarization curves for the bare alloy and alloy covered with cerium-based coatings are presented in **Figure 2**. In comparison with RCe, a considerable potential shift to more positive values is observed for RCe- H_2O_2 . Thus, the addition of oxidant in the cerium-based bath enhances the corrosion performance of RCe coating.

In order to improve the corrosion resistance of the cerium-based coating obtained in the presence of H_2O_2 , different additives were evaluated. Thus, the inhibition effect of three additives

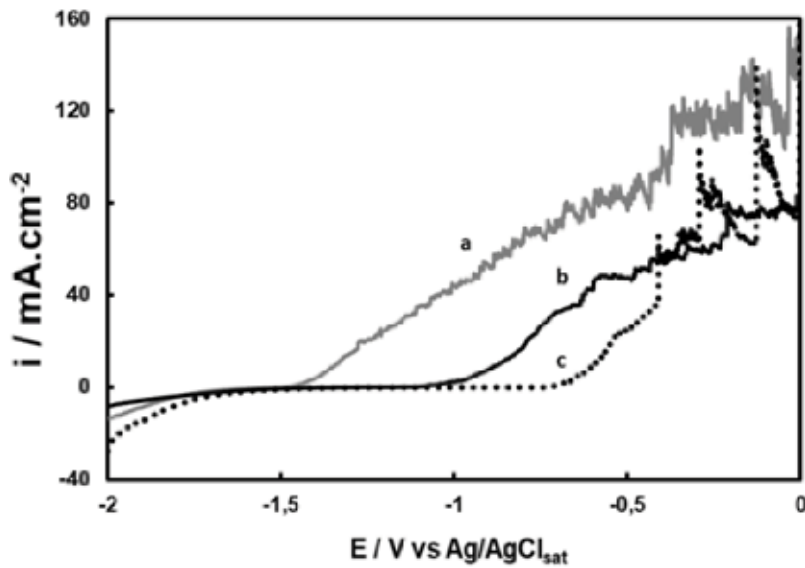


Figure 2. Polarization behavior in Ringer solution at 37°C for: (a) AZ91D Mg alloy, (b) RCe coating, and (c) RCe-H₂O₂ coating. The scan rate was 0.001 Vs⁻¹.

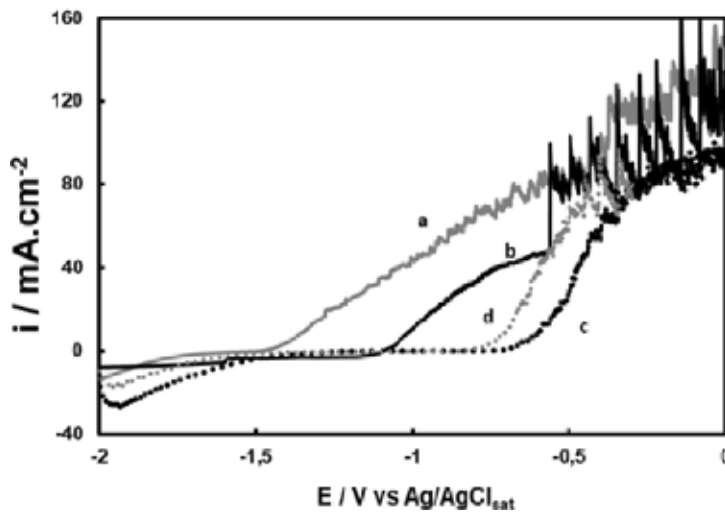


Figure 3. Polarization behavior for AZ91D alloy at 37°C in Ringer solution containing different H₃Cit concentrations: (a) 0 mM, (b) 5 mM, (c) 10 mM, and (d) 15 mM. The scan rate was 0.001 Vs⁻¹.

(citric acid (H₃Cit), ascorbic acid (Hasc), and sodium citrate (Na citrate)) on the electrochemical response of bare AZ91D alloy in Ringer solution was studied. For each additive a range of concentrations was evaluated in order to establish the best conditions to be used in Ce film formation. **Figures 3–5** show the polarization curves of AZ91D magnesium alloy in Ringer solutions containing different additive concentrations. It can be observed that the degradation

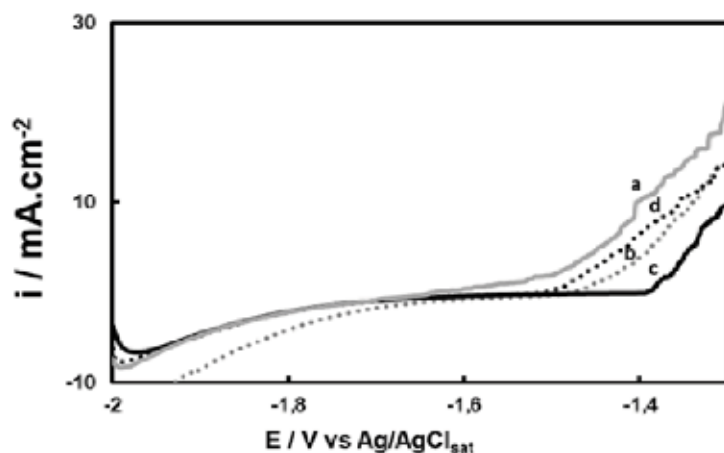


Figure 4. Polarization behavior for AZ91D alloy at 37°C in Ringer solution containing different HAsc concentrations: (a) 0 mM, (b) 1 mM, (c) 5 mM, and (d) 10 mM. The scan rate was 0.001 Vs⁻¹.

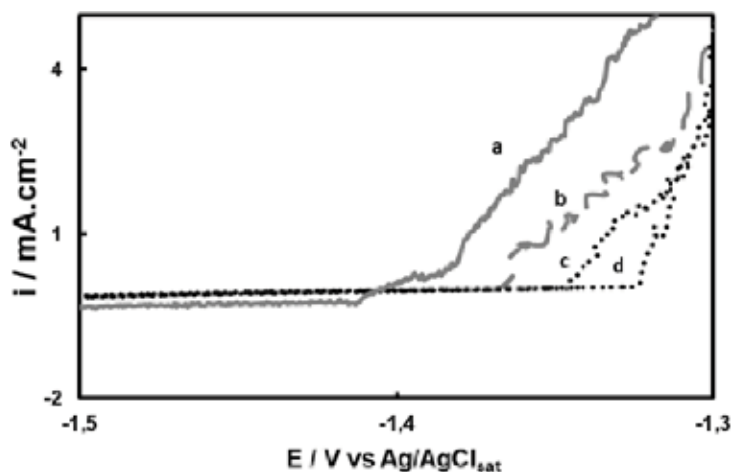


Figure 5. Polarization behavior for AZ91D alloy at 37°C in Ringer solution containing different Na citrate concentrations: (a) 0 mM, (b) 1 mM, (c) 5 mM, and (d) 15 mM. The scan rate was 0.001 Vs⁻¹.

rate of AZ91D alloy is retarded by the presence of the H₃Cit at concentrations up to 10 mM (**Figure 1**, curve c), while the effect is opposite for higher concentrations (**Figure 3**, curve d). Thus, the best inhibitive performance was obtained for 10 mM H₃Cit. A similar procedure was carried out in order to analyze HAsc (**Figure 4**) and Na citrate (**Figure 5**), respectively. The optimum concentration of HAsc was 5 mM (**Figure 4**, curve b), while for Na citrate the best inhibitor effect was obtained for 15 mM (**Figure 5**, curve c).

It is known that compounds with functional groups containing oxygen act as effective corrosion inhibitors for metallic materials in aqueous chloride solution by a surface complex formation [19]. Also, it is known that a chelating agent should have two opposite effects on

the corrosion of metals and may act as either an inhibitor or corrosive [20]. With respect to the effects of H_3Cit , Wang reported that a cerium conversion coating on AZ91 magnesium alloy formed from ethanol solution containing $Ce(NO_3)_3$ and citric acid showed good corrosion performance [17]. The authors postulated that Mg ions originated from the dissolution of the alloy during immersion in the treatment bath reacted with Cit^{3-} and partly deposited on the alloy surface in the form of Mg_3Cit_2 that is insoluble in ethanol. According to the theory of chemical adsorption of organic inhibitors, the chelating agent which forms a stable and insoluble chelate with a metal in certain medium can inhibit corrosion. HAsc is a well-known inhibitor for several metallic materials. The inhibitor character of HAsc has been extensively studied for steel in acid and neutral media [21–23]. Valek et al. reported that the generation of a protective oxide film on steel is associated with the formation of an insoluble surface chelate at an optimal concentration of 10^{-3} M [23]. However, these authors also informed that the formation of a soluble chelate has a stimulatory action in Fe dissolution at concentrations above 5×10^{-3} M. It has been informed that HAsc presents a dual role, in some conditions it can act as corrosion inhibitor, and in other cases, it can increase the corrosion rate of stainless steel (SS) X_4Cr_{13} in HCl solutions [24]. At the present time the inhibition effect of HAsc on the corrosion of magnesium alloys has not been reported. The results obtained here are in accordance with the tendency informed in the bibliography for other metallic materials. So, for an optimal HAsc concentration (5 mM), the precipitation of an insoluble surface chelate confers protection to the magnesium alloy through the formation of a physical barrier. On the other hand, for a HAsc concentration above 5 mM, the degradation rate of AZ91D alloy increases due to the formation of soluble chelates.

It has been demonstrated that sodium citrate can act as brightening, leveling, and buffering agent in electrodeposition electrolytes and, thus, eliminates the need for other additives [25]. Moreover, it is mainly known as a complexing agent. Organic compounds with carboxylate group have been presented as promising corrosion inhibitors of carbon steel in high-alkaline-media-containing chloride ions [26–29]. In addition, citrate ions were presented as good pitting inhibitors, as they could adsorb on the carbon steel (without a passive layer), avoiding chloride ions adsorption due to a steric effect [28]. It has been reported that citrate ions present a chelating effect, forming soluble complexes with Fe(II) and Fe(III) [30]. Bahramian et al. show that sodium citrate proved to be an effective and economical additive to improve the properties of Ni-P coatings obtained on Cu substrate; its impact depended only slightly on its concentration [31]. The effect of Na citrate as corrosion inhibitor in chloride solution was studied for AZ31D and AM60 Mg alloys [32, 33]. It has been demonstrated that Na citrate forms chelates with Mg^{2+} . Although the chelate is soluble, it can be absorbed on the surface of the substrate by the oxygen atom, hindering the adsorption of Cl^- [33].

From the corrosion inhibition behavior shown above, the optimal concentration of each additive for coating formation was selected. Thus, the treatment solutions contain 50 mM $Ce(NO_3)_3$, 6 mM H_2O_2 , and:

- 10 mM H_3Cit . This film will be called RCe- H_3Cit .
- 5 mM HAsc. This film will be called RCe-HAsc.
- 15 mM Na citrate. This film will be called RCe-citrate.

In all cases, a golden-yellow-colored coating was observed with the naked eyes when the substrate was polarized at -0.75 V during 30 min in the treatment solution at 50°C .

3. Evaluation of the anticorrosive properties of the coatings

Polarization measurements in Ringer solution were carried out in order to study the corrosion behavior of the coating formed in the presence of additives (**Figure 6**). A positive potential shift and the low current density measured indicate a better corrosion resistance of the coated samples. In the case of the RCe-HAsc film, a significant increase in the anodic current can be observed at more anodic potential values (**Figure 6**, curve d). It can also be noted that the addition of H_3Cit or Na citrate in the treatment solution does not improve the anticorrosive performance of RCe- H_2O_2 coatings.

Based on the above results, we decided to only study the anticorrosive performance of RCe- H_2O_2 and RCe-HAsc coatings. First, it is important to mention that the RCe coating was very adherent and could be removed only by mechanical polishing. Adherence force of RCe- H_2O_2 and RCe-HAsc was 34.3 and 43.4 N, respectively. Thus, adhesion of the films increases when the additive is added to the treatment solution.

To evaluate the degree of corrosion protection attained after covering the substrate, the variation of the open circuit potential (OCP) as a function of time was carried out in Ringer solution (**Figure 7**). Uncoated sample reaches the pitting potential (-1.503 V) after approximately 5 h of immersion (**Figure 7**, curve a). The electrode covered with the coating obtained without the additive reached the corrosion potential of the uncoated AZ91D alloy after 36 h of immersion (**Figure 7**, curve b). In the case of the coating generated in the presence of the HAsc, at the beginning, the OCP value was -1.320 V (**Figure 7**, curve c). Then, the OCP reached -1.150 V

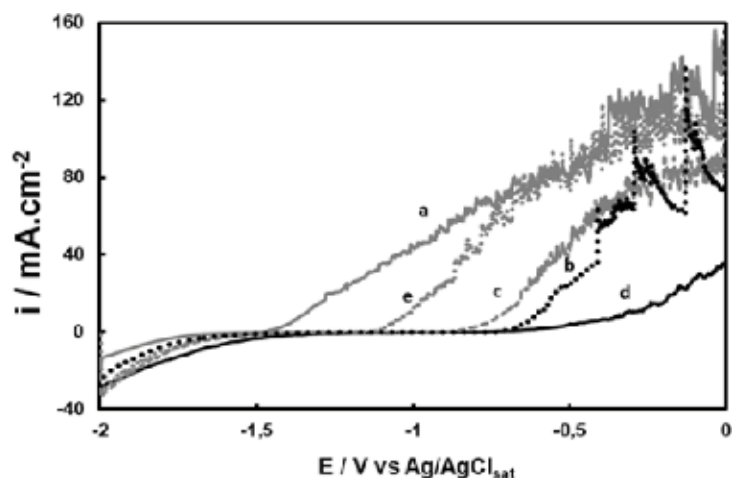


Figure 6. Polarization behavior in Ringer solution at 37°C for: (a) uncoated AZ91D alloy, (b) RCe- H_2O_2 coating, (c) RCe- H_3Cit coating, (d) RCe-HAsc coating, and (e) RCe-citrate coating. The scan rate was 0.001 Vs^{-1} .

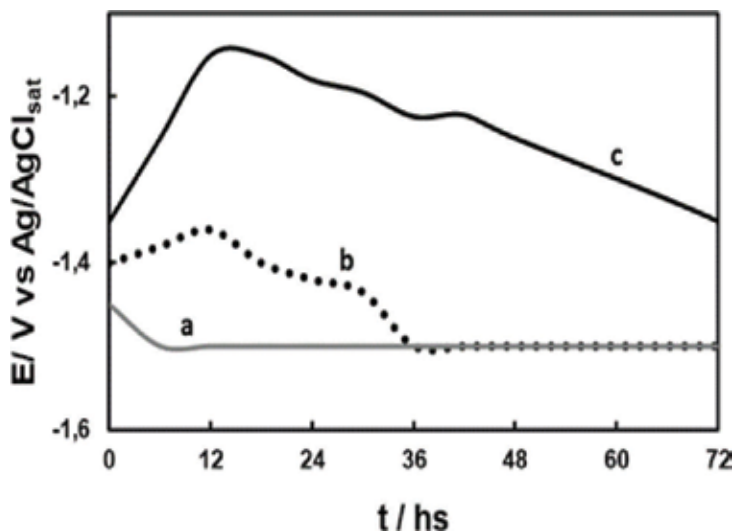


Figure 7. Time dependence of the OCP in Ringer solution for: (a) AZ91D magnesium alloy, (b) RCe-H₂O₂ film, and (c) RCe-HAsc coating.

and kept the same value during 18 h. The OCP was approximately -1.350 V after 72 h of immersion. This potential value was still nobler than that for the uncoated electrode.

Figure 8 shows the Tafel polarization plots for uncoated and coated AZ91D alloy. Estimation of the corrosion parameters (E_{corr} , cathodic (B_c) and anodic (B_a) Tafel slopes and corrosion current (i_{corr}) is reported in **Table 1** for RCe-H₂O₂ and RCe-HAsc coatings. The i_{corr} values measured for the coatings are lower than that for the bare AZ91D alloy. In the case of treated samples, the i_{corr} value is one order of magnitude lower than that of the uncoated substrate. However, higher displacement of E_{corr} to more noble potentials was obtained for the RCe-HAsc film compared to RCe-H₂O₂ coating (**Table 1**).

To obtain more information about the anticorrosion protection of RCe-H₂O₂ and RCe-HAsc film, EIS measurements were conducted in Ringer solution (**Figure 9**). For comparison, the impedance response of uncoated substrate was also presented in **Figure 9**, curve a. Two capacitive loops and one inductive loop were observed in the Nyquist diagram of the AZ91D Mg alloy as was observed for other magnesium alloys [34]. It has been postulated that relaxation processes of adsorbed species ($\text{Mg}(\text{OH})^+$ or $\text{Mg}(\text{OH})_2$) on the surface of untreated alloys/pure Mg leads to an inductive response at low frequencies [35]. After 5 min of immersion, the impedance response for the coated electrodes exhibit two capacitive loops in the high- and low-frequency ranges. It is known that the diameter of the capacitive loops is associated with the charge-transfer resistance (R_{ct}) and therefore with the corrosion resistance. The R_{ct} values for RCe-HAsc coating are much larger than that of RCe-H₂O₂ film indicating a better corrosion protection.

The performance of the RCe-HAsc at different immersion times in Ringer solution was analyzed by Nyquist plots (**Figure 10**). After 6 h of immersion, all the impedance diagrams

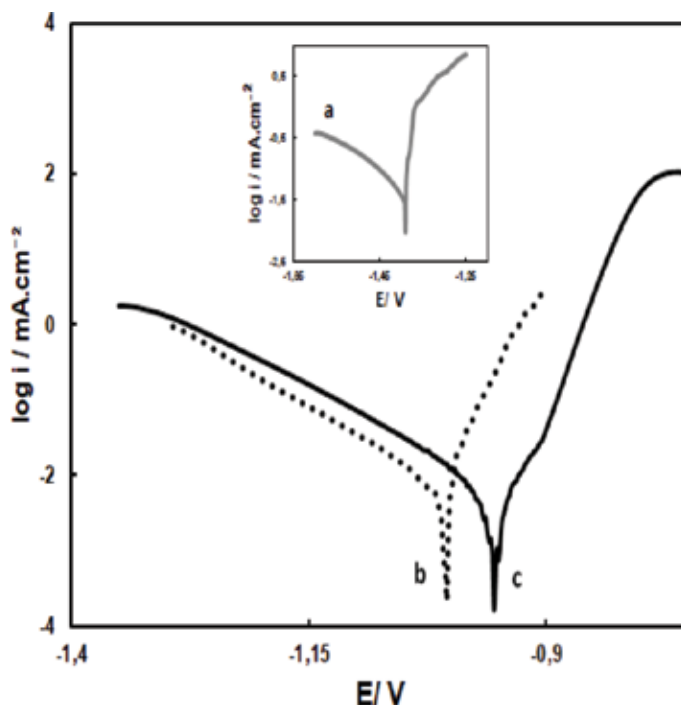


Figure 8. Tafel curves obtained in Ringer solution at 37°C for: (a) uncoated AZ91D alloy, (b) RCe-H₂O₂, and (c) RCe-HAsc. The scan rate was 0.001 Vs⁻¹.

	E_{corr}/V	$i_{\text{corr}}/mAc\text{m}^{-2}$	B_a/V	B_c/V
AZ91D	-1.501 ± 0.050	0.1050 ± 0.0050	0.045	-0.293
RCe-H ₂ O ₂	-1.002 ± 0.020	0.0057 ± 0.0002	0.034	-0.122
RCe-HAsc	-0.952 ± 0.015	0.0054 ± 0.0002	0.032	-0.126

The mean values and their standard deviation are presented.

Table 1. Corrosion parameters estimated from Tafel polarization plots for uncoated AZ91D, RCe-H₂O₂, and RCe-HAsc formed on AZ91D alloy.

exhibit a capacitive loop in the high- and medium-frequency ranges. As can be observed, the diameter of capacitive loop increases gradually with increasing time until 36 h, indicating an improvement in the anticorrosion performance of the coating with time. This result corroborates that the RCe-HAsc can effectively improve the corrosion resistance of the alloy.

In order to confirm the improvement in the corrosion protection of the AZ91D alloy imparted by the RCe-HAsc film, the quantity of Mg released in Ringer solutions after 5 h of immersion under open circuit potential conditions was determined. When the substrate was covered with the RCe-HAsc coating, the amount of Mg released was 2.01 mg/L and for the uncoated sample the value was 3.90 mg/L. So the corrosion rate is nearly twice less for the sample coated by the RCe-HAsc film. This result confirms a good performance of the RCe-HAsc coating even after a long exposure time.

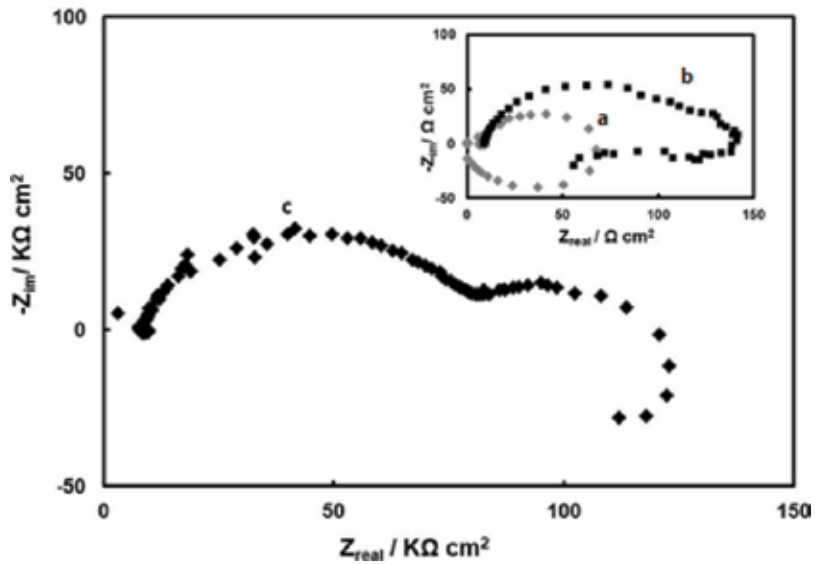


Figure 9. Nyquist plots of the impedance spectra obtained at OCP conditions after 5 min of immersion in Ringer solution at 37°C for: (a) AZ91D Mg alloy, (b) RCe-H₂O₂ film, and (c) RCe-HAsc film.

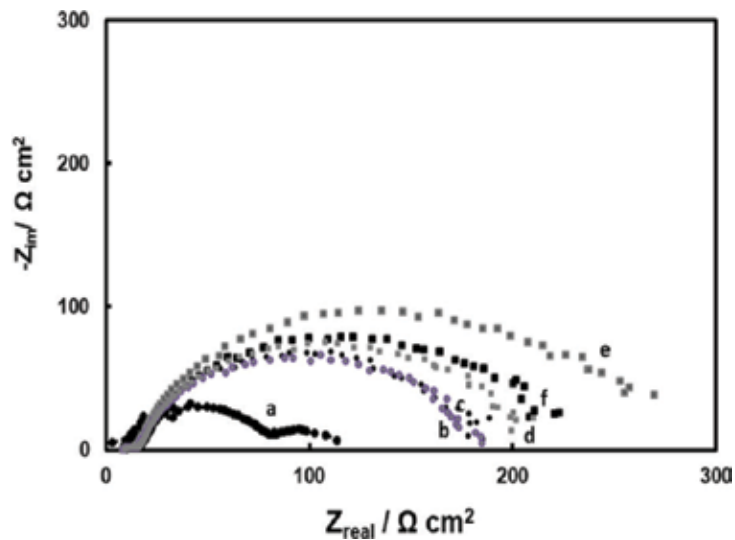


Figure 10. Nyquist plots of the impedance spectra obtained at OCP conditions in Ringer solutions at 37°C for RCe-HAsc coating, after different immersion times: (a) 5 min, (b) 6 h, (c) 12 h, (d) 24 h, (e) 36 h, and (f) 48 h.

When the uncoated AZ91D alloy is immersed in simulated physiological solution, it suffers significant degradation. As mentioned above, it is proposed that the general corrosion mechanism of Mg alloys implies Mg oxidation to Mg²⁺ with simultaneous water reduction. Cathodic reactions lead to a local alkalization which produces Mg(OH)₂ precipitation [36, 37]. The β-phase acts as the cathode and α-phase acts as the anode. The active surface area is reduced by RCe-HAsc film, and in consequence, less area of the substrate is available to be corroded. The potential difference

between α - and β -phases becomes smaller when the AZ91D alloy is coated by an adherent and stable film. Thus, the micro-galvanic couple effect is reduced [38, 39]. In summary, the coating confers a physical barrier between the substrate and the corrosive medium. In addition, the improvement in the corrosion resistance is associated with the presence of insoluble precipitates of cerium and the inhibitor effect of ascorbic acid. As mentioned previously, the HAsc has inhibition ability by insoluble chelates formation and it is responsible for the increased corrosion protection of RCe films. The presence of HAsc decreases the dissolution rate of the substrate during the coating formation allowing the formation of a more compact and protective film.

4. Morphological and compositional characterization of RCe-HAsc coating

Figure 11 presents the SEM image of the film obtained in solution containing 50 mM Ce(NO₃)₃ + 6 mM H₂O₂ (**Figure 11A**) or 50 mM Ce(NO₃)₃ + 6 mM H₂O₂ + 5 mM HAsc (**Figure 11B**). A cracked mud morphology is observed of RCe film. The dehydration of the surface film after the deposition leads to crack formation [40]. It has been suggested that the formation of gas bubbles on the substrate, combined with a dehydration process or also with shearing stresses between the alloys and the obtained film, is responsible of the cracked structure [41].

A more uniform and compact film with the presence of only some microcracks was obtained by the addition of HAsc in the conversion solution. From the SEM cross-sectional micrography, the thickness of the RCe-HAsc coating is approximately 5 μ m (**Figure 12**).

The presence of cerium in the coating was confirmed by EDX analysis (**Figure 13**). It is known that RCe coatings are obtained from the precipitation of oxides, due to an increase in local pH at the interface substrate/solution.

Figure 14 presents the XRD patterns of the AZ91D alloy and treated samples. By comparison it can be concluded that the coatings are composed of CeO₂, Ce₂O₃, and Mg(OH)₂.

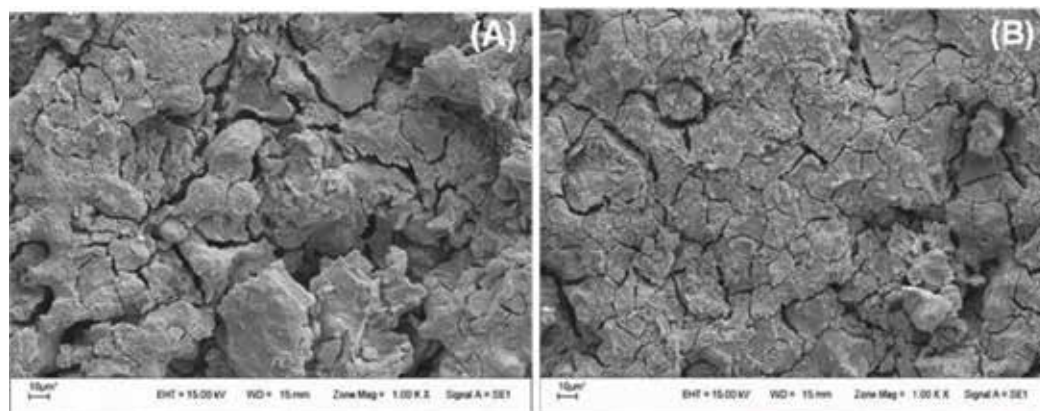


Figure 11. SEM image of the films obtained on AZ91D alloy. The film was formed at - 0.75 V during 30 min in 50 mM Ce(NO₃)₃ and 6 mM H₂O₂: (A) without HAsc and (B) with 5 mM HAsc.

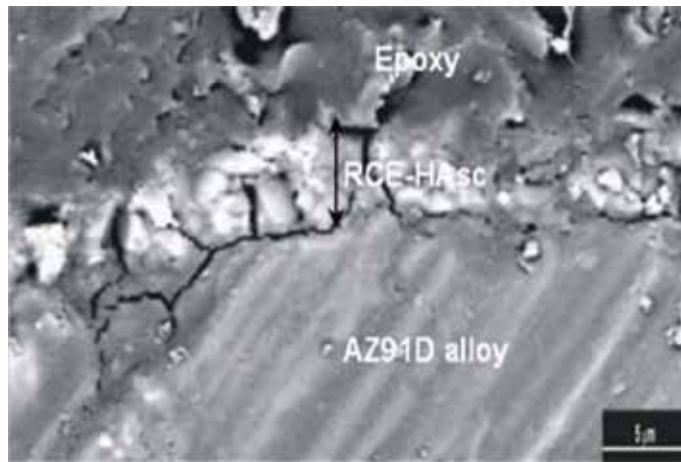


Figure 12. SEM micrograph showing the cross-section of RCE-HAsc coating. The coating was electrosynthesized at -0.75 V during 30 min in a solution containing 50 mM $\text{Ce}(\text{NO}_3)_3$, 6 mM H_2O_2 , and 5 mM HAsc.

In order to determine the surface chemical composition of RCE-HAsc coating, the XPS was employed. The XPS results are shown in **Figure 15**.

The main components are magnesium, oxygen, and cerium. **Figure 16** shows the XPS analysis of the specific electron binding energies of Mg, O, and Ce elements. From the Mg 2p spectrum, presented in **Figure 15**, it can be determined that Mg in the coating is present as MgO and $\text{Mg}(\text{OH})_2$ [2].

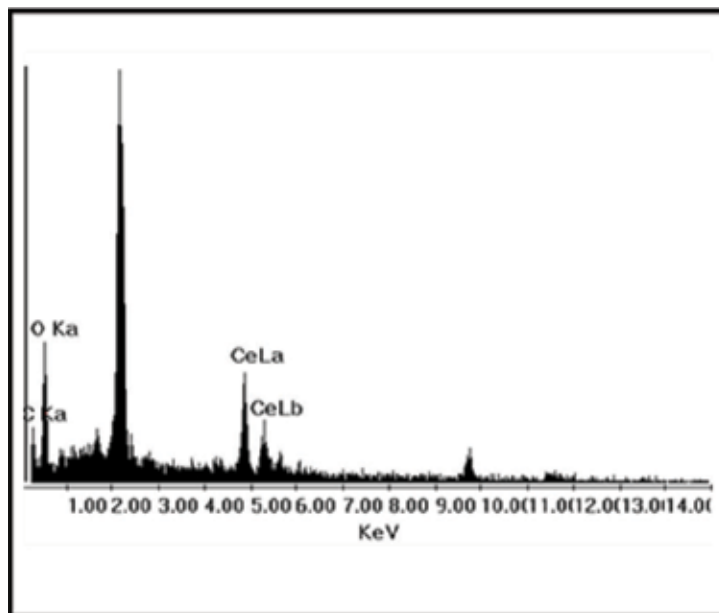


Figure 13. EDS spectrum of RCE-HAsc coating formed on AZ91D alloy. The coating was electrosynthesized at -0.75 V during 30 min in a solution containing 50 mM $\text{Ce}(\text{NO}_3)_3$, 6 mM H_2O_2 , and 5 mM HAsc.

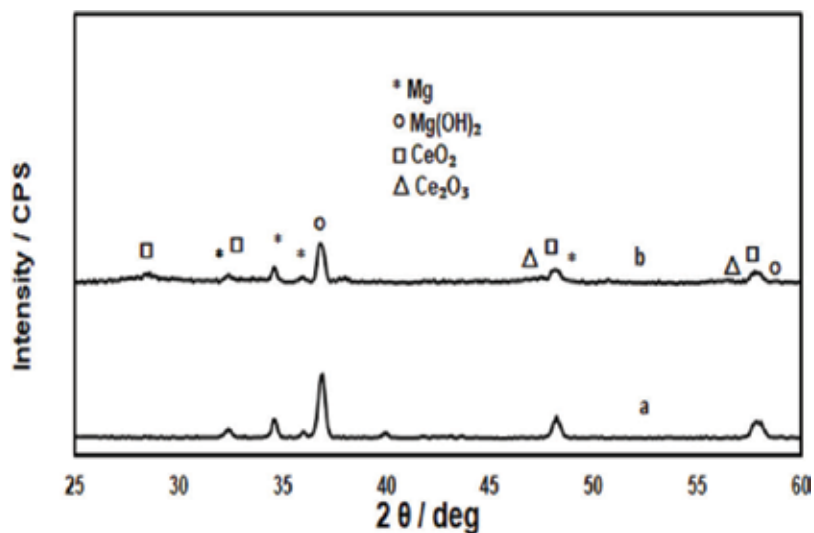


Figure 14. XRD spectra for: (a) AZ91D alloy and (b) RCe-HAsc coating.

Figure 16B shows the spectrum of O 1s. The peak at 531.25 eV is attributed to metallic oxides [2]. The Ce 3d_{5/2} and Ce 3d_{3/2} peaks are presented in **Figure 16C**. The analysis established that the binding energies at 916.0, 897.89, and 880.90 eV correspond to CeO₂, CeO, and Ce₂O₃, respectively. The satellite peak around 916.0 eV confirms the presence of Ce(IV) ions in the coating. The ratio between Ce(IV) and Ce(III) was 1.503. In summary, from the XPS results, it was concluded that the RCe-HAsc film is mainly composed of CeO₂, CeO, Ce₂O₃, MgO, and Mg(OH)₂.

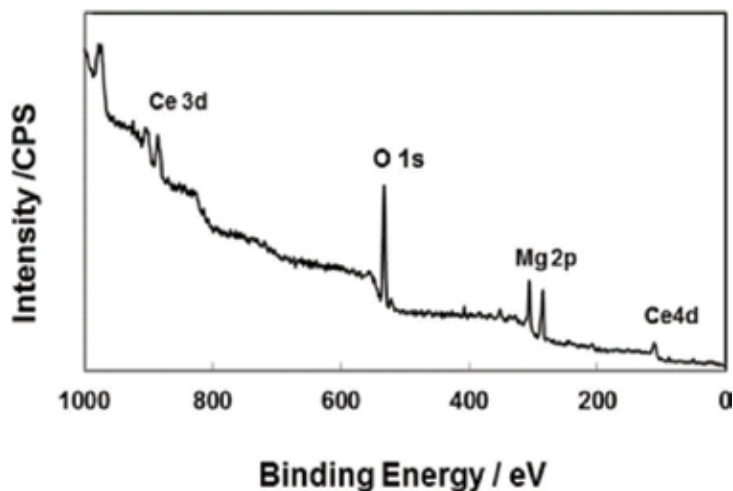


Figure 15. XPS survey spectrum of RCe-HAsc coating formed on AZ91D alloy. The coating was electro synthesized at -0.75 V during 30 min in 50 mM Ce(NO₃)₃, 6 mM H₂O₂, and 5 mM HAsc.

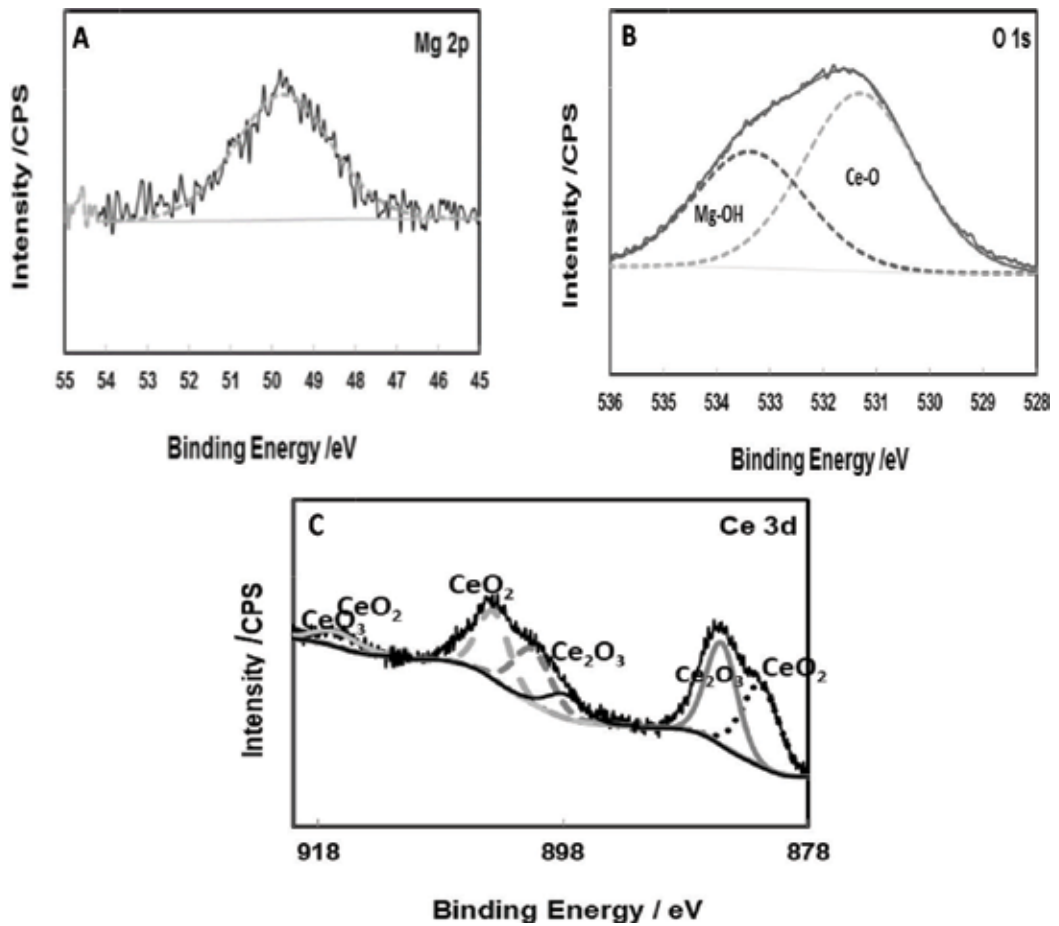


Figure 16. XPS intensities of: (A) Mg 2p, (B) O 1s, and (C) Ce 3d. The coating was electrosynthesized at -0.75 V during 30 min in 50 mM $\text{Ce}(\text{NO}_3)_3$, 6 mM H_2O_2 and 5 mM HAsc.

5. Conclusions

Adherent and uniform cerium-based coatings were obtained on AZ91D magnesium alloy in solutions containing cerium nitrate, H_2O_2 , and three different additives (H_3Cit , HAsc, and Na-citrate). The most adherent films were obtained by a potentiostatic polarization at -0.75 V. The RCe-HAsc-coated AZ91D alloy exhibited better corrosion resistance in Ringer solution. Magnesium oxides or hydroxides and cerium oxides are the main components of the film. The anticorrosive properties of RCe-HAsc film in simulated body fluid solution is superior to those of films formed in the absence of HAsc. The improvement in the corrosion resistance is associated with the presence of insoluble precipitates of cerium and the effect of the additive through the formation of insoluble chelates.

Acknowledgements

CONICET, ANPCYT, and Universidad Nacional del Sur, Bahía Blanca, Argentina, are acknowledged for financial support.

Nomenclature

EDX	energy dispersive X-ray spectroscopy
EIS	electrochemical impedance spectroscopy
HAsc	ascorbic acid
H ₃ Cit	citric acid
Na-citrate	sodium citrate
RCe	cerium-based coating obtained at -0.75 V in 50 mM Ce(NO ₃) ₃ solution
RCe-H ₂ O ₂	cerium-based coating obtained at -0.75 V in 50 mM Ce(NO ₃) ₃ and 6 mM H ₂ O ₂ containing solution
RCe-HAsc	cerium-based coating obtained at -0.75 V in 50 mM Ce(NO ₃) ₃ , 6 mM H ₂ O ₂ , and 5 mM HAsc containing solution
SEM	scanning electron microscopy
XPS	X-ray photoelectron spectroscopy
XRD	X-ray powder diffraction

Author details

Ana Paula Loperena, Ivana Leticia Lehr* and Silvana Beatriz Saidman

*Address all correspondence to: ilehr@uns.edu.ar

Chemical Engineering Department, Institute of Electrochemical and Corrosion Engineering, National University of the South, Bahía Blanca, Argentina

References

- [1] Rudd AL, Breslin CB, Mansfeld F. The corrosion protection afforded by rare earth conversion coatings applied to magnesium. *Corrosion Science*. 2000;**42**:275-288. DOI: 10.1016/S0010-938X(99)00076-1
- [2] Zheng YF, Gu XN, Witte F. Biodegradable metals. *Materials Science and Engineering R*. 2014;**77**:1-34. DOI: 10.1016/j.mser.2014.01.001

- [3] Ballerini G, Bardi U, Bignucolo R, Ceraolo G. About some corrosion mechanisms of AZ91D magnesium alloy. *Corrosion Science*. 2005;**47**:2173-2184. DOI: 10.1016/j.corsci.2004.09.018
- [4] Hornberger H, Virtanen S, Boccaccini AR. Biomedical coatings on magnesium alloys—A review. *Acta Biomaterialia*. 2012;**8**:2442-2455. DOI: 10.1016/j.actbio.2012.04.012
- [5] Montemor MF, Simoes AM, Ferreira MGS, Carmezim MJ. Composition and corrosion resistance of cerium conversion films on the AZ31 magnesium alloy and its relation to the salt anion. *Applied Surface Science*. 2008;**254**:1806-1814. DOI: 10.1016/j.apsusc.2007.07.187
- [6] Dabalà M, Brunellia K, Napolitanib E, Magrinia M. Cerium-based chemical conversion coating on AZ63 magnesium alloy. *Surface and Coatings Technology*. 2003;**172**:227-232. DOI: 10.1016/S0257-8972(03)00336-0
- [7] Yasakau KA, Zheludkevich ML, Lamaka SV, Ferreira MGS. Mechanism of corrosion inhibition of AA2024 by rare-earth compounds. *Journal of Physical Chemistry B*. 2006;**110**:5515-5528. DOI: 10.1021/jp0560664
- [8] Castano C, O'Keefe M, Fahrenholtz W. Cerium-based oxide coatings. *Current Opinion in Solid State and Materials Science*. 2015;**19**:69-76
- [9] Yu P, Hayes SA, O'Keefe TJ, O'Keefe MJ, Stoffer JO. The phase stability of cerium species in aqueous systems II. The Ce III/IV-H₂O-H₂O₂/O₂ systems. Equilibrium considerations and Pourbaix. Diagram calculations. *Journal of the Electrochemical Society*. 2006;**153**:C74-C79. DOI: 0013-4651/2005/1531/C74/6
- [10] Yang Y, Yang Y, Du X, Chen Y, Zhang Z, Zhang J. Influences of the main anodic electroplating parameters on cerium oxide films. *Applied Surface Science*. 2014;**305**:330-336. DOI: 10.1016/j.apsusc.2014.03.078
- [11] Cui X, Yang Y, Liu E, Jin G, Zhong J, Li Q. Corrosion behaviors in physiological solution of cerium conversion coatings on AZ31 magnesium alloy. *Applied Surface Science*. 2011;**257**:9703-9709. DOI: 10.1016/j.apsusc.2011.04.141
- [12] Scholes MF, Soste C, Hughes AE, Hardin SG, Curtis PR. The role of hydrogen peroxide in the deposition of cerium-based conversion coatings. *Applied Surface Science*. 2006;**253**:1770-1780. DOI: 10.1016/j.apsusc.2006.03.010
- [13] Valdez B, Kiyota S, Stoytcheva M, Zlatev R, Bastidas JM. Cerium-based conversion coatings to improve the corrosion resistance of aluminium alloy 6061-T6. *Corrosion Science*. 2014;**87**:141-149. DOI: 10.1016/j.corsci.2014.06.023
- [14] Eslamia M, Fedela M, Speranzab G, Defloriana F, Anderssonc N, Zanellac C. Study of selective deposition mechanism of cerium-based conversion coating on Rheo-HPDC aluminium-silicon alloys. *Electrochimica Acta*. 2017;**255**:449-462. DOI: 10.1016/j.electacta.2017.09.182
- [15] Chen S, Zhang S, Ren X, Xu S, Yin L. Cerium-based chemical conversion coating on aluminum alloy to inhibits corrosion in chloride solution. *International Journal of Electrochemical Science*. 2015;**10**:9073-9088

- [16] Loperena P, Lehr I, Saidman S. Formation of a cerium conversion coating on magnesium alloy using ascorbic acid as additive. Characterisation and anticorrosive properties of the formed films. *Journal of Magnesium and Alloys*. 2017;**4**:278-285. DOI: 10.1016/j.jma.2016.10.002
- [17] Wang C, Zhu S, Jiang F, Wang F. Cerium conversion coatings for AZ91D magnesium alloy in ethanol solution and its corrosion resistance. *Corrosion Science*. 2009;**51**: 2916-2923. DOI: 10.1016/j.corsci.2009.08.003
- [18] Zhou W, Shan D, Han E, Wei K. Structure and formation mechanism of phosphate conversion coating on die-cast AZ91D magnesium alloy. *Corrosion Science*. 2008;**50**: 329-337. DOI: 10.1016/j.corsci.2007.08.007
- [19] Kuznetsov YI, Thomas JGN, Mercer AD. *Organic Inhibitors of Corrosion of Metals*. New York: Springer Science & Business Media; 1996. 284 p. DOI: 10.1007/978-1-4899-1956-4
- [20] Katoh M. Influence of chelating agent (citric acid) and F⁻ on corrosion of Al. *Corrosion Science*. 1968;**8**:423-431. DOI: 10.1016/S0010-938X(68)90084-X
- [21] Ferrerira ES, Giacomellu C, Spinelli A. Evaluation of the inhibitor effect of L-ascorbic acid on the corrosion of mild steel. *Materials Chemistry and Physics*. 2004;**83**:129-134. DOI: 10.1016/j.matchemphys.2003.09.020
- [22] Akrouit H, Bousselmi L, Triki E, Maximovitch S, Dalard F. Effect of non-toxic corrosion inhibitors on steel in chloride solution. *Journal of Materials Science*. 2004;**39**:7341-7350. DOI: 10.1023/B:JMSC.0000048749.31437.b9
- [23] Valek L, Martinez S, Mikulic D, Brnardic I. The inhibition activity of ascorbic acid towards corrosion of steel in alkaline media containing chloride ions. *Corrosion Science*. 2008;**50**:2705-2709. DOI: 10.1016/j.corsci.2008.06.018
- [24] Fuchs-Godex R, Pavlovic M, Tomic M. The inhibitive effect of vitamin-C on the corrosive performance of steel in HCl solutions. *International Journal of Electrochemical Science*. 2013;**8**:1511-1519
- [25] Orinákova R, Turonová A, Kladeková D, Gálová M, Smith RM. Recent developments in the electrodeposition of nickel and some nickel-based alloys. *Journal of Applied Electrochemistry*. 2006;**36**:57-972. DOI: 10.1007/S10800-006-9162-7
- [26] Muralidharan S, Saraswathy V, Thangavel K, Srinivasan S. Competitive role of inhibitive and aggressive ions in the corrosion of steel in concrete. *Journal of Applied Electrochemistry*. 2000;**30**:1255-1259. DOI: 10.1023/A:1026570120698
- [27] Muralidharan S, Saraswathy V, Nima SPM, Palaniswamy N. Evaluation of a composite corrosion inhibiting admixtures and its performance in Portland Pozzolana cement. *Materials Chemistry and Physics*. 2004;**86**:298-306. DOI: 10.1016/j.matchemphys.2004.03.025
- [28] Ormellese M, Lazzari L, Goidanich S, Fumagalli G, Brenna A. A study of organic substances as inhibitors for chloride-induced corrosion in concrete. *Corrosion Science*. 2009;**51**:2959-2968. DOI: 10.1016/j.corsci.2009.08.018
- [29] Martinez S, Valek L, Oslakovic IS. Adsorption of organic anions on low-carbon steel in saturated Ca(OH)₂ and the HSAB principle. *Journal of the Electrochemical Society*. 2007;**154**(11):C671-C677. DOI: 10.1149/1.2777882

- [30] Vino A, Shweky I, Cohen S, Bauminger ER, Lippard SJ. A novel nonairon(III) citrate complex: A ferric triple-decker. *Inorganic Chemistry*. 1998;**37**(20):5168-5172. DOI: 10.1021/ic9715658
- [31] Bahramian A, Eyraud M, Vacandio F, Knauth P. Improving the corrosion properties of amorphous Ni-P thin films using different additives. *Surface and Coatings Technology*. 2018;**345**:40-52. DOI: 10.1016/j.surfcoat.2018.03.075
- [32] Dai Y, Li Q, Gao H, Li LQ, Chen FN, Luo F, et al. Effects of five additives on electrochemical corrosion behaviours of AZ31D magnesium alloy in sodium chloride solution. *Surface Engineering*. 2011;**27**(7):536-543. DOI: 10.1179/1743294410Y.0000000025
- [33] Liu D, Song Y, Sha D, Han E-H. Comparison of the inhibition effect of four inhibitors on the corrosion behavior of AM60 magnesium alloy. *International Journal of Electrochemical Science*. 2018;**13**:2219-2235. DOI: 10.20964/2018.03.23
- [34] Srinivasan A, Blawert C, Huang Y, Mendis CL, Kainer KU, Hort N. Corrosion behavior of Mg-Gd-Zn based alloys in aqueous NaCl solution. *Journal of Magnesium and Alloys*. 2014;**2**:245-256. DOI: 10.1016/j.jma.2014.08.002
- [35] Anik M, Celikten G. Analysis of the electrochemical reaction behavior of alloy AZ91 by EIS technique in H₃PO₄/KOH buffered K₂SO₄ solutions. *Corrosion Science*. 2007;**49**:1878-1894. DOI: 10.1016/j.corsci.2006.10.016
- [36] Zhang Y, Yan C, Wang F, Li W. Electrochemical behavior of anodized Mg alloy AZ91D in chloride containing aqueous solution. *Corrosion Science*. 2005;**47**:2816-2831. DOI: 10.1016/j.corsci.2005.01.010
- [37] Pardo A, Merino MC, Coy AE, Arrabal R, Viejo F, Matykina E. Corrosion behavior of magnesium/aluminum alloys in 3.5 wt.% NaCl. *Corrosion Science*. 2008;**50**:823-834. DOI: 10.1016/j.corsci.2007.11.005
- [38] Pezzato L, Brunelli K, Napolitani E, Magrini M, Dabalà M. Surface properties of AZ91 magnesium alloy after PEO treatment using molybdate salts and low current densities. *Applied Surface Science*. 2015;**357**:1031-1039. DOI: 10.1016/j.apsusc.2015.09.107
- [39] Song YW, Shan DY, Han EH. High corrosion resistance of electroless composite plating coatings on AZ91D magnesium alloys. *Electrochimica Acta*. 2008;**53**:2135-2143. DOI: 10.1016/j.electacta.2007.09.026
- [40] Brunelli K, Dabalà M, Calliani J, Magrini M. Effect of HCl pre-treatment on corrosion resistance of cerium-based conversion coatings on magnesium and magnesium alloys. *Corrosion Science*. 2005;**47**:989-1000. DOI: 10.1016/j.corsci.2004.06.016
- [41] Hamlaoui Y, Pedraza F, Remazeilles C, Cohendoz S, Rébéré C, Tifouti L, et al. Cathodic electrodeposition of cerium-based oxides on carbon steel from concentrated cerium nitrate solutions: Part I. Electrochemical and analytical characterization. *Materials Chemistry and Physics*. 2009;**113**:650-657. DOI: 10.1016/j.matchemphys.2008.08.027

Doped Ceria for Solid Oxide Fuel Cells

Shobit Omar

Additional information is available at the end of the chapter

<http://dx.doi.org/10.5772/intechopen.79170>

Abstract

Lower valent cation-doped CeO_2 materials have attracted remarkable research interest for the electrolyte application in solid oxide fuel cells operating in the intermediate temperature range (500–700°C). At these temperatures, the oxygen-ion conductivity of gadolinium-doped ceria is about an order of magnitude higher than that of yttria-stabilized zirconia. The oxygen-ion diffusion in the cubic fluorite structure of CeO_2 is dependent on several factors such as charge valence and size of dopant cation, doping amount, etc. In the literature, several conductivity trends have been reported as a function of these parameters and are explained by the atomistic computational models. This chapter describes the highlights of the various activities that have been done in this regard to provide insights into the mechanisms underlying the oxygen-ion conduction process in acceptor-doped ceria.

Keywords: bulk ionic conductivity, doped ceria, local defect complexes, defect chemistry, solid oxide fuel cells, electrolyte

1. Introduction

Cerium oxide is the most thoroughly investigated material for the application in solid oxide fuel cells (SOFCs) working in the intermediate-temperature range (500–700°C) [1, 2]. This is because of its pronounced catalytic properties, substantial oxygen-ion conductivity (on doping with lower valent metal oxides) and good phase and thermal stability in the given temperature range. The high catalytic activity in ceria is associated with the presence of $\text{Ce}^{4+}/\text{Ce}^{3+}$ redox couple which is a key to improve the electrochemical properties of the electrodes. Although this is one area where most of the papers related to ceria have been produced, in this chapter, we restrict our discussion to its usefulness as an electrolyte in SOFCs [3].

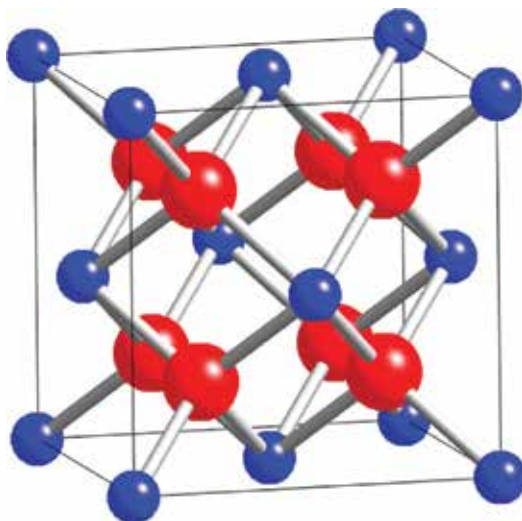


Figure 1. Schematic of a cubic fluorite structure of CeO_2 . Ce^{4+} and O^{2-} are shown by blue and red spheres, respectively.

Ceria exhibits a cubic fluorite crystal structure that possesses a relatively large interionic open space facilitating fast oxygen-ion diffusion inside the lattice (shown in **Figure 1**). This open structure is stable from room temperature to its melting point ($\sim 2400^\circ\text{C}$) and allows to accommodate high levels of point defect disorder [4]. Several properties such as ionic conduction, thermoelectric effect, mixed ionic-electronic conductivity, etc., can be altered and tailored by controlling the concentration of these zero-dimensional defects [5]. As a result, the defect engineering in ceria plays a vital role in improving its properties for the electrolyte application.

Oxygen-ion conduction in ceria is mediated through a vacancy diffusion mechanism. In oxidizing atmospheres, the cubic fluorite structure of pure CeO_2 does not have any oxygen vacancy defects. As a result, pure CeO_2 itself is a poor oxygen-ion conductor. The oxygen vacancy defects are introduced into the CeO_2 structure by partially substituting Ce^{4+} with acceptor cations inside the lattice. This can be expressed through the following defect reaction in Kröger-Vink notation.



Thus, the impurity center (A'_{Ce}) and oxygen vacancy ($V_{\text{O}}^{\bullet\bullet}$) are the dominant extrinsic ionic defects in trivalent metal oxide doped ceria. Nearly, all oxygen anions vibrate in the region of their tetrahedral sites and under a sufficient driving force, jump from their respective site to the adjacent vacant oxygen-ion site in (100) direction. Though the other conduction pathways are also present, they have a substantially large jump barrier [6]. As a result, the jump distance of oxygen-ion is half the length of the unit cell. During migration from one tetrahedral site to another, oxygen-ion is required to pass through an edge formed by cations shared by the involved tetrahedrons (shown in **Figure 2**).

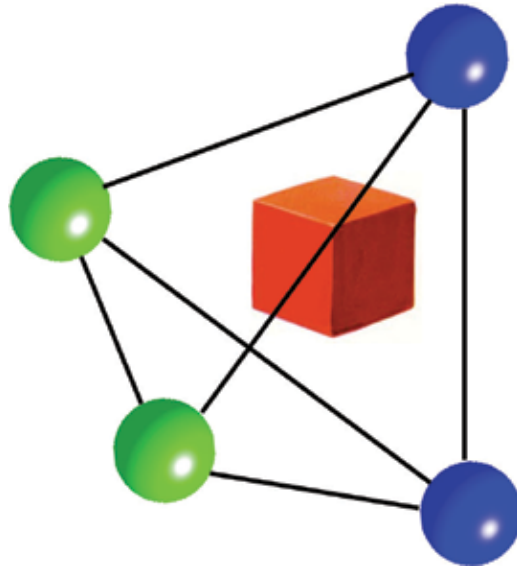
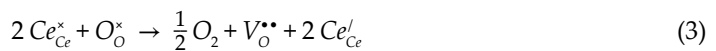


Figure 2. Schematic showing the jump of an oxygen vacancy from one tetrahedral to another through a migration edge. Ce^{4+} , A^{3+} and O^{2-} are shown by blue, green, and red spheres, respectively, while oxygen vacancy is shown by red cube.

For a pure oxygen-ion conductor, oxygen-ion conductivity (σ) can be expressed by,

$$\sigma = (1 - [V_o^{\bullet\bullet}]) N_o q_i \mu_i \quad (2)$$

where N_o is the concentration of oxygen sites, $[V_o^{\bullet\bullet}]$ is the fraction of oxygen-ion vacancy and μ_i is the mobility of oxygen-ions with charge denoted as q_i . Several studies have demonstrated that at high temperatures ($>700^\circ C$) and under the reducing environments (present on the anode side of SOFC device), Ce^{4+} present in ceria tends to reduce to Ce^{3+} leading to the formation of oxygen vacancy and two additional electrons as a charge compensating defect.



These electrons are typically localized in the periphery of Ce^{3+} , leading to the formation of small polarons (Ce_{Ce}'). These polarons not only break the translation symmetry of crystal but also induce a local lattice distortion around the Ce_{Ce}' site. The migration of polaron results in electronic conduction which contributes a portion of the measured total conductivity in bulk ceria. However, for the solid oxide electrolyte, the electronic conductivity should be kept as low as possible not only to minimize the leakage current which if present decreases the overall cell efficiency, but also to avoid the warping and delamination of electrolyte layer because of the chemical expansion [4]. As a result, the use of doped ceria is restricted to conditions (less than $\sim 700^\circ C$, $P_{O_2} > 10^{-18}$ atm) where the electronic conduction is substantially lower than the ionic conduction and thus can be neglected [7].

Oxygen-ion diffusion in doped ceria is a thermally activated process. The temperature dependent behavior of the oxygen-ion conductivity can be expressed through Arrhenius relationship given by,

$$\sigma T = \sigma_o \exp\left(-\frac{E_A}{kT}\right) \quad (4)$$

where σ_o is a pre-exponential factor and E_A is the activation energy of oxygen-ion conduction. The value of E_A is determined from the gradient of the linear-fit of the σ data plotted between $\log\sigma T$ versus $1/T$. The detailed form of Eq. (4) is given by,

$$\sigma T = \frac{q_V^2}{k} [V_{O^{\bullet\bullet}}] (1 - [V_{O^{\bullet\bullet}}]) N_o a^2 v_o \exp\left(\frac{\Delta S_m}{k}\right) \exp\left(-\frac{\Delta H_m}{kT}\right) \quad (5)$$

where a is the jump distance of oxygen-ion, v_o is an appropriate lattice vibration frequency, and ΔS_m and ΔH_m are the change in entropy and enthalpy, respectively, during oxygen-ion diffusion. On comparing Eqs. (4) and (5), it is apparent that the change in enthalpy during oxygen-ion diffusion (ΔH_m) is, in fact, the activation energy (E_A) shown in Eq. (4). Thus, an explicit relationship between the conductivity and temperature is provided in Eq. (5).

It is noteworthy to mention that even though the total conductivity of polycrystalline samples is influenced by the conductivity inside the grains and grain boundaries, in this chapter, we only refer to the grain (bulk) conductivity which occurs by oxygen-ion jump through the regular lattice and is not affected by the microstructural characteristics of the sample. Thus, the bulk ionic conduction is the inherent property of the doped material [8]. On the other hand, the conduction in grain boundaries is dependent on several factors such as impurity segregation, space-charge region, etc. [9]. Both the bulk and grain boundary conductivity can be estimated by acquiring an impedance spectrum over a frequency range (typically 10 MHz to 0.01 Hz) on the polycrystalline sample [10]. As grain boundaries show higher capacitance value (in the range from 10^{-8} to 10^{-11} F) compared to the bulk region ($\sim 10^{-12}$ F), two distinct arcs are typically observed associated with these phenomena [10]. On fitting the impedance data using an analog equivalent electric circuit, the resistance offered by bulk and grain boundary regions is estimated which can be then be used in determining the corresponding conductivities.

The bulk conductivity has a significant dependence on the concentration of oxygen vacancy which is controlled by the doping amount according to $2[A'_{Ce}] = [V_{O^{\bullet\bullet}}]$ in A_2O_3 -doped CeO_2 . It can be observed from Eq. (5) that the conductivity would likely to follow a parabolic behavior as a function of oxygen vacancy concentration and reaches its maximum value when half of the oxygen sublattice is unoccupied. From several investigations on fluorite-structured oxides (including ceria), it has been found that even though conductivity exhibits maxima when plotted against the dopant concentration, the maximum in conductivity appears at significantly lower dopant fractions (less than 0.4) [11–13]. **Figure 3** shows the bulk conductivity of $Sm_{x/2}Nd_{x/2}Ce_{1-x}O_{2-x/2}$ as a function of doping amount (x) at various temperatures [8]. At 550°C, the maximum in conductivity is found at $x = 0.15$. On lowering the temperature, the doping fraction leading to the maximum in conductivity (x_{max}) shifts toward the lower value. Thus, the conductivity data obtained at low temperatures results in low x_{max} while the high-temperature data will possess a high value of x_{max} [6]. Further, the x_{max} value is also dependent on the charge valence and size of acceptor dopant used to generate oxygen vacancies in ceria. This is attributed to the formation of local defect complexes which are discussed in the later section.

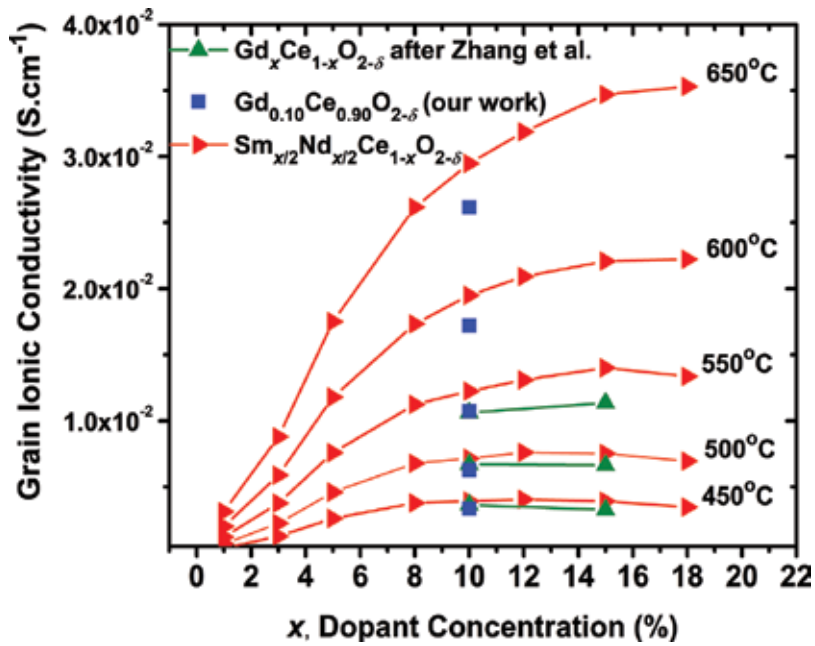


Figure 3. Bulk ionic conductivity is plotted against the dopant concentration (x) in $\text{Sm}_{x/2}\text{Nd}_{x/2}\text{Ce}_{1-x}\text{O}_{2-\delta}$ and $\text{Gd}_x\text{Ce}_{1-x}\text{O}_{2-\delta}$ [8, 14].

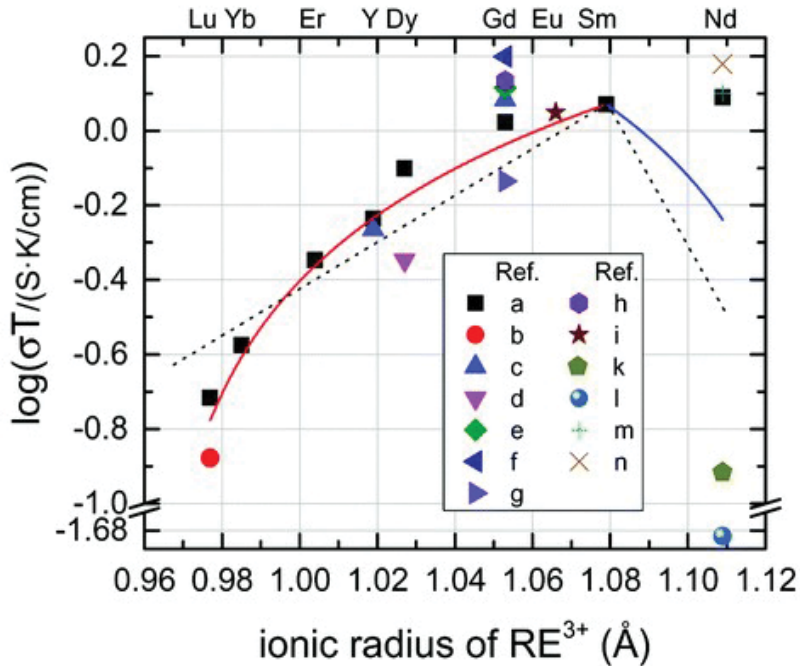


Figure 4. Bulk ionic conductivity of $\text{A}_x\text{Ce}_{1-x}\text{O}_{2-x/2}$ (with $x = 0.1$) at 400°C plotted against the radius of dopant cation. The conductivity data are taken according to references a [15], b [23], c [14], d [24], e [25], f [26], g [27], h [28], i [29], k [30], l [31], m [32] and n [33]. The lines show a linear relationship between the ionic radius and the conductivity (solid lines) or the logarithm of the conductivity (dashed lines) [6].

Besides the doping amount, the physical properties of dopant cations also influence the bulk conductivity of ceria. Numerous investigations have been performed to understand these correlations in doped ceria systems [1, 15–19]. **Figure 4** depicts the dependence of ionic conductivity in $A_{0.10}Ce_{0.90}O_{1.95}$ on the ionic size of the trivalent dopant cation (A^{3+}) at 600°C. While the work performed by Omar et al. [15] showed a continuous increase in the bulk conductivity with the increase in ionic size, others [17, 20–22] reported a conductivity maximum around Gd^{3+} and Sm^{3+} . It is interesting to note that the maximum in conductivity observed around these cations is independent of dopant concentration [6]. In the literature, several empirical, semi-empirical and atomistic models have been reported to clarify this and elucidate the effect of doping amount and the dopant-type on the conductivity. This chapter reviews some of these models to provide insights into the mechanisms underlying the oxygen-ion conduction process in doped ceria.

2. Formation of local defect complexes

Whenever charged point defects (A'_c) are incorporated into the crystal structure, to maintain electroneutrality, defects possessing opposite charges must be created. These oppositely charged defects strongly interact with each other because of electrostatic attraction. Further, the elastic interactions also exist to relax the local stresses surrounding these defects. For example, an oversized substitutional impurity cation may attract an open space of vacancy. This leads to the formation of local defect complexes such as $(A'_c - V_o^{**} - A'_c)$ and $(A'_c - V_o^{**})^*$. These defect complexes trap the oxygen vacancies and effectively reduce the number of mobile oxygen-ions. In most literature, it is commonly accepted that the primary reason for the significant decrease in ionic conductivity of doped ceria at higher dopant content is essentially because of the formation of local defect complexes.

Figure 5 depicts a case where V_o^{**} defect is trapped in a tetrahedral site of the fluorite structure surrounded by oppositely charged dopant cations and neutral host cations. There are several experimental studies which support the formation of local defect structures. Extended X-ray absorption

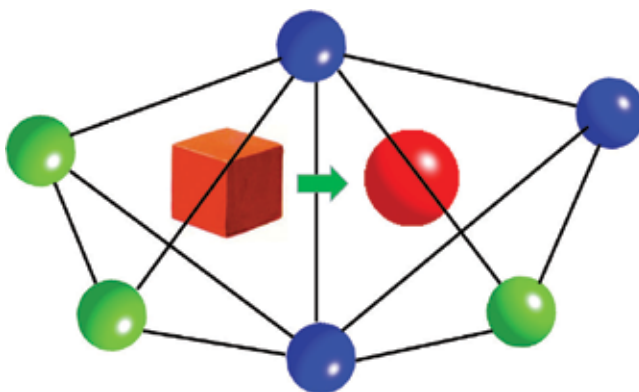


Figure 5. Oxygen vacancy defect trapped inside the tetrahedral void to form local defect complex. Ce^{4+} , A^{3+} and O^{2-} are shown by blue, green, and red spheres, respectively, while oxygen vacancy is shown by red cube.

fine structures (EXAFS) have been extensively utilized to study the local structures around the cations and anions in lower-valent cation-doped ceria [34–36]. In case of $\text{Gd}_x\text{Ce}_{1-x}\text{O}_{2-x/2}$, the addition of Gd^{3+} leads to a decrease in the interatomic distance Gd-O which is attributed to the formation of the defect complexes with two Gd^{3+} and one oxygen vacancy [37]. The formation of local defect structure is also evident in the nuclear magnetic resonance study where the average coordination number is estimated for cations in Y^{3+} - and Sc^{3+} -doped CeO_2 [38]. The tendency of oxygen vacancies to preferentially associate with Sc^{3+} was found to be stronger than with Y^{3+} in these systems.

The binding energy associated with the local defect structures is mainly dependent on the electrostatic attraction of the defects caused by the effective charges in the lattice. Further, it also includes terms due to the relaxation of the lattice around the defect which depends on the polarizability and the size of dopant cation. Several groups have found a difference in the magnitudes of E_A when measured in the high- and low-temperature regimes [14, 39]. Typically, the activation energy value estimated in a low-temperature regime is higher than that in the high-temperature region. In a few investigations, a kink is noticed around 350–600°C in the Arrhenius plot of the measured ionic conductivity [14]. Nevertheless, there are several other studies where instead of a sharp, a gradual change in slope with temperature is reported [8, 40]. It has been argued that in a low-temperature regime, most of the oxygen vacancies are bound to various traps to form local defect complexes [41]. However, at higher temperatures, the thermal vibrations of the local defect structures become dominant. At a certain temperature, the thermal energy overcomes the binding energy of these local defect complexes, and the majority of oxygen vacancy defects are set free to migrate from one site to another. Thus, the oxygen vacancies require only migration (ΔH_m) to cross the energy barrier at higher temperatures. As a result, in the low-temperature region, the total E_A is composed of ΔH_m and association enthalpy (ΔH_a), whereas in the high-temperature region, the measured E_A is only because of migration enthalpy of oxygen-ions.

In the literature, several methods have been used to determine the association enthalpy. Omar et al. [42] have taken a difference in the magnitudes of E_A obtained in the high- and low-temperature regimes and reported the association enthalpy in $\text{Sm}_{x/2}\text{Nd}_{x/2}\text{Ce}_{1-x}\text{O}_{2-x/2}$ in the range

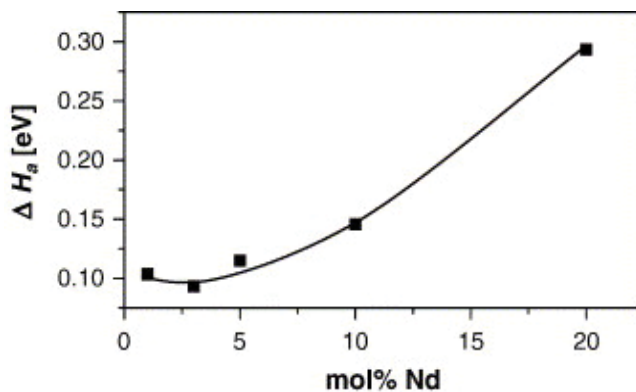


Figure 6. Association enthalpy (ΔH_a) is plotted against the Nd^{3+} doping amount in $\text{Ce}_{1-x}\text{Nd}_x\text{O}_{2-x/2}$. For the calculation of ΔH_a , the minimum value of the E_A measured in the low-temperature range (i.e., below 350°C) has been assumed to be equal to the enthalpy of migration [32].

of 0.02–0.05 eV [42]. Nowick et al. [43] obtained the association enthalpy by estimating the migration enthalpy in pure CeO₂ to be 0.67 eV. Stephen and Kilner [32] have taken the minimum value of E_A measured in the low-temperature regime in Nd_xCe_{1-x}O_{2-x/2} as a migration enthalpy. The association enthalpy initially decreases and then increases after reaching a minimum value at $x = 0.03$ (shown in **Figure 6**) [32]. The increase in association enthalpy is attributed to the development of deep vacancy association. A similar trend in association enthalpy is also observed for other dopant cations such as Y³⁺, Gd³⁺ and Sm³⁺ and so on [11, 14, 44].

3. Elastic lattice strain

The amount of local defect structures increases with the incorporation of oxygen vacancies inside the lattice. For achieving high oxygen-ion conductivity, the association of defects needs to be minimized. Kilner and Brook [45] stated that the oxygen-ion conductivity in doped CeO₂ could be enhanced if the elastic strain present in the lattice is lowered. Kim [46] partially replaced acceptor cations in fluorite-structured MO₂ (where M is a tetravalent cation) and studied the change in lattice parameter of the host oxides. By performing multiple regression analysis, an empirical model was developed that can predict the elastic strain in doped ceria systems for any given dopant cation. This model takes into consideration the size mismatch and difference in charge valence between the dopant and host cations and the dopant concentration. Further, Kim [46] proposed the concept of critical ionic radius (r_c) which was described as the ionic radius of a cation which on doping leads to a negligible distortion in the host fluorite lattice. For the trivalent dopant cation and host ceria, the value of r_c was estimated to be 1.038 Å. Based on Kilner and Brook's prediction, the cation with the ionic radius of r_c is the optimal dopant that can lead to the maximum oxygen-ion conductivity in CeO₂ [45]. As a result, the oxygen-ion conductivity in doped CeO₂ depend upon the ($|r_d - r_c|$) value, where r_d is the ionic radius of dopant. The lower the $|r_d - r_c|$ value for a particular dopant, the higher the ionic conductivity for that system is expected to be. Kim [46] argued that the highest ionic conductivity is observed around Gd³⁺ (see **Figure 4**) as r_c value is close to the ionic radius of Gd³⁺ ($r_{Gd, VIII}^{3+} = 1.053$ Å).

In a similar study, Hong and Virkar [47] calculated the r_c value to be 1.024 Å using a simple analytical model that can also predict the elastic lattice strain present in doped CeO₂. In this model, the oxygen vacancy is treated as one of the chemical species whose size remains constant irrespective of the size and concentration of dopant cation.

To examine the validity of minimum strain's hypothesis, Omar et al. [23] have carried out the experimental studies using a novel co-doping strategy in ceria. A co-dopant pair of Lu³⁺ and Nd³⁺ were chosen and added in a ratio such that the weighted average dopant ionic radius of co-dopants matches the magnitude of r_c . Using this approach, it is expected that, on average, the positive elastic strain because of larger dopant cation (i.e., Nd³⁺) is compensated by the negative elastic strain caused by the smaller dopant cation (i.e., Lu³⁺). This, as a result, prevents any distortion in fluorite lattice that is usually present in singly doped ceria systems. On calculating the lattice parameter, almost negligible elastic lattice strain was seen in these systems (see **Figure 7**). However, the ionic conductivity in Lu³⁺ and Nd³⁺ co-doped

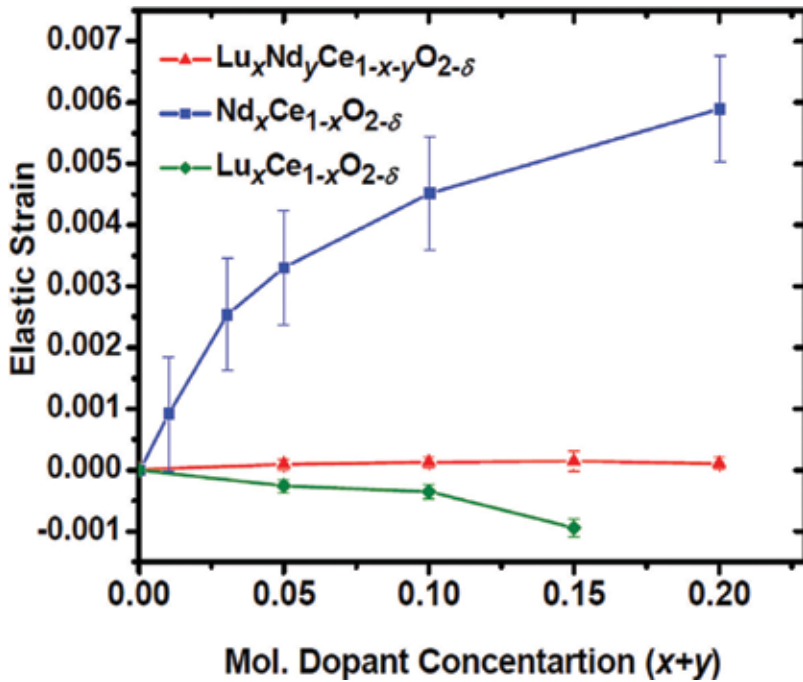


Figure 7. Elastic strain is plotted against the dopant concentration [23]. Data for $\text{Nd}_x\text{Ce}_{1-x}\text{O}_{2-\delta}$ were taken after Stephens et al. [32].

CeO_2 system was found to be lower than that of Gd^{3+} -doped CeO_2 [23]. Thus, even though the co-doped CeO_2 system exhibits minimal elastic strain, its oxygen-ion conductivity remains inferior to that of Gd^{3+} -doped CeO_2 .

On plotting the activation energy for oxygen-ion diffusion in trivalent cation-doped CeO_2 , it has been found that the minimum value for activation energy occurs for Sm^{3+} which possesses a much larger ionic radius than the r_c value [15]. Thus, both co-doping results and the obtained activation energy values do not support the hypothesis given by Kilner and Brook [45] that the highest oxygen-ion conductivity is obtained in the system having a negligible elastic lattice strain. However, it is noteworthy to mention that all the r_c values reported in the literature are derived from the empirical relationships which are based on the lattice expansion data acquired at room temperature. As the oxygen-ion conductivity of doped CeO_2 materials is usually measured between 400°C and 700°C , there is a possibility that the r_c value increases with the increasing temperature. Omar et al. [15] tested this hypothesis by measuring the lattice distortion for various doped CeO_2 systems (with 10 mol.% dopant concentration) at higher temperatures. The r_c value was then determined, where the lattice parameter mismatch between doped and pure CeO_2 becomes zero (see **Figure 8**). It was noticed that the r_c value decreases with the increase in temperature and does not follow the conductivity trend. The obtained results clearly indicate that the oxygen-ion conductivity is not solely dependent on elastic strain, and therefore, a structure-conductivity relationship based on the critical ionic radius concept is insufficient to describe the conduction behavior in doped ceria.

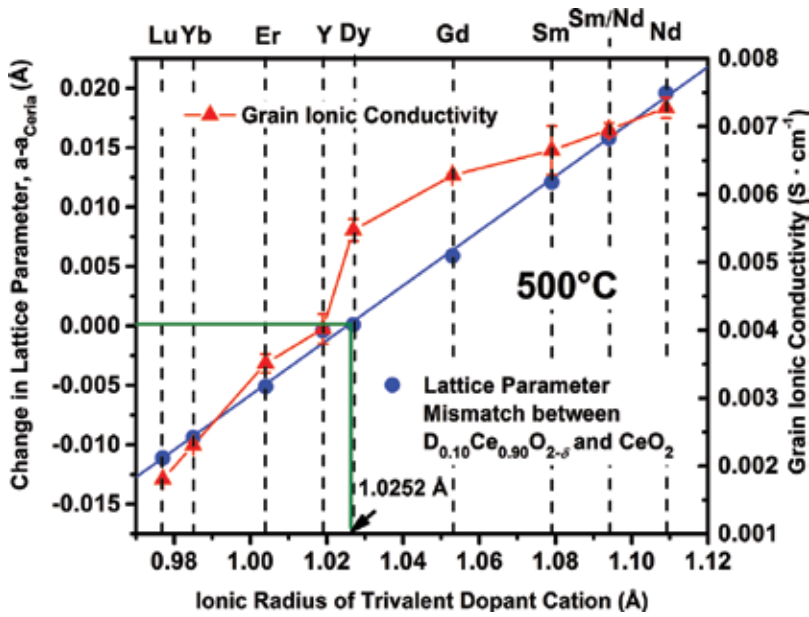


Figure 8. Lattice parameter mismatch between $A_{0.10}Ce_{0.90}O_{2-d}$ and CeO_2 is plotted against the ionic radius of dopant cation (A^{3+}) at $500^\circ C$. The grain (bulk) oxygen-ion conductivity of $A_{0.10}Ce_{0.90}O_{2-d}$ at $500^\circ C$ is also shown [15].

4. Dopant cation-oxygen vacancy interaction energetic

In the past, multiple atomistic computer simulation techniques have been used to study the interaction energetic involved between the cations and oxygen vacancies in acceptor cation-doped CeO_2 . Butler et al. [48] reported that the ionic radius of dopant has a major influence on the stability of defect complexes. Minervini et al. [49] studied the binding energy of an oxygen vacancy with dopant cation using the energy minimization techniques. It was found that the oxygen vacancies prefer to reside in the first neighboring sites of small dopant cations and in the second neighboring sites of large dopant cations. For Gd^{3+} dopant cation, the oxygen vacancy shows similar preference to reside in first and second neighboring sites. Moreover, the binding energy was also estimated to be lowest in Gd^{3+} -doped CeO_2 . Although these theoretical studies show a close match with the experimental results, they are based on empirical atomistic models.

Andersson et al. [16] performed the quantum mechanical calculations within the density functional theory (DFT) formalism in trivalent cation-doped CeO_2 . Both electrostatic and elastic interaction energies between the dopant cation and oxygen vacancy located in nearest neighbor (NN) site and in the next to nearest neighbor (NNN) site (of dopant cation) were predicted using the *ab-initio* calculations. It was found that for Pm^{3+} dopant cation, the total interaction energy values are similar for both the configurations (shown in **Figure 9**). As a result, the Pm^{3+} -doped CeO_2 system contains the maximum number of oxygen sites with equi-interaction energy inside the host lattice. There will be no site preference for oxygen vacancies

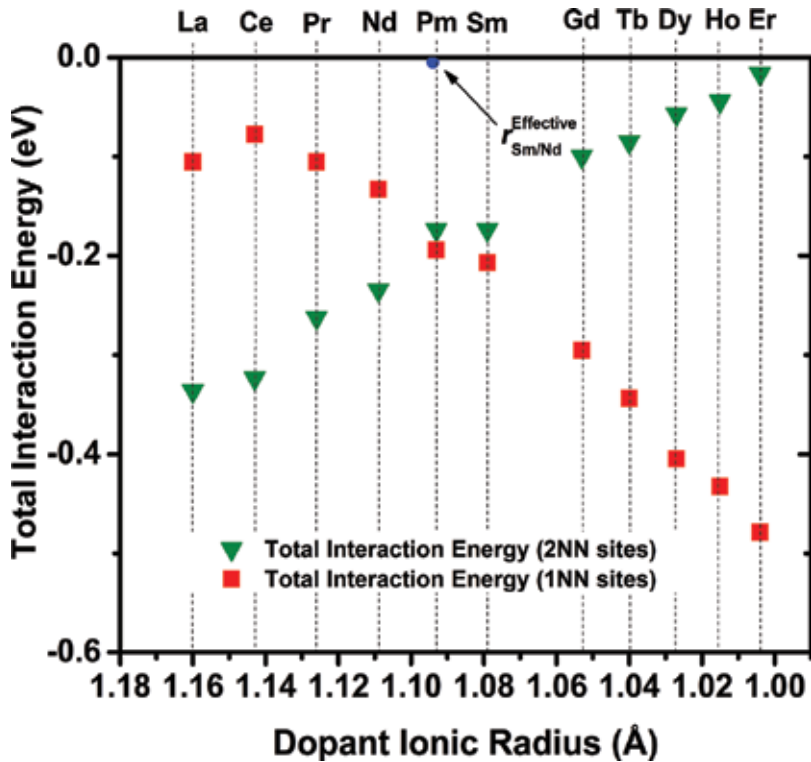


Figure 9. Total interaction energy between dopant cation and oxygen vacancy sitting in nearest neighbor (NN) and next to nearest neighbor (NNN) site (of dopant cations) for rare-earth dopant cations. The negative numbers imply attractive interactions. The $r_{Sm/Nd}^{Effective}$ is the weighted average ionic radius of Sm^{3+}/Nd^{3+} . The figure is modified after Andersson et al. [16].

which leads to minimal deep traps inside the doped ceria lattice. Thus, Pm^{3+} -doped CeO_2 was predicted to exhibit higher oxygen-ion conductivity than any other acceptor-doped ceria materials.

Unfortunately, Pm is a radioactive element and cannot be used as a dopant in ceria. The best dopant should be having an effective atomic number around Pm^{3+} (61) with an ionic radius of 1.093 Å. According to Andersson et al. [16], a co-doping approach, with Sm^{3+} and Nd^{3+} as co-dopants, provides an experimental scenario for examining the validity of this hypothesis. Omar et al. [8, 42] have studied the influence of co-doping Sm^{3+} and Nd^{3+} on the oxygen-ion conductivity of CeO_2 . Sm^{3+} and Nd^{3+} were added in an equal ratio to obtain the effective atomic number of Pm^{3+} , that is, 61. By doing so, similar total interactions between the dopant cations and oxygen vacancies sitting in NN and NNN sites (of dopant cations) are expected, which may lead to enhancement in the oxygen-ion conductivity. It was reported that for compositions containing 10 mol.% of dopant, Sm^{3+} and Nd^{3+} -doped ceria exhibits 14% higher grain ionic conductivity than that of $Gd_{0.10}Ce_{0.90}O_{2.95}$ at 550°C, in air (shown in Figure 3). The obtained high conductivity of co-doped samples validates the density functional theory prediction about Pm^{3+} to be the best dopant cation for achieving high oxygen-ion conductivity in CeO_2 .

5. Migration enthalpy in the local environment

Although several investigations have shown the formation of local defect structures in doped ceria systems, only a few models exist which describe the doping fraction at which they start appearing and directly influencing the conductivity. Also, in several experimental investigations, the observed trend in macroscopic migration enthalpy is attributed to the microscopic level association between dopant cation and oxygen vacancies without a thorough understanding of underlying atomistic level mechanisms. In earlier studies, the local defect structures are considered as one of the chemical species whose concentration is described using the equilibrium thermodynamics [1, 39]. However, this approach does not take into account the interactions between the local defect structures, especially at higher doping concentrations (>10 mol.% A_2O_3).

Multiple atomistic simulations studies have been performed to comprehend the relationships between the macroscopic conductivity and the migration in various local environments. In one of the earlier theoretical studies, Murray et al. [50] used Kinetic Monte Carlo (KMC) simulations to consider the migration enthalpy in the local environment to estimate the oxygen-ion conductivity as a function of doping level. It was reported that at higher doping concentration, oxygen vacancies tend to reside next to dopants, and thus do not contribute toward ionic conduction.

In a similar investigation, Nakayama et al. [51] used *ab-initio* density functional theory calculations to identify two key relationships that govern the oxygen-ion migration in rare-earth cation-doped ceria. First, the lowering of migration energy barrier by doping with a smaller trivalent cation would be accompanied by trapping of an oxygen vacancy at the nearest neighboring sites of the dopant. Second, doping with a larger trivalent cation increases the energy barrier but decreases the trapping effect of oxygen vacancies. Thus, the relative magnitude of these two effects is dependent on the size of dopant cation which in turn decides the magnitude of oxygen-ion conductivity.

In recent work by Koettgen et al. [6], the oxygen-ion conductivity was calculated as a function of the doping amount by combining *ab-initio* density functional theory and Kinetic Monte Carlo simulations. A model was developed that can estimate migration energies for all the possible jump configurations present in rare-earth-doped CeO_2 system. Migration energies were analyzed for energy contributions that are either energetically symmetric for both migration directions, that is, forward and backward jumps or energetically asymmetric for the forward and backward directions. If the presence of dopant changes the migration energy identically in both the backward and forward directions, the energy contribution, in this case, is referred to as blocking. On the other hand, if the migration energy is different for forward and backward jumps, the energy contribution is referred to as trapping.

Figure 10 shows the schematic of trapping and blocking effects. The energy of the system as a function of a reaction coordinate for the corresponding configuration is also shown. It was demonstrated that both these effects have an impact on the observed ionic conductivity. While blocking effect determines the doping fraction at which the maximum in conductivity is observed, it is the trapping effect which limits the maximum ionic conductivity value.

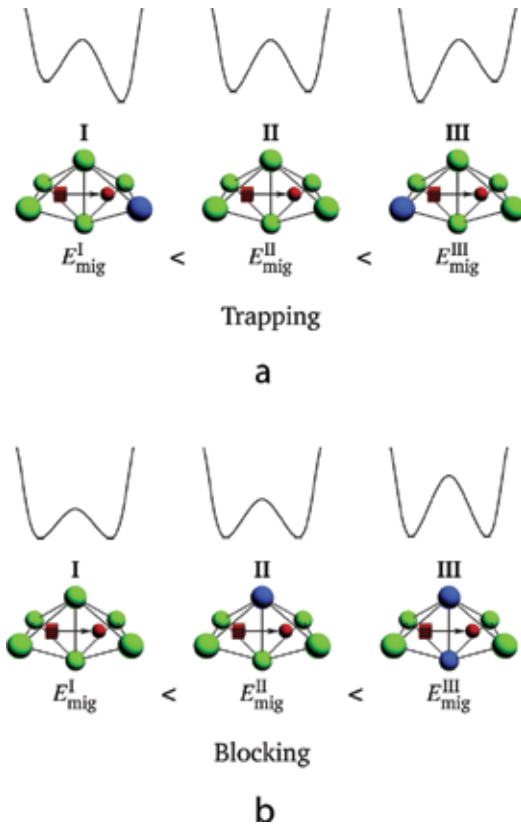


Figure 10. The energy of the system as a function of the reaction coordinate for the configuration change that is shown below in rare-earth-doped ceria. In trapping effect, migration enthalpy increases if the oxygen-ion jump weakens the association between the oxygen vacancies and the dopants. In case of blocking effect, the migration energy increases for an increasing number of large dopants at the migration edge: cerium ions (green), rare-earth ions (blue), oxygen ions (red spheres), and oxygen vacancies (red boxes) [6].

Thus, this study clarifies that the optimal doping concentration to achieve the maximum ionic conductivity cannot be predicted only by trapping effect (association between dopant cation and oxygen vacancies) which is commonly assumed in the literature.

6. Summary and conclusion

This chapter reviews some of the highlights of investigations performed on lower-valent cation-doped ceria materials which have been considered strong candidates for the electrolyte application in SOFCs operating at the intermediate-temperature range. Some of the basic characteristics of doped ceria relating to its high oxygen-ion conductivity are discussed. The maximum in conductivity observed by adding a large amount of lower-valent dopant cation is explained on the basis of formation of local defect structures. The extent of formation of these local defect structures cannot be lowered by just minimizing the elastic lattice distortion. It has been emphasized

that the concept of critical ionic radius alone cannot explain the maximum oxygen-ion conductivity observed in Pm^{3+} -doped CeO_2 as found by the first-principles density functional theory calculations. Particular attention has been given to a more recent atomistic simulations study on rare-earth-doped ceria which calculates the migration energies for all the possible jump configurations that may present in rare-earth-doped CeO_2 . This study explains the importance of the shape of migration energy barrier and its impact on the ionic conductivity.

Acknowledgements

Author would like to acknowledge IIT Kanpur for supporting in writing this chapter.

Author details

Shobit Omar

Address all correspondence to: somar@iitk.ac.in

Department of Materials Science and Engineering, Indian Institute of Technology Kanpur, Kanpur, Uttar Pradesh, India

References

- [1] Inaba H, Tagawa H. Ceria-based solid electrolytes - review. *Solid State Ionics*. 1996;**83**:1-16
- [2] Steele BCH. Appraisal of $\text{Ce}_{1-y}\text{Gd}_y\text{O}_{2-y/2}$ electrolytes for IT-SOFC operation at 500° C. *Solid State Ionics*. 2000;**129**:95-110
- [3] Mogensen M, Sammes NM, Tompsett GA. Physical, chemical and electrochemical properties of pure and doped ceria. *Solid State Ionics*. 2000;**129**:63-94
- [4] Omar S, Nino JC. Consistency in the chemical expansion of fluorites: A thermal revision of the doped ceria. *Acta Materialia*. 2013;**61**:5406-5413
- [5] Tuller HL, Bishop SR. Tailoring material properties through defect engineering. *Chemistry Letters*. 2010;**39**:1226-1231
- [6] Koettgen J, Grieshammer S, Hein P, Grope BOH, Nakayama M, Martin M. Understanding the ionic conductivity maximum in doped ceria: Trapping and blocking. *Physical Chemistry Chemical Physics*. 2018;**20**:14291-14321
- [7] Zhu H, Ricote S, Coors WG, Chatzichristodoulou C, Kee RJ. Equilibrium and transient conductivity for gadolinium-doped ceria under large perturbations: II. Modeling. *Solid State Ionics*. 2014;**268**:198-207
- [8] Omar S, Wachsmann ED, Nino JC. Higher ionic conductive ceria based electrolytes for SOFCs. *Applied Physics Letters*. 2007;**91**:144106

- [9] Guo X, Waser R. Electrical properties of the grain boundaries of oxygen ion conductors: Acceptor-doped zirconia and ceria. *Progress in Materials Science*. 2006;**51**:151-210
- [10] Irvine JTS, Sinclair DC, West AR. Electroceramics: Characterization by impedance spectroscopy. *Advanced Materials*. 1990;**2**:132-138
- [11] Wang DY, Park DS, Griffith J, Nowick AS. Oxygen-ion conductivity and defect interactions in Ytria-doped ceria. *Solid State Ionics*. 1981;**2**:95-105
- [12] Yahiro H, Eguchi Y, Eguchi K, Arai H. Oxygen ion conductivity of the ceria-samarium oxide system with fluorite structure. *Journal of Applied Electrochemistry*. 1988;**18**:527-531
- [13] Yahiro H, Ohuchi T, Eguchi K, Arai H. Electrical-properties and microstructure in the system ceria alkaline-earth oxide. *Journal of Materials Science*. 1988;**23**:1036-1041
- [14] Zhang TS, Ma J, Kong LB, Chan SH, Kilner JA. Aging behavior and ionic conductivity of ceria-based ceramics: A comparative study. *Solid State Ionics*. 2004;**170**:209-217
- [15] Omar S, Wachsman ED, Jones JL, Nino JC. Crystal structure-ionic conductivity relationships in doped ceria systems. *Journal of the American Ceramic Society*. 2009;**92**:2674-2681
- [16] Andersson DA, Simak SI, Skorodumova NV, Abrikosov IA, Johansson B. Optimization of ionic conductivity in doped ceria. *Proceedings of the National Academy of Sciences of the United States of America*. 2006;**103**:3518
- [17] Balazs GB, Glass RS. AC-impedance studies of rare-earth-oxide doped ceria. *Solid State Ionics*. 1995;**76**:155-162
- [18] Butler V, Catlow CRA, Fender BEF, Harding JH. Dopant ion radius and ionic-conductivity in cerium dioxide. *Solid State Ionics*. 1983;**8**:109-113
- [19] Gerhardt-Anderson R, Nowick AS. Ionic conductivity of CeO₂ with trivalent dopants of different ionic radii. *Solid State Ionics*. 1981;**5**:547-550
- [20] Perez-Coll D, Marrero-Lopez D, Nunez P, Pinol S, Frade JR. Grain boundary conductivity of Ce_{0.8}Ln_{0.2}O_{2-d} ceramics (Ln = Y, La, Gd, Sm) with and without co-doping. *Electrochimica Acta*. 2006;**51**:6463-6469
- [21] Zając W, Molenda J. Electrical conductivity of doubly doped ceria. *Solid State Ionics*. 2008;**179**:154-158
- [22] Mogensen M, Lindegaard T, Hansen UR, Mogensen G. Physical properties of mixed conductor solid oxide fuel cell anodes of doped CeO₂. *Journal of the Electrochemical Society*. 1994;**141**:2122-2128
- [23] Omar S, Wachsman ED, Nino JC. A co-doping approach towards enhanced ionic conductivity in fluorite-based electrolytes. *Solid State Ionics*. 2006;**177**:3199-3203
- [24] Sánchez-Bautista C, Dos santos-García AJ, Peña-Martínez J, Canales-Vázquez J. The grain boundary effect on dysprosium doped ceria. *Solid State Ionics*. 2010;**181**:1665-1673
- [25] Tianshu Z, Hing P, Huang H, Kilner J. Ionic conductivity in the CeO₂-Gd₂O₃ system (0.05≤Gd/Ce≤0.4) prepared by oxalate coprecipitation. *Solid State Ionics*. 2002;**148**:567-573

- [26] Fuentes RO, Baker RT. Structural, morphological and electrical properties of Gd_{0.1}Ce_{0.9}O_{1.95} prepared by a citrate complexation method. *Journal of Power Sources*. 2009;**186**:268-277
- [27] Keqin H, Man F, Goodenough JB. Synthesis and electrical properties of dense Ce_{0.9}Gd_{0.1}O_{1.95} ceramics. *Journal of the American Ceramic Society*. 1998;**81**:357-362
- [28] Reddy KR, Karan K. Sinterability, Mechanical, Microstructural, and electrical properties of gadolinium-doped ceria electrolyte for low-temperature solid. *Journal of Electroceramics*. 2005;**15**:45-56
- [29] Cioateră N, Pârvulescu V, Rolle A, Vannier RN. Effect of strontium addition on europium-doped ceria properties. *Solid State Ionics*. 2009;**180**:681-687
- [30] Li LP, Lin XM, Li GS, Inomata H. Solid solubility and transport properties of Ce_{1-x}Nd_xO_{2-d} Nanocrystalline solid solutions by a sol-gel route. *Journal of Materials Research*. 2001;**16**:3207-3213
- [31] Aneflous L, Musso JA, Villain S, Gavarrri JR, Benyaich H. Effects of temperature and Nd composition on non-linear transport properties in substituted Ce_{1-x}Nd_xO_{2-d} cerium dioxides. *Journal of Solid State Chemistry*. 2004;**177**:856-865
- [32] Stephens IEL, Kilner JA. Ionic conductivity of Ce_{1-x}Nd_xO_{2-x/2}. *Solid State Ionics*. 2006;**177**:669-676
- [33] Zhu JX, Zhou DF, Guo SR, Ye JF, Hao XF, Cao XQ, Meng J. Grain boundary conductivity of high purity neodymium-doped ceria nanosystem with and without the doping of molybdenum oxide. *Journal of Power Sources*. 2007;**174**:114-123
- [34] Yamazaki S, Matsui T, Sato T, Arita Y, Nagasaki T. EXAFS study of reduced ceria doped with lanthanide oxides. *Solid State Ionics*. 2002;**154-155**:113-118
- [35] Yamazaki S, Matsui T, Ohashi T, Arita Y. Defect structures in doped CeO₂ studied by using XAFS spectrometry. *Solid State Ionics*. 2000;**136-137**:913-920
- [36] Deguchi H, Yoshida H, Inagaki T, Horiuchi M. EXAFS study of doped ceria using multiple data set fit. *Solid State Ionics*. 2005;**176**:1817-1825
- [37] Ohashi T, Yamazaki S, Tokunaga T, Arita Y, Matsui T, Harami T, Kobayashi K. EXAFS study of Ce_{1-x}Gd_xO_{2-x/2}. *Solid State Ionics*. 1998;**113-115**:559-564
- [38] Jain P, Avila-Paredes HJ, Gapuz C, Sen S, Kim S. High-resolution 89Y and 45Sc NMR spectroscopic study of short-range structural order in Nanocrystalline Y- and Sc-doped CeO₂ and ZrO₂. *The Journal of Physical Chemistry C*. 2009;**113**:6553-6560
- [39] Kilner JA, Waters CD. The effects of dopant cation-oxygen vacancy complexes on the anion transport properties of non-stoichiometric fluorite oxides. *Solid State Ionics*. 1982;**6**:253-259
- [40] Rai A, Mehta P, Omar S. Ionic conduction behavior in Sm_xNd_{0.15-x}Ce_{0.85}O_{2-d}. *Solid State Ionics*. 2014;**263**:190-196

- [41] Nowick AS, Lee WK, Jain H. Survey and interpretation of pre-exponentials of conductivity. *Solid State Ionics*. 1988;**28**:89-94
- [42] Omar S, Wachsmann ED, Nino JC. Higher conductivity Sm³⁺ and Nd³⁺ co-doped ceria-based electrolyte materials. *Solid State Ionics*. 2008;**178**:1890-1897
- [43] Nowick AS, Wang DY, Park DS, Griffith J. Oxygen-ion conductivity and defect structure of CeO₂ doped with CaO and Y₂O₃. In: Vashishta P, Mundy JN, Shenoy GK, editors. *Fast Ion Transport in Solids: Electrodes and Electrolytes*. Amsterdam: Elsevier, North-Holland Publishing Co.; 1979
- [44] Zhan ZL, Wen TL, Tu HY, Lu ZY. AC impedance investigation of samarium-doped ceria. *Journal of the Electrochemical Society*. 2001;**148**:A427-A432
- [45] Kilner JA, Brook RJ. A study of oxygen ion conductivity in doped nonstoichiometric oxides. *Solid State Ionics*. 1982;**6**:237-252
- [46] Kim DJ. Lattice-parameters, ionic conductivities, and solubility limits in fluorite-structure MO₂ oxide (M = Hf⁴⁺, Zr⁴⁺, Ce⁴⁺, Th⁴⁺, U⁴⁺) solid-solutions. *Journal of the American Ceramic Society*. 1989;**72**:1415-1421
- [47] Hong SJ, Virkar AV. Lattice-parameters and densities of rare-earth-oxide doped ceria electrolytes. *Journal of the American Ceramic Society*. 1995;**78**:433-439
- [48] Butler V, Catlow CRA, Fender BEF, Harding JH. Dopant ion radius and ionic conductivity in cerium dioxide. *Solid State Ionics*. 1983;**8**:109-113
- [49] Minervini L, Zacate MO, Grimes RW. Defect cluster formation in M₂O₃-doped CeO₂. *Solid State Ionics*. 1999;**116**:339-349
- [50] Murray AD, Murch GE, Catlow CRA. A new hybrid scheme of computer simulation based on Hades and Monte Carlo: Application to ionic conductivity in Y³⁺ doped CeO₂. *Solid State Ionics*. 1986;**18-19**:196-202
- [51] Nakayama M, Martin M. First-principles study on defect chemistry and migration of oxide ions in ceria doped with rare-earth cations. *Physical Chemistry Chemical Physics*. 2009;**11**:3241-3249

Prototyping a Gas Sensors Using CeO₂ as a Matrix or Dopant in Oxide Semiconductor Systems

Lucian Pîslaru-Dănescu, Gabriela Telipan,
Ioana Ion and Virgil Marinescu

Additional information is available at the end of the chapter

<http://dx.doi.org/10.5772/intechopen.80801>

Abstract

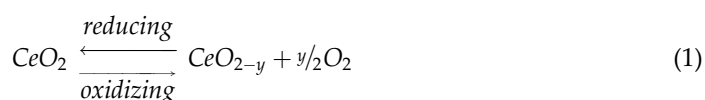
In this chapter, two important aspects of using CeO₂ in the field of gas sensors are presented. Firstly, for CO₂ detection in the range of 0–5000 ppm, a binary semiconductor oxides CeO₂-Y₂O₃ was used. Secondly, as a dopants, in oxide semiconductor systems, used to detect the NO₂. In this case, CeO₂ is used as a dopant in hybride composite, consisting of reduced graphene oxide/ZnO, in order to increase the sensibility in NO₂ detection at low concentration in the range of 0–10 ppm. The structural and morphological characterization of sensitive materials by X-ray diffraction, SEM, adsorption desorption isotherms, thermal analysis and RAMAN spectroscopy are presented. Also, the sensing element of the sensor that detects the NO₂ is achieved by depositing the nanocomposite material on the interdigital grid. The electronic conditioning signal from the sensing element is achieved by using a Wheatstone bridge together with an instrumentation operational amplifier.

Keywords: ceria oxide, yttrium oxide, zinc oxide, reduced graphene oxide, sensing element, electronic conditioning, X-ray diffraction, scanning electron microscopy

1. Introduction

Cerium represents one of the most abundant elements in the Earth's crust (66.5 ppm) than copper (60 ppm) or tin (2.3 ppm). Ce possesses an unique electronic configuration ([Xe] 4f²6s²), and presents two common valence states Ce³⁺ and Ce⁴⁺ [1–3], which give CeO₂ excellent chemical and physical properties: 1/4 O₂, at most, can be released from each CeO₂ unit cell. It serves as an active oxygen donor in many reactions, such as three-way catalytic reactions to eliminate toxic

automobile exhaust [1, 4], the low-temperature water gas shift reaction [1, 5], oxygen sensors, oxygen permeation membrane systems and fuel cells [1, 6]. Cerium oxide CeO_2 is a semiconductor oxide with a band gap energy (3.19 eV) [7, 8]. The crystalline structure consists of a cubic fluorite structure (Fm3m) with a cell parameter of 5.41 Å at room temperature and presents a high dielectric constant $\epsilon = 26$, almost of silicon, that it makes use in spintronic devices with silicon microelectronic devices [9, 10]. Synthesis of CeO_2 nanoparticles comprise various methods as: solvothermal [2, 11, 12], sol gel [2, 13, 14], sonochemical [2, 15], hydrolysis [2, 16], hydrothermal [2, 17, 18], precipitation [2, 19] and reverse micelles [2, 20]. The dual oxidation state mentioned above means that these nanoparticles have oxygen vacancies or defects [19]. The loss of oxygen and the reduction of Ce^{4+} to Ce^{3+} in accord with Eq. 1, is accompanied by creation of an oxygen vacancy. This property is responsible for the interesting redox chemistry exhibited by ceria nanoparticles and makes them attractive for many catalytic applications [21].



Also all ceria applications are based on its potential redox between Ce^{3+} and Ce^{4+} , high oxygen affinity and absorption/excitation energy bands associated with the electronic structure [22]. Another important property of CeO_2 consists in their ability to release and absorb oxygen during alternating redox conditions and hence to function as oxygen buffer. The addition of dopants leads to increase of concentration of oxygen vacancies and improves the thermal stability of the parent oxide [23]. Also, CeO_2 presents a great chemical stability and high diffusion coefficient with values between 10^{-8} and 10^{-6} cm^2/s in the temperature range of 800–2200 K coming from oxygen vacancies (V_o has been used for gas sensing for oxygen, NO_x , acetone and H_2S sensors). Besides, CeO_2 is also used for improving sensing properties of semiconductor oxides such as ZnO , TiO_2 and In_2O_3 [24, 25]. On the other hand, the ionic conductivity of CeO_2 is improved by doping with rare earth oxides such as Sm_2O_3 , Gd_2O_3 and Y_2O_3 and the size of conductivity of the doped ceria depends on the ionic radius of the doping ion. The introduction of trivalent ions in ceria leads to production of anion vacancies

Sensitive material	Gas detected	Range concentration, [ppm]/[%]	Operation temperature, [°C]	Detection limit, [ppm]	Response/recovery time, [s]	Ref.
$\text{CeO}_2\text{-SnO}_2$	CO	0–500 ppm	430	<5	26/30	[27]
$\text{ZnO/Al}_2\text{O}_3\text{/CeO}_2$	ethanol	0–2000 ppm	260	*	2/10	[28]
$\text{CeO}_2\text{-Fe}_2\text{O}_3$	methanol	1–1000 ppm	400	1–3	*	[29]
CeO_2	formaldehyde	0.5–50 ppm	30	—	36/1	[30]
CeO_2 activated ZnO-TiO_2	CO_2	286 ppm exposure	290	*	24/72	[31]
$\text{Ce}_{(1-x)}\text{Zr}_x\text{O}_2$	O_2	1–100%	500–700	*	*	[32]

*Data unavailable.

Table 1. Gas detection with sensitive materials based on CeO_2 .

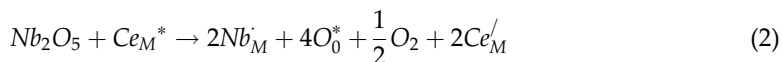
which may enhance catalytic and gas sensing properties [26]. In **Table 1**, several sensitive materials based on ceria for gas detection and their gas sensing characteristics is presented.

As doping with other ions could lead to enhanced activity for different reasons. Ceria doped with pentavalent ions as Nb, could insert extra oxygen anions that would be more easily removed [26]. In this chapter, the mixed oxides CeO₂-Nb₂O₅, Y₂O₃-doped CeO₂ as sensitive materials for CO₂ detection and sensitive materials composed from CeO₂-doped rGO (reduced graphene oxide) and CeO₂-doped rGO-ZnO for NO₂ detection are presented.

To conditioning the signal provided by sensing element, high-performance electronic circuits such as precision operational amplifiers, digital analogue converters and analog multipliers have been used [33, 34].

2. Sensor for CO₂ detection with mixed binary oxide CeO₂-Nb₂O₅ sensitive material

Niobium oxide has some properties that make it in principal as promising for catalytic applications. Niobia-based materials are effective catalysts in selective oxidation reactions due to its redox properties. Also, niobia-doped ceria materials have shown a good carbon deposition and excellent properties as solid oxide fuel cell (SOFC) anodes [35]. Nb⁵⁺ ions (ionic radius of Nb⁵⁺: 78 pm) may initiate the reduction of Ce⁴⁺ to Ce³⁺ by the doping Nb into the CeO₂ structure, which results in formation of oxygen vacancies. Using the Kröger-Vink notation, it can mention two mechanisms for the dissolution: one of which occurs by electronic compensation (Eq. 2) and the other by consumption of vacancies (Eq. 3), as shown below [3, 36, 37].



where O_o^* , $V_o^{\cdot\cdot}$ represent oxygen and oxygen vacancies on the oxygen sites, Ce_M^* , Ce_M^{\prime} represent cerium (Ce⁴⁺) and negatively charged cerium ions (Ce³⁺) on metal sites M, Nb_M^{\cdot} metal vacancy. Nb₂O₅ it is known as an n-type oxide semiconductor with a band gap about 3.4 eV. Because of its good physicochemical properties and structural isotropy, it is used in other range of applications such as: in construction of gas sensing, field-emission displays and microelectronics electrochromics display and photoelectrodes [38].

2.1. Synthesis of mixed oxides CeO₂-Nb₂O₅ sensitive material

In our case, we used the mixed binary oxides CeO₂-Nb₂O₅ for CO₂ detection. Sensitive element is composed from mechanical mixing of CeO₂ (97%) and Nb₂O₅ (3%); both reagents purchased from Merck. The powder oxides were treated with a few drops of ethylic alcohol for ink obtaining and then introduced in a ball mill for homogenization followed by calcination at 500, 600 and 800°C for 1 hour. The powder calcined at 600°C was pressed in disc form at 2 tons force/cm² with the dimensions Ø4 × 1 mm and mounted on the ambasis transistor. The sensor image is showed in **Figure 1** [39].



Figure 1. Image of the CO₂ sensor made with mixed oxides CeO₂-Nb₂O₅ sensitive material.

2.2. Structural characterization

Calcined mixed powder oxides were characterized by X-ray diffraction using a diffractometer-type X Bruker-AXS type D8 ADVANCE in conditions: CuK_α radiation ($\lambda = 1.54059 \text{ \AA}$), 40 kV/40 mA, filter k_β of Ni. pas: 0.04°, measuring time on point: 1 s, measure range $2\theta = 10\text{--}100^\circ$. The mixed oxides powder with composition CeO₂-3%Nb₂O₅ was calcined at 500, 600 and 800°C for 1 hour. It shows a cubic phase for CeO₂ and orthorhombic phase for Nb₂O₅, **Figure 2**. Also, for this powder that was calcined at 800°C, was identified in addition a hexagonal Ce₂O₃ phase (**Figure 3**). It obtain for CeO₂ cell parameter $a = b = c = 5.407 \text{ \AA}$. This is in accord with

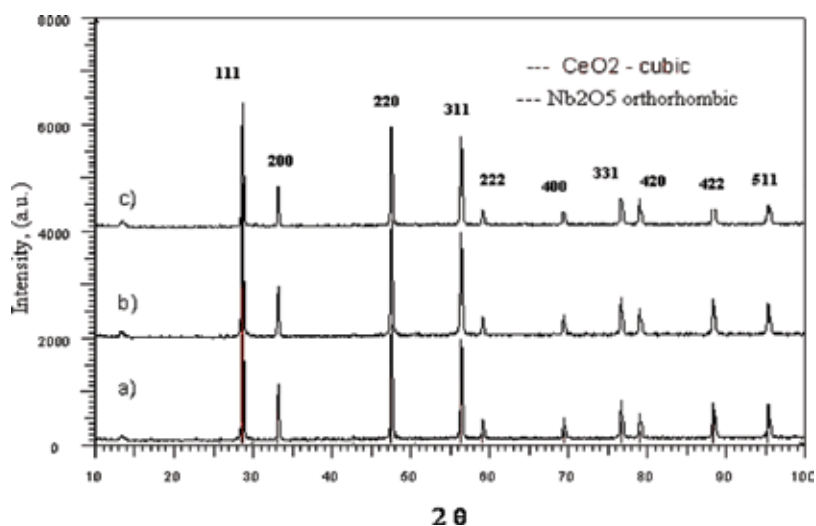


Figure 2. X-ray diffraction of CeO₂-Nb₂O₅ calcinated at: (a) 500°C; (b) 600°C and (c) 800°C.

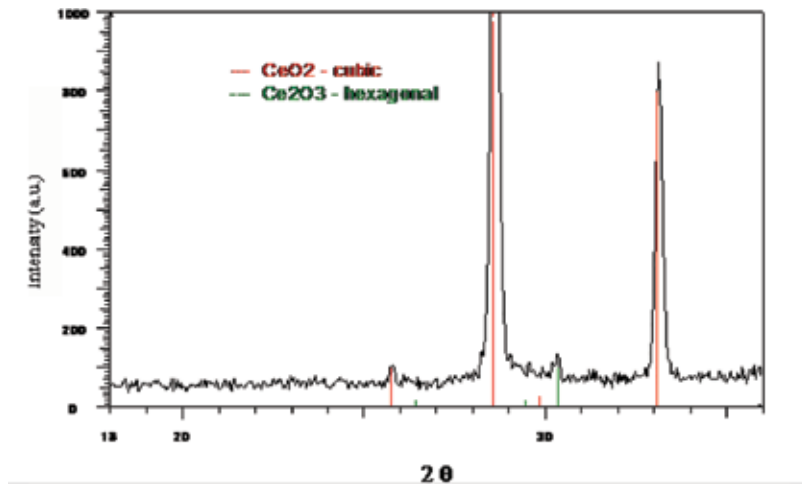


Figure 3. X-ray diffraction of CeO₂-Nb₂O₅ calcinated at 800°C.

theoretical value of $a = 5.404 \text{ \AA}$ as well as in according with card number 03-065-5923. The cell parameters for Nb₂O₅ orthorhombic phase were $a = 6.175 \text{ \AA}$, $b = 29.175 \text{ \AA}$ and $c = 3.930 \text{ \AA}$ in accord with card number 30-0873 [4]. Corresponding to hkl (Miller indices) 111, 200, 220 and 311, the crystallites size determined with Scherrer formula give values of 160.9, 145.6, 117.4 and 63.5 nm.

2.3. CO₂ gas sensor made with mixed oxides CeO₂-Nb₂O₅ sensitive material tested in automated process mode

The gas sensors testing were performed with the apparatus as presented in **Figure 4**. It is realized by SYSCOM-18 Romania for National Institute for Research and Development in



Figure 4. The testing gas sensor installation.

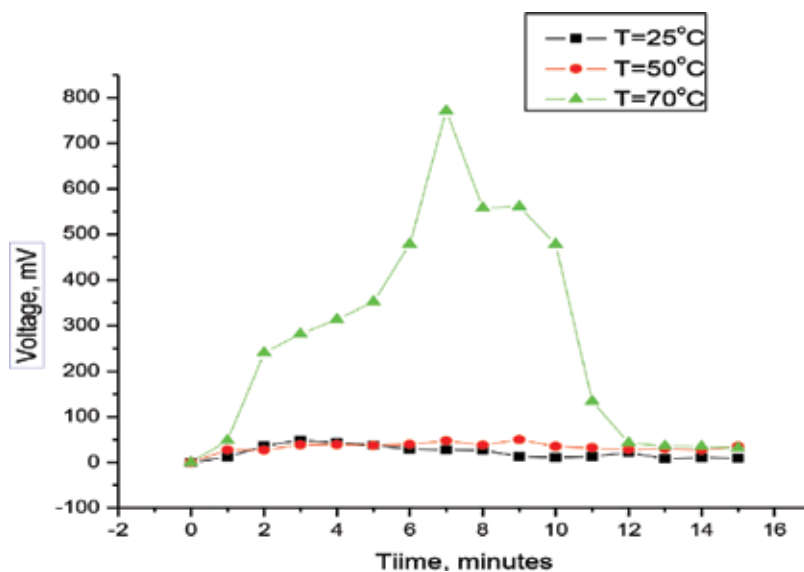


Figure 5. Variation of the voltage depending on time for CO₂ sensor, made with mixed oxides CeO₂-Nb₂O₅ sensitive material.

Electrical Engineering ICPE-CA. The voltage measurements were effected by testing module, in automated process mode. A control panel provides a lot of measuring values, at rate 1/10 s. The bench of testing for the gas sensor consists in an enclosure where there are set of testing conditions for the sensor as well as in connected equipment. The whole process of testing is automated, being controlled by a programmable automaton. The gas for testing is introduced in a controlled way in the testing enclosure, through a mass debit meter. In the testing, enclosure is set a constant temperature, controlled by a temperature regulator.

The gas testing was done in concentration of 10,000 ppm CO₂ at the 25, 50 and 70°C chamber test temperature. The sensor was developed the voltages values of 48, 50 and 770 mV (**Figure 5**) [39].

The experimental data shows a good sensor response for CO₂ detection with increasing temperature.

2.4. Signal conditioning of the sensing element for CO₂ detection with mixed binary oxide CeO₂-Nb₂O₅ sensitive material

The Analog Devices AD620 operational amplifier is used to build the signal conditioning electronic module, provided by the sensing element. A preamp section comprised of Q1 and Q2, **Figure 6**, provides additional gain up front. Feedback through the Q1-A1-R1 loop and the Q2-A2-R2 loop maintains a constant collector current through the input devices Q1 and Q2, thereby impressing the input voltage across the external gain setting resistor, R_G.

This creates a differential gain from the inputs to the A1/A2 outputs given by Eq. (4):

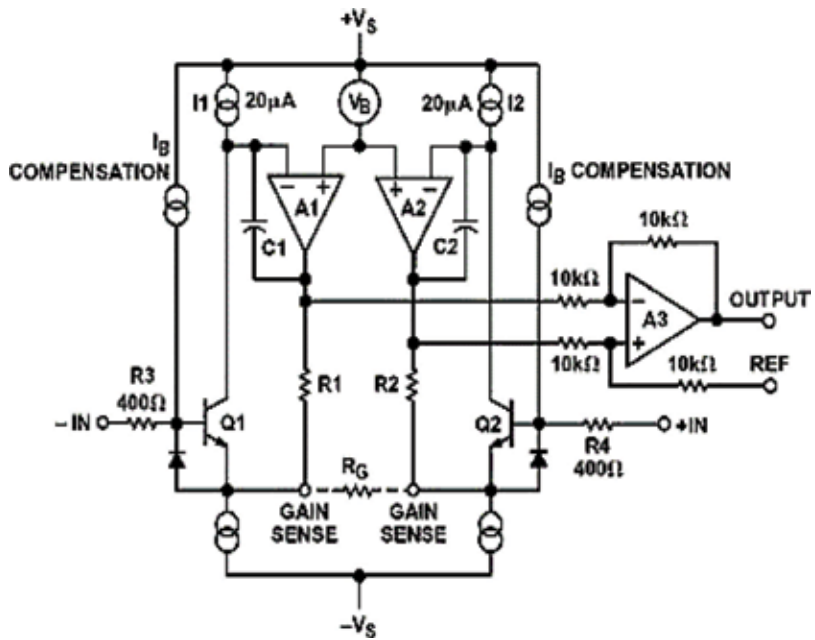


Figure 6. A simplified schematic of the AD620 [39].

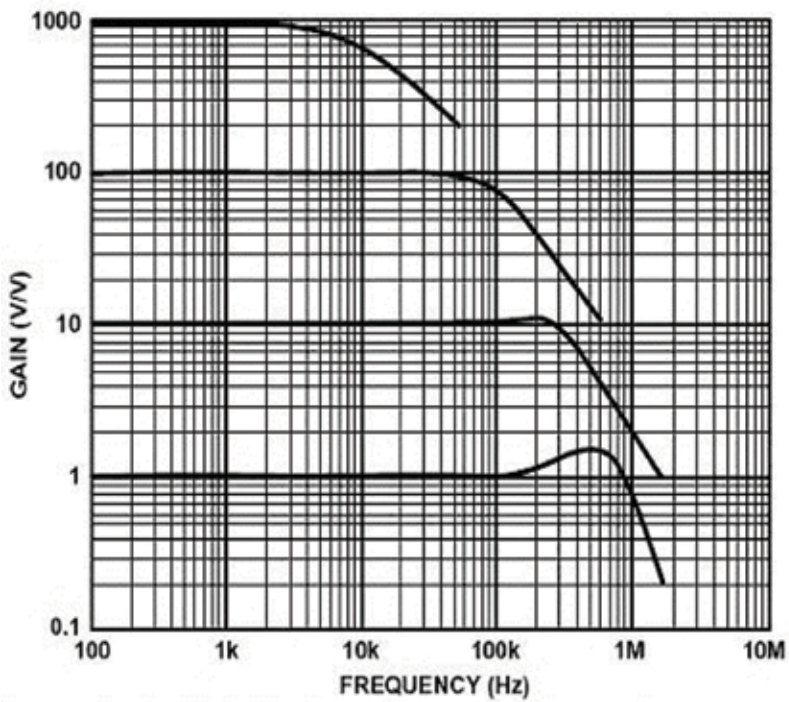


Figure 7. AD620 closed-loop gain versus frequency [39].

$$G = \frac{R1 + R2}{R_G} + 1 \tag{4}$$

The unity-gain subtractor, A3, removes any common-mode signal, yielding a single-ended output referred to the REF pin potential. The value of R_G also determines the transconductance of the preamp stage [34]. As R_G is reduced for larger gains, the transconductance increases asymptotically to that of the input transistors. The open-loop gain is boosted for increasing programmed gain, thus reducing gain related errors. Also, the gain bandwidth product (determined by C1, C2 and the preamplifier transconductance, **Figure 6**) increases with programmed gain, thus optimizing the amplifier’s frequency response. In **Figure 7**, the closed-loop gain of AD620 versus frequency is shown. Finally, the input voltage noise is reduced to $9 \text{ nV}/\sqrt{\text{Hz}}$, which is determined mainly by the collector current and base resistance of the input devices. The internal gain resistors, R1 and R2, are laser trimmed to an absolute value of $24.7 \text{ k}\Omega$, allowing the gain to be programmed accurately with a single external resistor. The gain equation is Eq. (5).

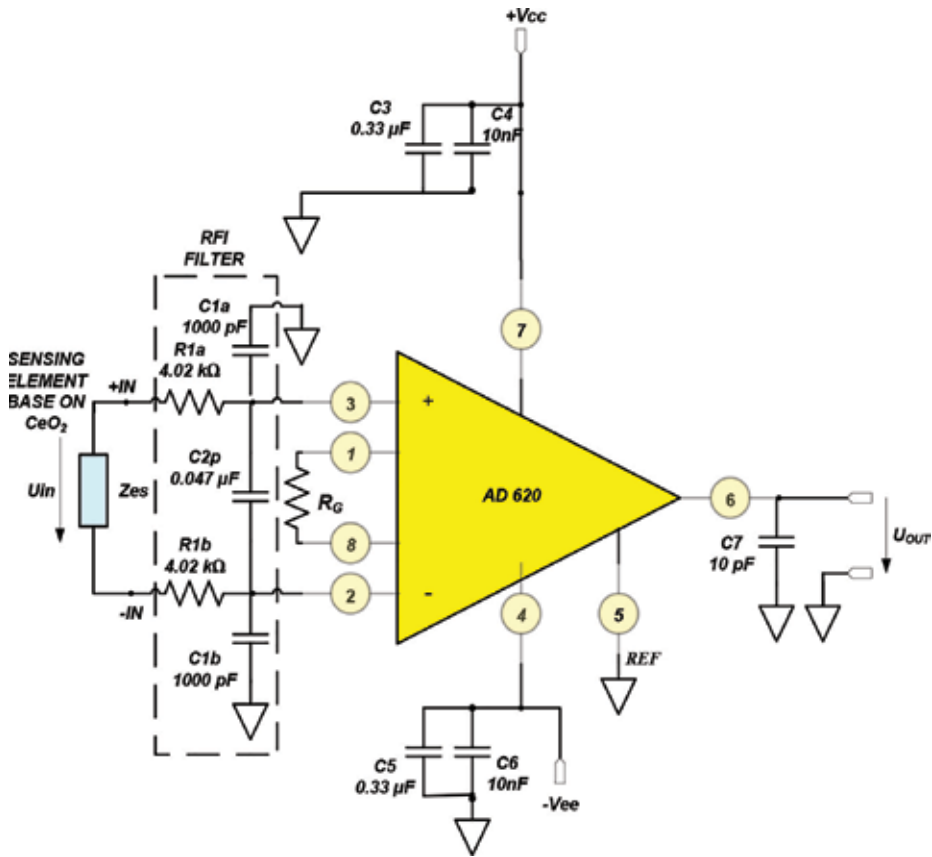


Figure 8. The electronic module for signal conditioning provided by sensing element, designing with AD620 analog devices.

$$G = \frac{49.4k\Omega}{R_G} + 1 \quad (5)$$

So that,

$$R_G = \frac{49.4k\Omega}{G - 1} \quad (6)$$

where the resistor R_G in $k\Omega$, according to Eq. (6).

The value of 24.7 $k\Omega$ was chosen so that standard 1% resistor values could be used to set the most popular gains. For the input resistors, R_{1a} and R_{1b} were used, capacitor C_{2p} approximately five times to 0.047 μF to provide adequate RF attenuation (**Figure 8**). With the values shown, the circuit -3 dB bandwidth is approximately 400 Hz and noise levels 12 nV/\sqrt{Hz} . It requires the circuitry preceding the in-amp to drive a lower impedance load and results in somewhat less input overload protection. The output signal V_{OUT} (**Figure 8**) is a common mode voltage, picked at the output of the operational amplifier. The capacitor groups, 0.01 μF and 0.33 μF make a decoupling of the supply voltage (**Figure 8**) in the immediate closeness of the operational amplifiers. The supply voltage $+V_{cc}$ and $-V_{ee}$, respectively, stabilized is differentiated, $\pm 15V_{cc}$ in comparison with the reference potential bar.

3. Sensor for CO₂ detection with Y₂O₃-doped CeO₂ sensitive material

The ion conductivity of CeO₂ can be significantly improved upon substitution with some trivalent oxides of lanthanides like Y₂O₃, Sm₂O₃ and Gd₂O₃, because the number of oxygen vacancy will be considerably increased for charge compensation. The electrical conductivity in doped ceria is influenced by factors such as: the dopant ion, the dopant concentration, the oxygen vacancy concentration and the defect association enthalpy. An example is constituted by combination Y₂O₃-doped CeO₂ which has been used usually as the solid electrolyte for moderate temperature solid oxide fuel cells [40]. In our case, we used the Y₂O₃-doped CeO₂ as sensitive material for CO₂ detection. For Y₂O₃-CeO₂ synthesis, it utilizes several methods such as hydrothermal [41], electrospinning [23], thermolysis [42] and sol gel [43].

3.1. Synthesis method

Sol gel method applied for synthesis of Y₂O₃-doped CeO₂ sensitive material, is in accord with ref. [44] and used as starting reagents Ce(SO₄)₂ × 4H₂O (97% purity, Merck) and Y(NO₃)₃ × 3H₂O (98% purity Karlsruhe GmbH in molar ratio CeO₂/Y₂O₃ = 4:1). The salts were dissolved in deionized water. To 100 ml salt solution, 25 ml solution of 1 M citric acid as chelating agent was added. To obtain gel, the salt solution was heated to 70°C under constant stirring. To this solution, 40 ml ethylene glycol was added to promote citrate polymerization and heated at 90°C. The gel formed was filtered, washed and heat treated in oven at 100°C. The powder obtained was calcined at 800°C for 2 hours. The powder was pressed to disc form using 10 ton force/cm², with dimensions diameter 4 mm, height 1 mm and then sinterized at 1100°C for 6 hours [44].

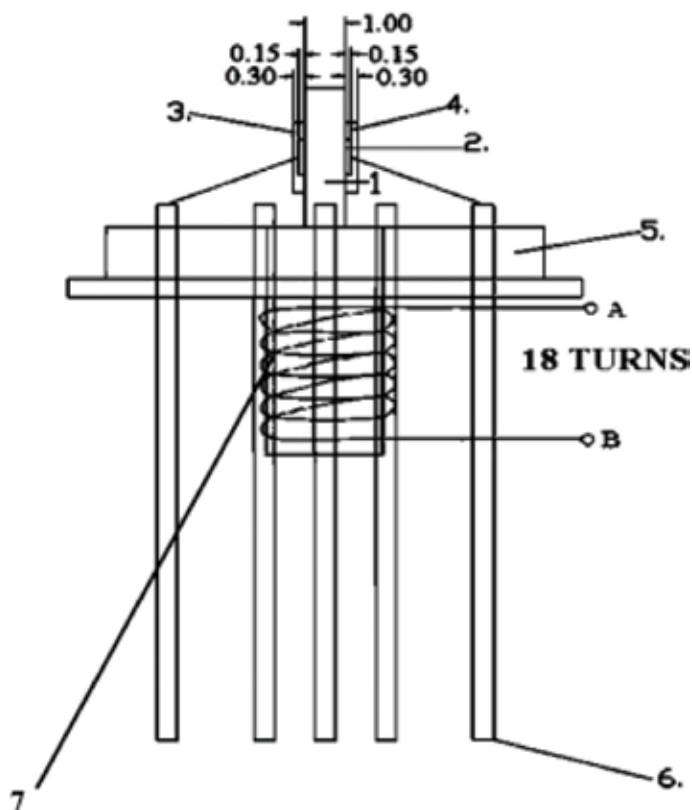


Figure 9. CO₂ sensor, component parts: 1. Ce₂O₂-Y₂O₃ disc; 2. Gold electrode, thin film deposition of Au, in the form of the disc; 3. Ag micro-wire connections; 4. The positioning piece; 5. TO-8 package plated base; 6. The pins; 7. A, B terminals of 18 turns heating resistance.

3.2. The construction of the sensor for CO₂ detection designed with Y₂O₃-doped CeO₂ sensitive material

On both sides of disc, gold electrodes in circular form with diameter of 1 mm was deposited. The gold was deposited by e-beam evaporation method using Baltzer equipment with conditions: pressure $P = 10^{-5}$ Torr and current $I = 8$ mA, for 60 s time deposition. The disc with electrodes deposited was mounted on a 12 pin TO-8 package base. Below the base, the heater element composed of Ni wire with a diameter of 0.1 mm was placed, the winding is composed from 18 turns with a diameter of $d = 3$ mm. **Figure 9** shows how it built the CO₂ sensor [44].

3.3. Structural and morphological characterization of sensitive material Y₂O₃-doped CeO₂

Thermal analysis was performed with NETZSCH STA 409 simultaneous thermogravimetric balance, in the analysis conditions: inert atmosphere of argon, heating rate of 10°C/min in alumina crucible and the mass sample was 15.7 mg. **Figure 10** presents the thermal analysis TG, DTA and differential thermogravimetry (DTG) curves for the dried gel. The DTA curve

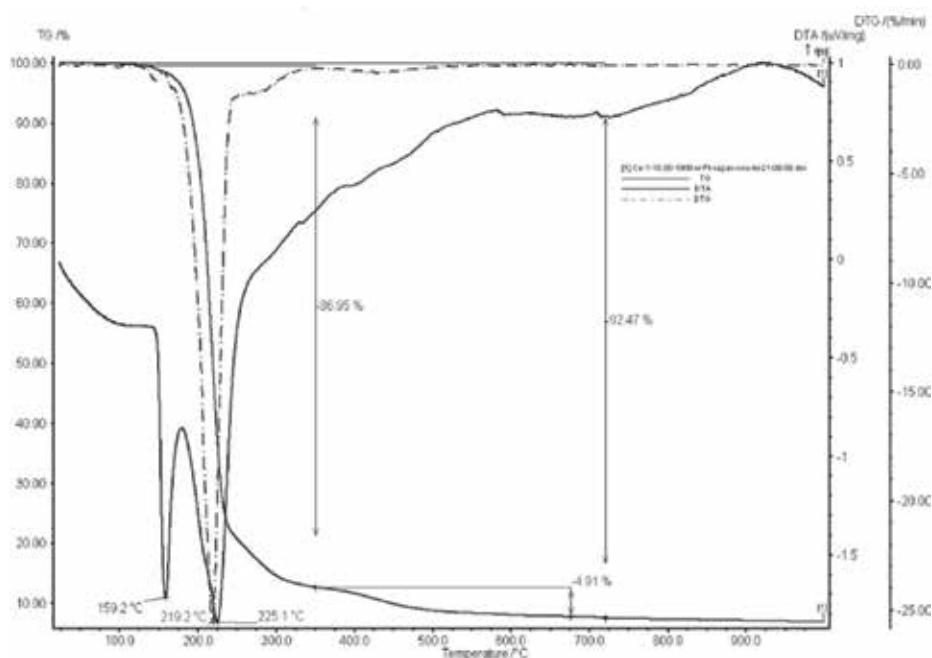


Figure 10. Thermal analysis TG, DTA and DTG curves for dried gel of CeO₂-Y₂O₃.

releases two endothermic peaks at 159.2 and 225.1°C. The last one has a correspondent in DTG curve at 219°C, the total mass loss was 86.95% from initial mass. Other thermal transformation appears at 430°C which represents on in a TG curve a loss of 4.91% which correspond to the decomposition of precursors, consisting in cerium sulfate and yttrium nitrate and in the end only Ce-Y-related oxides are obtained [44].

The X-ray diffraction patterns of the CeO₂-Y₂O₃ oxides powder calcinations at 800°C for 2 hours are shown in **Figure 11**. For comparison, **Figure 12** shows the X-ray diffraction for commercial CeO₂ powder. For this oxides system, the XRD pattern reveals the formation of well crystallized phases, CeO₂ indexed with the cubic fluorite structure and Y₂O₃ with cubic structure. Also, a secondary phase with cubic structure and composition Ce_{0.6}Y_{0.4}O_{1.8} was identified [44].

Table 2 presents X-ray parameters for Y₂O₃-doped CeO₂, cell parameters and crystallite sizes determined with Scherrer formula.

The morphological structure of Y₂O₃-doped CeO₂ was investigate by SEM measurements using FESEM-FIB type Auriger model Carl Zeiss SMT GmbH at a high voltage acceleration of 2 and 3 kV. The SEM sample morphology was investigated trough SESI (combined detector in SEM chamber–Evernhart Thornley type with Faraday cup). **Figure 13** shows the SEM image for disc CeO₂-Y₂O₃ sintered, where it can be seen as a relative homogeneous structure and the crystallite sizes of CeO₂ and Y₂O₃ were in range of 26–54 nm in good accord with X-ray diffraction analysis. **Figure 14** shows the SEM images for CeO₂-Y₂O₃ powder calcined at

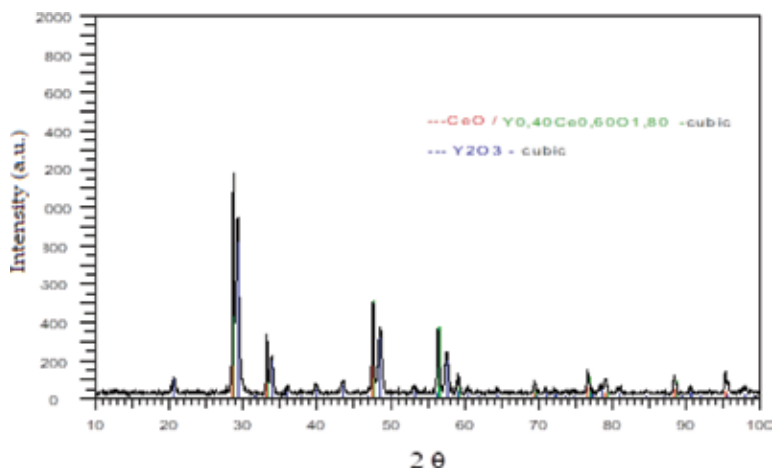


Figure 11. X-ray diffraction of Y_2O_3 -doped CeO_2 synthesized by sol gel method.

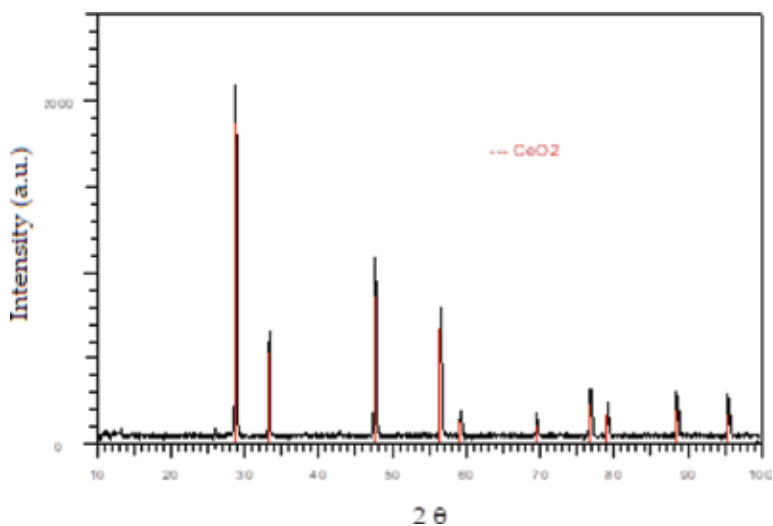


Figure 12. X-ray diffraction for commercial CeO_2 .

800°C for 2 hours, where it can be seen a nonhomogeneous structure composed by agglomerates [44].

N_2 adsorption-desorption isotherms were performed with the AUTOSORB-1, Quantachrome Instruments, United Kingdom in the following conditions: working gas N_2 , measured temperature: $-196^\circ C$ and relative pressure range $P/P_0 = 0.001-0.99$. For binary oxides $CeO_2-Y_2O_3$, powder calcined at 800°C for 2 hours, BET analysis revealed the results: the specific surface area was $3.13 \text{ m}^2/\text{g}$, the total volume of the pores was $1.066 \times 10^{-3} \text{ cm}^3/\text{g}$ and pore sizes of 8.93 Å. There is a specific ratio $P/P_0 = 0.02898$ for the pores with diameters smaller than 6.9 Å [44].

Phase	Crystal structure	Unit cell parameter (Å) a = b = c		2θ	Crystalline face indexes hkl	Crystallites-size (nm)
		Experimental	Theoretic card no.:			
CeO ₂	Cubic	5.41325	5.41100 PDF 01-071-4199	28.536	111	48.1
Y ₂ O ₃	Cubic	10.61131	10.61060 PDF 01-076-8044	29.121	222	27.0
Y _{0.4} Ce _{0.6} O _{1.8}	Cubic	5.39449	5.39300 PDF 01-075-0177	28.639	111	49.2
CeO ₂ Merck	Cubic	5.384			111	154.9

Table 2. X-ray parameters for Y₂O₃-doped CeO₂.

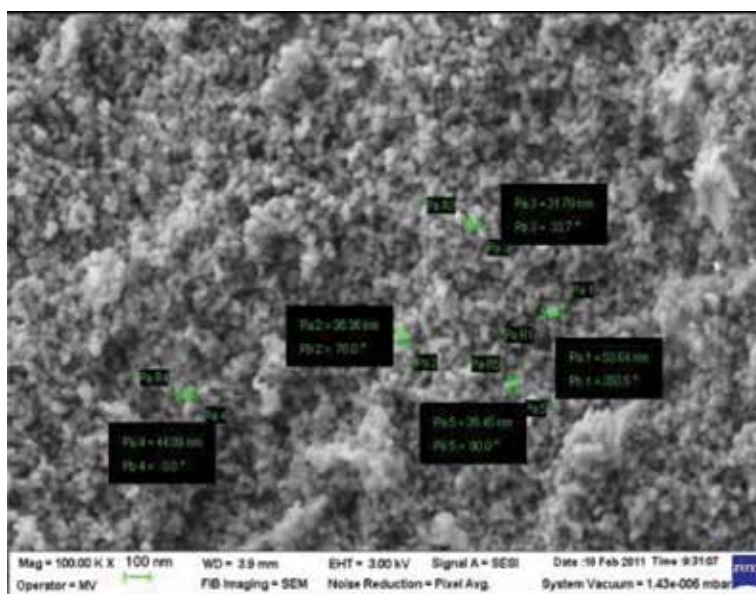


Figure 13. SEM images for sintering disc CeO₂-Y₂O₃.

3.4. The CO₂ gas sensing mechanism and gas sensors testing

The improved sensing response at CO₂ can be attributed to synergistic effects between Y₂O₃-doped CeO₂. In certain conditions such as high temperature, reduced state or pure CeO₂, lose some amount of oxygen and generate oxygen vacancies in accord with Eq. (7),



When CO₂ comes in contact with CeO₂-activated surface, this forms carbonates as a product through the participation of surface oxide ions in accordance with Eq. (8),

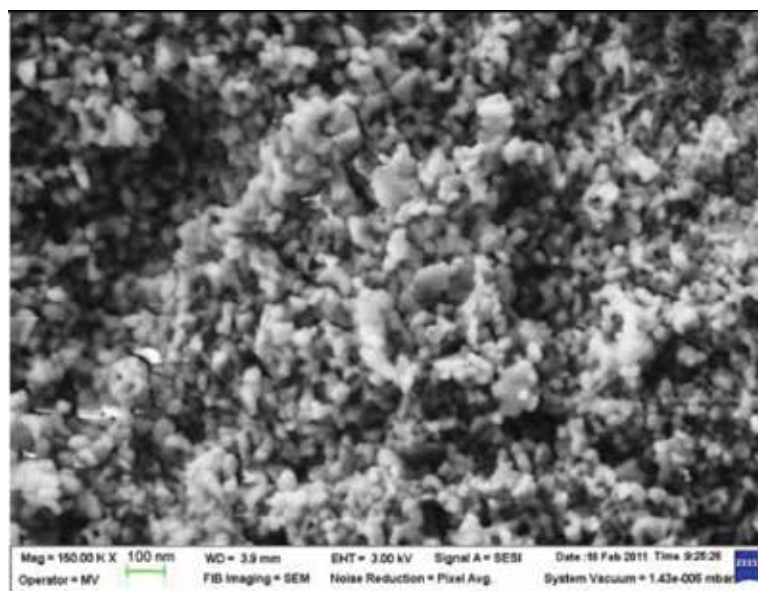


Figure 14. SEM images for oxidic powder $\text{CeO}_2\text{-Y}_2\text{O}_3$ calcined at 800°C for 2 hours.



The carbonates disappear when they are exposed to oxidizing conditions [31]. The sensor characteristic was performed using test installation presented in **Figure 4**. The sensor was exposed at CO_2 atmospheres in the concentration range of 0–5000 ppm CO_2 in the climatic conditions: $T = 20^\circ\text{C}$ and two relative humidity testing 40% RH and 80% RH, respectively. The sensor functions at 135°C , temperature provided by the heating resistance (**Figure 9**, Pos. 7). **Figure 15** shows the variation of sensor voltage with the gas concentration. The characteristics show a slow linear decreasing of voltage with CO_2 concentration which allows an easy signal conditioning. In the concentration range 0–5000 ppm CO_2 , the sensor presents a voltage variation as follows: 378.17–377.32 mV for $T = 20^\circ\text{C}$, RH 40% and 377.11–376.61 mV for $T = 20^\circ\text{C}$, RH 80%. The sensor data show a little dependence of voltage with relative humidity that makes usable in environment with high relative humidity. The sensitivity of the sensor was 0.3 V/ppm and the response time was less than 30 s [44].

3.5. Signal conditioning of the sensing element for CO_2 gas detection with Y_2O_3 -doped CeO_2 sensitive material

The operational amplifier ADA4627-1, provided by analog devices (**Figure 16**) is a broadband and high precision amplifier. It is recommended in applications like “sensor conditioning” and electronic conditioning of the signal, due to its exceptional attributes: low noise, very low offset voltage, very high common-mode rejection ratio (CMMR) and very high slew rate. This operational amplifier combines the best “DC” features and very good dynamic characteristics

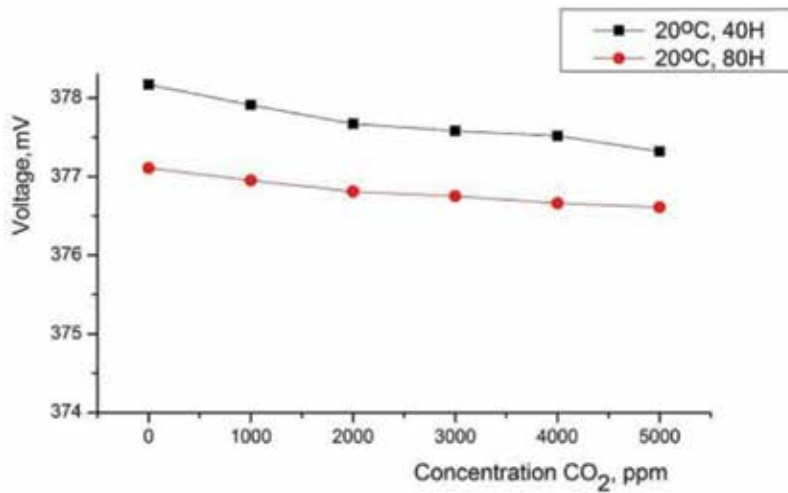


Figure 15. The sensor voltage function with CO₂ concentration, for $T = 20^{\circ}\text{C}$ and two relative humidity testing 40% RH and 80% RH, respectively.

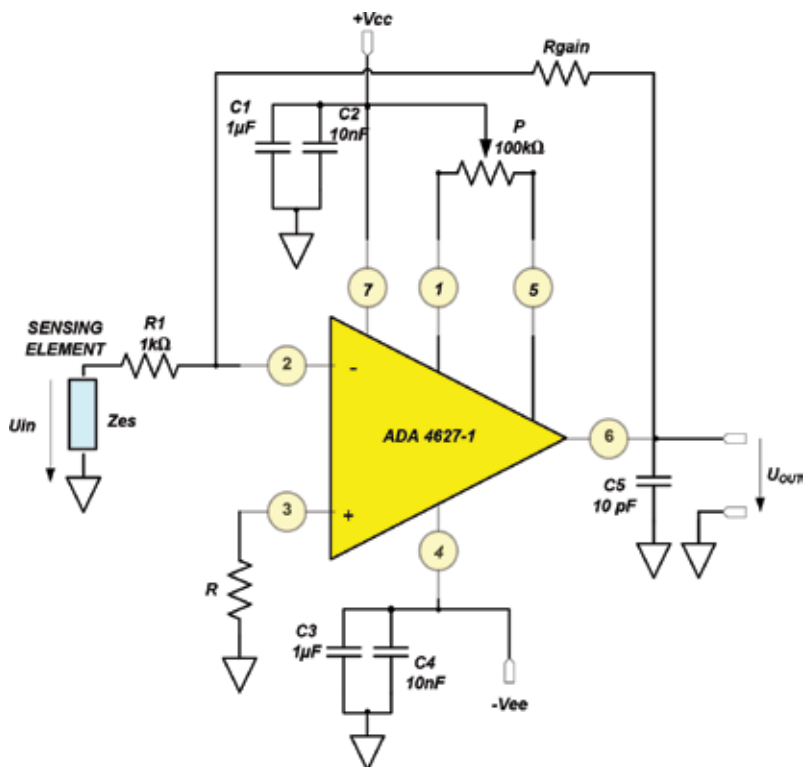


Figure 16. The electronic module for signal conditioning provided by sensing element, designing with ADA4627-1 analog devices.

[33], like: slew rate 60 V/ μ s; extended range of differential supply voltage: ± 5 Vcc ± 15 Vcc; open loop gain 120 dB; low offset voltage maximum 200 μ V and the bias current: maximum 5 pA.

4. NO₂ gas sensor made with rGO-doped CeO₂ and CeO₂-doped rGO/ZnO

4.1. Synthesis of sensitive materials rGO-doped CeO₂ and CeO₂/rGO-doped ZnO

In order to study the CeO₂ sensor properties for NO₂ detection, two sets of sensitive materials for sensors was synthesized: (a) 1%rGO/CeO₂ nanocomposite as sensitive material to study the effect of rGO adding on the sensitivity and (b) 1%(wt. %)CeO₂ was added at 1%(wt.%) rGO/ZnO-nanocomposite, in order to study the effect of CeO₂ adding on the sensitivity.

- A. Synthesis of 1%rGO/CeO₂: 1%(wt.%) rGO/CeO₂ nanocomposite was synthesized in situ by precipitation method using Ce(NO₃)₃ and NH₃ (25% conc) at 90°C and 30 min maturation time.
- B. Synthesis of 1%CeO₂/1%rGO/ZnO: The 1%(wt.%)GO and 1%CeO₂ was mixed with ZnO in ethanol. The resulted powder after ethanol evaporation was heat treated at 150°C. The GO was synthesized by Hummers' modified method using as strong oxidant potassium permanganate (mass ratio C:oxidant = 1:3) in a solution of sodium nitrate and concentrated sulfuric acid (1 g/150 ml) and graphite [45, 46].

4.2. Structural and morphological characterizations of the sensitive materials

UV-Vis diffuse reflectance spectroscopy measurements were performed a Jasco V-570 Spectrophotometer, Japan, equipped with integrating sphere for diffuse reflectance measurement mode and SPECTRALON reference as etalon, and bang gap software in order to evaluate the optical properties and band gap values of the CeO₂, doped CeO₂ with 1%rGO and doped 1%GO-ZnO nanocomposite with 1%CeO₂. The diffuse reflectance spectrum was converted in absorbance spectrum and presented in **Figure 17**. The band gap was calculated using Kubelka-Munk equation with associated plot $\sqrt{\alpha h\nu}$ versus photon energy E_g [eV], where α is extinction coefficient [cm^{-1}] and h is Planck constant 4.135×10^{-15} [eVs], ν is light frequency [s^{-1}] and wavelength [nm] [47–49]. The linearity coefficient was in all case bigger than 0.99.

In **Table 3**, the UV-Vis spectra parameters of UV-Vis measurements, for 1%rGO/CeO₂ and CeO₂ is also presented.

Legend: A_{abs} represents absorbance plasmon resonance (APR) and I represents intensity of APR.

The effect of doping of CeO₂ with 1%rGO leads to blue shift of APR presented in **Table 3** and **Figure 17** accompanied by the hyperchromic effect for both peaks, while the band gap are narrows, keeping the same characteristic shape of the ceria spectrum. The same effect—a blue shift has been described in literature for both TiO₂ aditived with GO and for ZnO aditived with

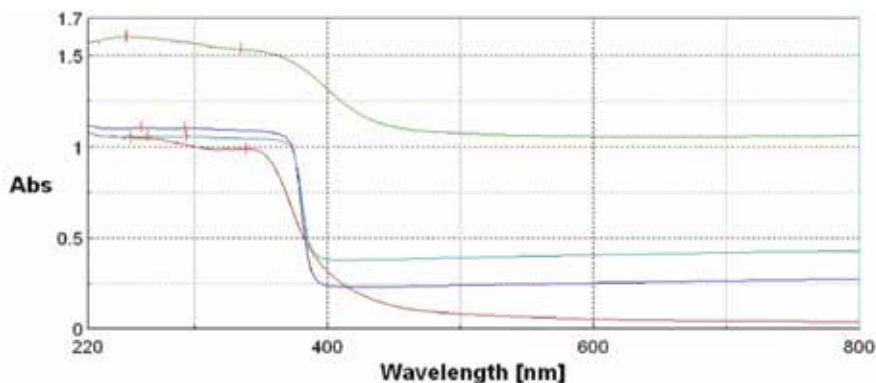


Figure 17. Diffuse reflectance UV-Vis spectroscopy spectra for CeO₂ (red), (1%CeO₂/1%rGO) ZnO (blue), 1%rGO/ZnO (cyan) and 1%rGO/CeO₂ (green).

Samples	Abs _{max1}	I1	Abs _{max2}	I2	Band gap, [eV]
1%rGO/CeO ₂	249	1.065	335	1.535	3.05
	Blue shift	Hyper chromic effect	Blue shift	Hyper chromic effect	band gap narrowing
CeO ₂ -standard	252	1.051	339	0.99	theoretical Commercial type
					3.19, Ref. [47] 3.16

Table 3. UV-Vis spectra parameters of UV-Vis measurements.

GO [50, 51]. The introduction of 1%GO(wt.%) in CeO₂ leads to a decrease in the effective optical band gap value from 3.16 eV to 3.05 eV, with a variation of 0.11 eV. This shows that the 1%GO(wt.%) acted as a band gap modifier [47–49, 52]. The same effect has been described in literature for the introduction of GO and related materials rGO in TiO₂ leads to a decrease in band gap [50]. Earlier, a lot of researchers attempt to tailor the properties of oxide semiconductors by using band gap modifiers and in this way to improve the catalytic, photovoltaic and sensing properties; this new trend is named bend gap engineering [47–49, 52]. Many researchers obtained a band gap narrowing after heat treatment of CeO₂ [52] and doping with different metals as Co [52], Gd [53], functionalized by different techniques [47], etc. Rare earth oxides present a high basicity related to ordinary oxide semiconductors such as TiO₂, WO₃, SnO₂ and ZnO, fast oxygen ion mobility and interesting catalytic properties which are important in gas sensing application [54–56]. **Table 4** presents UV-Vis spectra parameters of UV-Vis measurements for 1%CeO₂/1%rGO/ZnO and 1%rGO/ZnO.

In the case of doping with 1%(wt.%)CeO₂ of the 1%(wt.%)rGO/ZnO nanocomposite, the effect is the same, an increasing of APR accompanied by the hyperchromic effect with the preservation of the characteristic spectra shape. But in opposite with the first case of CeO₂ doped with 1%GO(wt. %), there is a decrease in effective optical band gap value from 3.24 to 3.19 eV, with a variation of 0.05 eV. This shows that the 1%CeO₂(wt.%) acted as a band gap modifier. The UV-Vis spectra present a strong absorption bands below 400 nm in UV region for the nanocomposites with the main component ZnO which are attributed to ZnO NP. The APR of ZnO nanocomposites are

Samples	Abs _{max1}	I1	Abs _{max2}	I2	Band gap, [eV]
1%CeO ₂ /1%rGO-ZnO	260	1.104	293	1.103	3.19
	Blue shift	Hyper chromic effect	Blue shift	Hyper chromic effect	Band gap narrowing
1%rGO-ZnO-etalon	265	1.059	294	1.056	3.25
ZnO	376	—	—	—	Theoretic
	Ref. [60]				3.37
					Ref.: [48], [57–60]

Legend: A_{abs} represents absorbance plasmon resonance (APR) and I represents intensity of APR.

Table 4. UV-Vis spectra parameters of UV-Vis measurements for 1% CeO₂/1%rGO/ZnO and 1%rGO/ZnO.

lower, in generally, than the absorption band of bulk ZnO (373 nm) that had a wide direct band gap at room temperature of 3.37 eV [48, 57–60]. CeO₂ adding on ZnO nanocomposite surface leads to a significant increase of the absorption in the UV light spectrum and decrease in the visible light spectrum. Based on the above results, UV-Vis and transformed Kubelka–Munk function plots suggested that are necessary energy for generation of electrons in conduction bands and holes in valence bands is smaller for the doped 1%rGO/CeO₂ than the CeO₂, this makes the doped CeO₂ more reactive and sensitive. Other researchers tried to improve the sensing properties of ZnO sensor, for ethanol detection, by adding noble metals such as Pd [61], Pt [62] and Au [63], other metals such as Al, In, Cu, Fe and Sn [64], oxides as TiO₂ [65], CuO [66], CoO [67], RuO₂ [68] and SnO₂ and not in the end Ce and CeO₂ [55]. There is a current practice to use band gap modifiers. Many researchers use a band gap modifier in order to improve the functional properties of nanocomposite based on semiconductors oxides. The functional properties are ranging from the photocatalytic properties, sensitivity and selectivity for different sensor types, catalysts and others [52]. Raman spectroscopy measurements was performed with Raman dispersive spectrometry–LabRam HR Evolution, Horiba Jobin Yvone, France, equipped with Laser wave 532 nm, acquisition time 5 s, 10 accumulation, 0.1% laser power, used in order characterized the order-disorder degree in the synthesized nanocomposite. **Figure 18** shows the RAMAN spectra for CeO₂ and rGO/CeO₂.

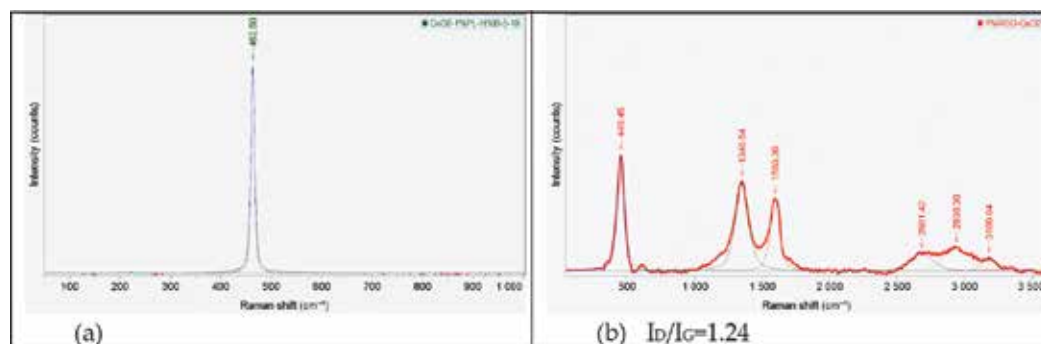


Figure 18. Raman spectra for CeO₂ powder (a) and synthesized 1%rGO/CeO₂ (b).

Figure 18(a) presents the Raman spectrum of CeO₂ powder which reveals a peak situated at 462.5 cm⁻¹ characteristic for CeO₂, corresponding to the Raman active modes F_{2g} for Ce–O symmetric breathing mode of oxygen atoms around the Ce atoms [49]. **Figure 18(b)** shows the Raman spectrum of 1%rGO/CeO₂ with characteristic peak of ceria at 449 cm⁻¹ corresponding to the Raman active modes of CeO₂ and characteristics graphene oxide peaks [69] at 1348.54 cm⁻¹ (D band), 1593.30 cm⁻¹ (G band), 2681.42 cm⁻¹ (2D band), 2938.30 cm⁻¹ (2D + D' band) and 3180.64 cm⁻¹ (G + D' band). According to the Raman line, broadening is equivalent with lattice constant cell crystallographic parameter a₀ of CeO₂ can be estimated by Eq. (9) [49], with 0.9 nm for CeO₂ powder and 0.43 nm for the CeO₂ from the 1% rGO-CeO₂ nanocomposite. The characteristic peak of CeO₂ was shifted with 13.05 cm⁻¹ at lower wave number as a doping effect of 1%rGO.

$$FW[cm^{-1}] = 10 + \frac{124,7}{d} [nm] \quad (9)$$

where the FW is full wide at half-maximum of the Raman active mode F_{2g} and d is the diameter particle in nm. **Figure 19(a)** shows the Raman spectrum of GO with characteristic peaks of graphene oxide peaks at 1347.96 cm⁻¹ (D band), 1595.33 cm⁻¹ (G band), 2681.77 cm⁻¹ (2D band), 2914.68 cm⁻¹ (2D + D' band) and 3196.75 cm⁻¹ (G + D' band). **Figure 19(b)** shows the Raman spectrum of 1%CeO₂/1%rGO/ZnO with characteristic peaks of graphene oxide peaks at 1350.87 cm⁻¹ (D band), 1605.74 cm⁻¹ (G band), 2684.22 cm⁻¹ (2D band) and characteristic peaks of ZnO and active modes F_{2g}, CeO₂ (462.79 cm⁻¹), where the I_D/I_G can be used to evaluate quantitative the crystallinity/disorder degree and are varying between 1.05 and 1.24, lower value indicates the less defects in graphitic structure [69]. **Figure 20** shows the morphologies for the three sensitive materials reveals for (a) CeO₂ was evidenced a polycrystalline structure, for (b) CeO₂/rGO - the micrographic image presents a 3-D layered structured of GO mixed with small polycrystalline particles of ceria and for (c) CeO₂/rGO/ZnO was evidenced a mixed polycrystalline structure of preponderant small particles of wurtzite hexagonal types ZnO and minor faces of cubic CeO₂ and carbon faces.

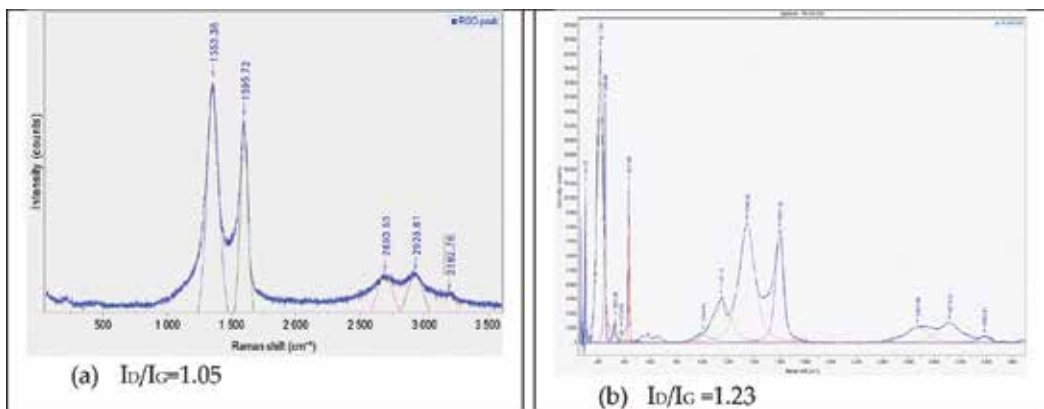


Figure 19. Raman spectra for rGO (a) and synthesized 1%CeO₂/1%rGO/ZnO (b).

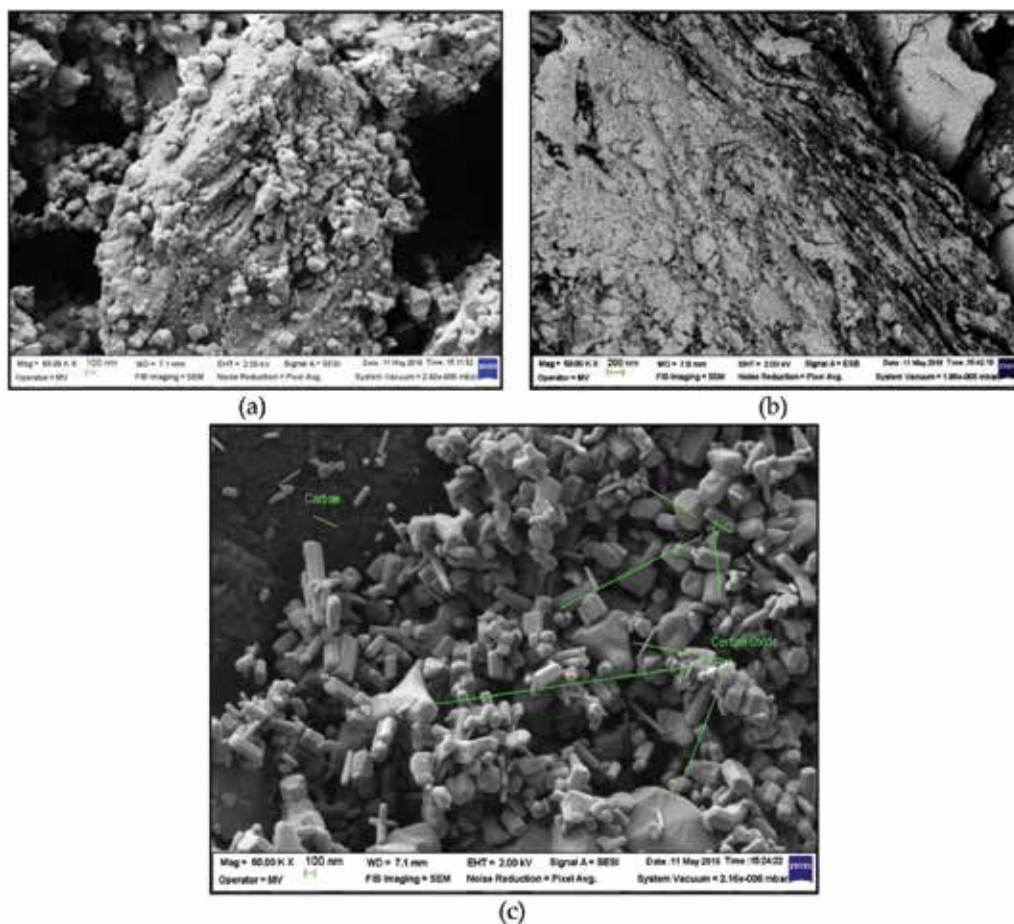


Figure 20. SEM images for: (a) CeO₂; (b) CeO₂/rGO; (c) CeO₂/rGO/ZnO.

4.3. The construction of the sensing element for NO₂ gas detection designed with rGO-doped CeO₂ and CeO₂-doped rGO/ZnO sensitive material

The sensor module is constituted from printed circuit board (PCB), substrate with interdigitated Ag array electrode deposited by photolithographic technology and the sensitive material in amounts 15–20 mg was deposited on surface electrode. The active area for sensitive material was 10 mm × 0.5 mm, **Figure 21(a)** and **(b)**.

4.4. The NO₂ gas sensing mechanism

In metal oxide semiconductor gas sensors, the resistance is measured as a function of the gas concentration. Generally, this devices function at elevated temperature between 200 and 600°C in air. The grain of metal oxide is covered by adsorbed oxygen molecules. Oxygen molecules present the character of electronegativity, they extract electrons from the conduction band of

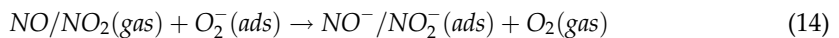
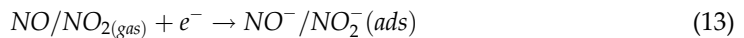


Figure 21. The NO₂ gas sensing element structure (a) PCB substrate with interdigitated Ag array electrode; (b) the sensing element made with PCB substrate and sensitive material deposited on surface electrode.

metal oxide causing the formation of oxygen ions O_2^- , O^- , O^{2-} , adsorbed at the surface of metal oxide. Since electrons are removed from the metal oxide, the concentration of free charge carriers is reduced forming a depletion layer at grain boundaries. The surface reactions can be written according with Eqs. (10–12):



As is it known, nitrogen oxides specify as NO_x have the character of oxidizing gases with very high electron affinity 2.28 eV as compared with oxygen 0.43 eV. The NO_x molecules interact with the surface of metal oxide through surface adsorbed oxygen ions, thus increasing the potential barrier at grain boundaries. The redox reactions taking place on the surface of a metal oxide can be written according with Eqs. (13–14) [70].



As result, the thickness and resistance of the depletion layer increase and resistance change is reversible at operating temperature [70]. The oxygen vacancies can significantly enhance the adsorption of oxygen molecules and electrons will transfer from the oxygen vacancies from CeO₂ to the oxygen molecules, resulting in more oxygen species (especially O²⁻). These oxygen species will react with NO₂, resulting in an abrupt change in the conductivity of the sensor [71]. The graphene sheets by their good properties as: high surface area 2630 m²/g, thermal conductivity in the range of 3000–5000 W/mK at room temperature carrier mobility up to 200,000 cm²/Vs [72], electrical conductivity of 7200 S/m [73], coming from their structure two-dimensional (2D) single atom layer is used in gas sensing and in the composite leads to increase of the electrical conductivity of CeO₂ and thus improve the performance to gas sensing room temperature [71].

4.5. The NO₂ gas sensors testing and sensing characteristics

The sensors with sensitive materials 1%rGO-doped CeO₂, and 1% CeO₂/1%rGO-doped ZnO were tested in NO₂ atmosphere in concentrations 5 and 10 ppm. The gas testing was effected

with testing installation presented in **Figure 4**. The gas testing was performed in order to establishment of the sensitivity sensors and response time. The sensor sensitivity was expressed in accord with Eq. (15), as the ratio of resistance in air to that in target gas, in this case NO_2 ,

$$S = \frac{Ra}{Rg} \tag{15}$$

where Ra is the resistance of sensor in air and Rg is the resistance of sensor in gas.

The response time is expressed by formula:

$$Ra - 90\%x(Ra - Rg) \tag{16}$$

Notations are the same with Eq. (15) [28]. Having the resistance values, from the graph, the response time can be determined. **Figure 22** shows the resistance variation with time exposure gas and **Figure 23** shows the sensitivity (response) for sensing element with time exposure gas for two sensitive material: 1%rGO/CeO₂ and 1%CeO₂/1%rGO/ZnO. All the characteristics are considered for the 1 hour time exposure. Since the resistance of sensors decreases sharply, for a good view we opted for a semilogarithmic scale representation of resistance and sensors response with exposure time. The decreases of resistance denotes a character of type p semi-conductors for both sensitive materials in oxidant gas like NO_2 , character given by reduced graphene oxide which is a semiconductor type p.

The sensors performances can be resumed in **Table 5**.

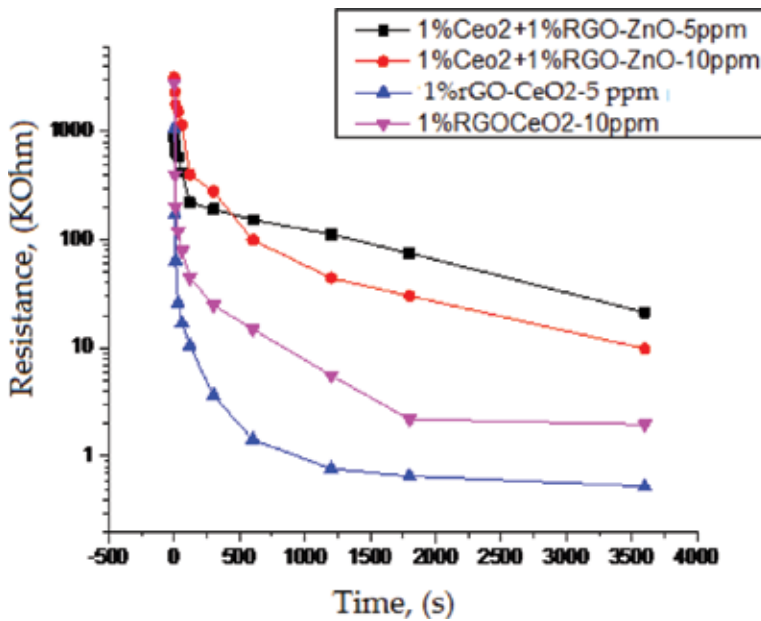


Figure 22. Resistance variation function with time.

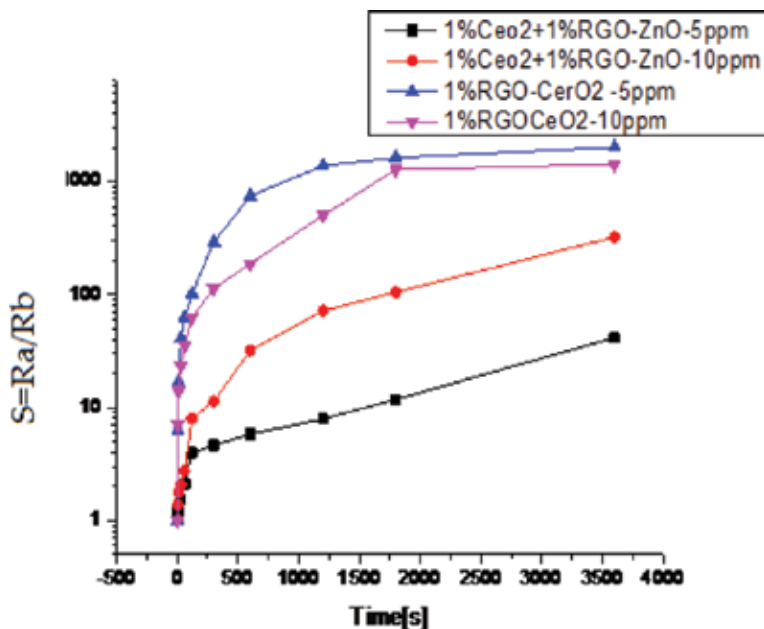


Figure 23. The sensitivity variation function with time.

Sensitive material	Concentration NO ₂ , [ppm]	Resistance in air, [kΩ]	Resistance in gas, [kΩ] (after 3600 s exposure)	Sensitivity, Ra/Rg	Response time, [s]
1%rGO/CeO ₂	5	1060	0.53	2000	2.5
1%CeO ₂ /1%rGO/ZnO	5	885	21.43	41.29	2.8
1%rGO/CeO ₂	10	2800	1.54	1818	3.5
1%CeO ₂ /1%rGO/ZnO	10	3180	9.9	321.2	2.2

Table 5. The characteristics of sensors with sensitive materials 1%rGO/CeO₂ and 1%CeO₂/1%rGO/ZnO.

Analyzing the obtained results, it can be concluded that the both sensitive materials show the good performance at NO₂ exposure at room temperature. However, the sensitive material composed by 1%rGO/CeO₂ presents very good sensitivity at NO₂ exposure for 5 and 10 ppm concentrations of 2000 and 1818 and very short response time of 2.5 and 3.5 s. Thus, sensitive materials with CeO₂ in majority concentration in matrix with reduced oxide graphene presents the best performance at NO₂ detection, face to sensitive materials 1%CeO₂/1%rGO/ZnO where ZnO is majority and are a promising sensitive materials for NO₂ detection.

4.6. Signal conditioning of the sensing element for NO₂ gas detection designed with rGO-doped CeO₂ and CeO₂-doped rGO/ZnO sensitive material

Resistance of sensor sensing element ES, $R + \Delta R$, Figure 24 may vary from less than 10 kΩ to several hundred kΩ, depending on the design of the sensor and the physical environment to

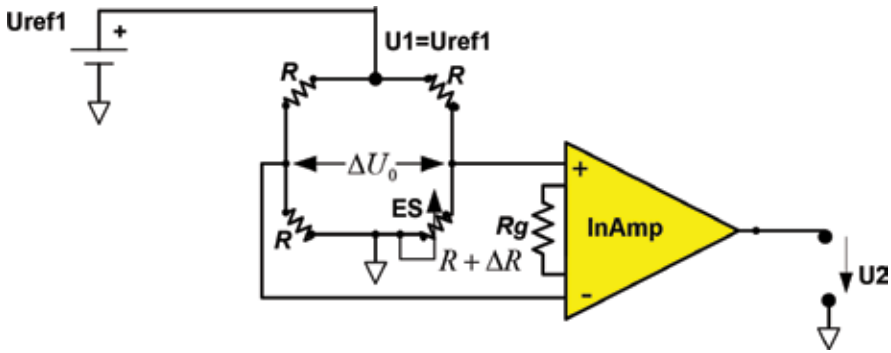


Figure 24. Schematic of the electronic block for signal conditioning generated by the sensing element.

be measured. The sensing element ES of the NO_2 gas sensor is disposed in one of the Wheatstone bridge arms and shows the resistance R for a NO_2 concentration of zero ppm. The resistances of resistors disposed in all of other branches of the bridge show the same value, namely R . A DC voltage excitation source U_1 is connected to one of the bridge diagonals [74].

If the gas concentration of NO_2 is zero ppm, the sensing element ES shows the resistance R . The Wheatstone bridge is in this case at equilibrium so that the voltage measured on the other diagonal of the bridge is 0 V. Variation of NO_2 gas concentration in the range from zero ppm to 10 ppm causes a voltage variation with ΔU_0 , which can be measured on the other diagonal of the bridge. The voltage variation up to ΔU_0 is given by the relation (17):

$$\Delta U_0 = \frac{U_1}{2} \left[\frac{\frac{\Delta R}{2}}{R + \frac{\Delta R}{2}} \right] \quad (17)$$

The operational amplifier that can be used with the best performance is instrumentation type amplifier (in-amp), “resistor programmable” (**Figure 24**). Considering the transfer function of the electronic amplifier module and taking into account the relation (17), we obtain [74]:

$$U_2 = \frac{U_1}{2} \left[\frac{\frac{\Delta R}{2}}{R + \frac{\Delta R}{2}} \right] A = K \left[\frac{\frac{\Delta R}{2}}{R + \frac{\Delta R}{2}} \right], \quad (18)$$

where A is the amplification factor, depending on the R_g resistance value and $K = \frac{U_1}{2} A$, is a constant. In-amps such as the AD620 family, the AD623 and AD627, Analog Devices type can be used in single (or dual) supply bridge applications.

4.6.1. Realization of the continuous U_1 excitation voltage source

The continuous U_1 excitation voltage source is made using a D/A digital/analog converter, a U_{ref} reference voltage and an operational amplifier (OA) (**Figure 25**). Thus, depending on the values set for the least significant bit (LSB) up to the most significant bit (MSB), the resulting word can establish a desired U_1 continuous excitation voltage. **Figure 25** shows the schematic of the electronic block for the U_1 excitation voltage source.

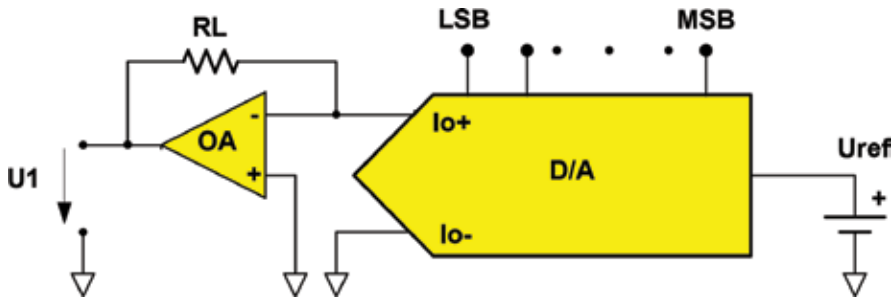


Figure 25. Schematic of the electronic block for the U1 excitation voltage source.

4.6.2. Bridge-linearization electronic circuit

Schematic of the electronic linearization block of the signal generated by the Wheatstone bridge, via an operational amplifier, in-amp uses an analog multiplier [75], AD 534 or AD 734, produced by analog devices (**Figure 26**). The transfer function associated with the AD 534 or AD 734 analog multiplier is written [76, 77]:

$$W = A_0 \left\{ \frac{(X1 - X2)(Y1 - Y2)}{SF} - (Z1 - Z2) \right\} \quad (19)$$

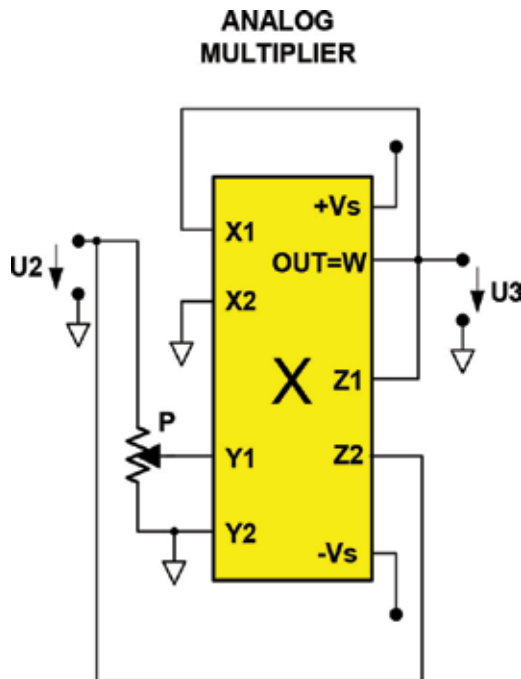


Figure 26. Schematic of the electronic linearization block of the signal generated by the Wheatstone bridge, via an operational in-amp instrumentation amplifier.

where A_0 is the open loop gain, $X1, X2, Y1, Y2, Z1$ and $Z2$ represent the inputs of the analog multiplier, SF a scale factor, typically $SF = 10$ V and $W = OUT$, according to **Figure 26**.

Since $A_0 \rightarrow 72$ dB can be considered as $W/A_0 \rightarrow 0$ and the relation (19) becomes:

$$(X1 - X2)(Y1 - Y2) = SF(Z1 - Z2) \tag{20}$$

Since $Z1 = W$ it is obtained:

$$W = \frac{(X1 - X2)(Y1 - Y2)}{SF} + Z2 \tag{21}$$

Since $Z2 = U2, Y1-Y2 = \beta U2, 0 \leq \beta < 1, X2 = 0$ and $X1 = Z1 = W=U3$, according to **Figure 26**. Finally,

$$U3 = W = \frac{U2}{1 - \frac{\beta U2}{SF}} \tag{22}$$

is obtained

The relation (6) together with the relation (2) represents the calculation method regarding the linearization of the signal generated by the Wheatstone bridge, via an operational in-amp instrumentation amplifier.

4.6.3. Resulting structures for the electronic block for signal conditioning generated by the sensing element

By considering the three previously analyzed electronic blocks, the electronic block for signal conditioning generated by the sensing element is obtained. **Figure 27** shows the schematic of

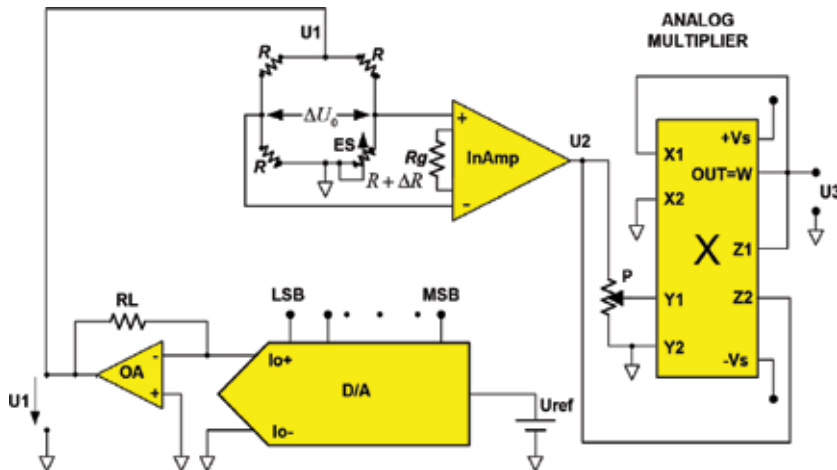


Figure 27. Schematic of the electronic block for signal conditioning generated by the sensing element, single supply bridge applications.

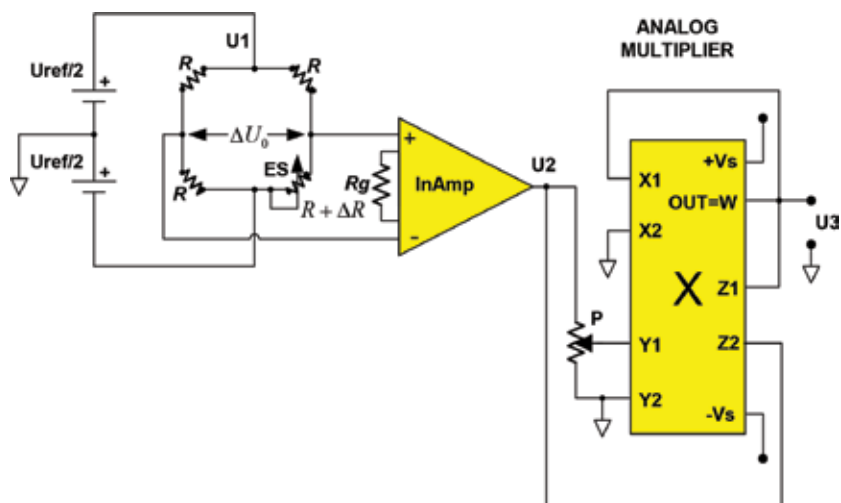


Figure 28. Schematic of the electronic block for signal conditioning generated by the sensing element, dual supply bridge applications.

the electronic block for signal conditioning generated by the sensing element, single supply bridge applications.

It is possible to reconfigure circuits so as to improve the performance in terms of reduces the dc common-mode voltage to zero. **Figure 28** shows how the use of split U1 tension in order to reduce the dc common-mode voltage to zero.

An isolation amplifier can be useful for this application, with respect to the signal-conditioning, so that it does not exist galvanic connections between the bridge and grounded instrumentation circuitry.

5. Conclusions

Cerium, by its unique electronic configuration ($[Xe] 4f^2 6s^2$) and by the two common valence states Ce^{3+} and Ce^{4+} allowing a redox reaction between them which gives CeO₂ excellent chemical and physical properties, is used in many applications, like as: three-way catalytic reactions to eliminate toxic automobile exhaust, the low-temperature water gas shift reaction, oxygen permeation membrane systems for fuel cells as well as gas sensors. For gas sensing applications, several sensitive elements based on CeO₂ were tested to determine both this detection function as well as this performances:

- By doping the CeO₂ with oxides semiconductor, for example, Nb₂O₅ introduced in CeO₂ structure, the following mechanism is triggered: Nb⁵⁺ ions initiate the reduction of Ce⁴⁺ to Ce³⁺ resulting in the formation of oxygen vacancies with consequences in increasing the sensitivity.
- The ionic conductivity of CeO₂ is improved by doping with rare earth oxides such as Sm₂O₃, Gd₂O₃ and Y₂O₃. The size of conductivity for doped ceria depends on the ionic

radius of the doping ion. Therefore, the introduction of trivalent ions in ceria leads to the production of anion vacancies which may enhance catalytic and gas sensing.

- CO₂ detection using sensitive material based on mixed binary oxide CeO₂-Nb₂O₅ in ratio 97%/3%, for 10,000 ppm CO₂ at the 25, 50 and 70°C chamber test temperature, the sensor was developed voltage values of 48, 50 and 770 mV.
- CO₂ detection with Y₂O₃-doped CeO₂ molar ratio CeO₂/Y₂O₃ = 4:1 with characteristics: the CO₂ concentration in the range of 0–5000 ppm, function temperature 135°C, climatic conditions $T = 20^{\circ}\text{C}$, 40% RH and 80% RH, voltage values 378.17–377.32 mV for $T = 20^{\circ}\text{C}$, 40% RH and 377.11–376.61 for $T = 20^{\circ}\text{C}$, 80% RH. Sensitivity is 0.3 V/ppm and response time 30 seconds;
- Sensitive materials based on 1%rGO/CeO₂ and 1%CeO₂/1%rGO/ZnO was analyzed with UV-Vis spectroscopy showing that a decreasing of band gap of CeO₂ in matrix with rGO from 3.19 eV at 3.05 eV what allows for sensor to function at room temperature. The sensors were tested for 5 and 10 ppm NO₂ obtaining the sensitivities of 2000 and 1818, response times of 2.5 and 3.5 s for sensitive material 1%rGO/CeO₂ and sensitivities of 41.29 and 321.2, response times of 2.8 and 2.2 s for sensitive material 1%CeO₂/rGO/ZnO. The sensitive materials made so that the matrix in which CeO₂ is in majority presents the best performance.
- Also, the sensing mechanism in CO₂ and NO₂ detection was discussed.

Based on these results, it can be stated that CeO₂ is a good candidate in gas sensors applications.

Acknowledgements

The research was performed with the support of Ministry of Research and Innovation, NUCLEU Programme Research Projects - Romania, Contract PN18240301/2018, "Sensors and electronic actuators based on new active materials", and UEFISCDI, Program 2 - Romania, Contract 4SOL/2017, "Development and implementation of modern solutions for gas turbine propulsion systems and their associated systems".

Conflict of interest

No conflict of interest exists with regard to this chapter.

Author details

Lucian Pîslaru-Dănescu*, Gabriela Telipan, Ioana Ion and Virgil Marinescu

*Address all correspondence to: lucian.pislaru@icpe-ca.ro

National Institute for Research and Development in Electrical Engineering ICPE-CA, Bucharest, Romania

References

- [1] Song S, Wang X, Zhang H. CeO₂-encapsulated noble metal nanocatalysts: Enhanced activity and stability for catalytic application-review. *NPG Asia Materials*. 2015;**7**:e179. DOI: 10.1038/am.2015.27
- [2] Babitha KK, Sreedevi A, Priyanka KP, Sabu B, Vargheze T. Structural characterization and optic studies of CeO₂ nanoparticles synthesized by chemical precipitation. *Indian Journal of Pure & Applied Physics*. 2015;**53**:596-603
- [3] Melchionna M, Fornasiero P. The role of ceria-based nanostructured materials in energy applications. *Materials Today*. 2014;**17**(7):349-357. DOI: 10.1016/j.mattod.2014.05.005
- [4] Hadi A, Yaacob II. Synthesis of PdO/CeO₂ mixed oxides catalyst for automotive exhaust emissions control. *Catalysis Today*. 2004;**96**(3):165-170. DOI: 10.1016/j.cattod.2004.06.118
- [5] Andreeva D, Idakiev V, Tabakova T, Ilieva L, Falaras P, Bourlinos A, et al. Low-temperature water-gas shift reaction over Au/CeO₂ catalysts. *Catalysis Today*. 2002;**72**(1-2):51-57. DOI: 10.1016/S0920-5861(01)00477-1
- [6] Kharton V, Figueiredo FM, Navarro L, Naumovich EN, Kovalevsky AV, Yaremchenko AA, et al. Ceria-based materials for solid oxide fuel cells. *Journal of Materials Science*. 2001;**36**:1105-1117. DOI: 10.1023/A:1004817506146
- [7] Ansari SA, Khan MM, Ansari MO, Lee SKJ, Cho MH. Band gap engineering of CeO₂ nanostructure using an electrochemically active biofilm for visible light applications. *RSC Advances*. 2014;**4**:16782-16791. DOI: 10.1039/c4ra00861h
- [8] Prabaharana DMDM, Sadaiyandib K, Mahendran M, Sagadevand S. Structural, optical, morphological and dielectric properties of cerium oxide nanoparticles. *Materials Research*. 2016;**19**(2):478-482. DOI: 10.1590/1980-5373-MR-2015-0698
- [9] Shi H, Hussain T, Ahuja R, Kang TW, Luo W. Role of vacancies, light elements and rare-earth metals doping in CeO₂. *Scientific Reports*. 2016;**6**:31345. DOI: 10.1038/srep31345
- [10] Alla SK, Kollu P, Singh Meena S, Poswal HK, Prajapat CL, Mandal RK, et al. Investigation of magnetic properties for Hf⁴⁺ substituted CeO₂ nanoparticles for spintronic applications. *Journal of Materials Science: Materials in Electronics*. 2018;**29**(12):10614-10623. DOI: 10.1007/s10854-018-9125-x
- [11] Kumar E, Selvarajan P, Muthura D. Synthesis and characterization of CeO₂ nanocrystals by solvothermal route. *Materials Research*. 2013;**16**(2):269-276. DOI: 10.1590/S1516-14392013005000021
- [12] Sun C, Li H, Zhang H, Wang Z, Chen L. Controlled synthesis of CeO₂ nanorods by a solvothermal method. *Nanotechnology*. 2005;**16**:1454-1463. DOI: 0957-4484/05/091454
- [13] Laberty-Robert C, Long JW, Lucas EM, Pettigrew KA, Stroud RM, Doescher MS, et al. Sol-gel-derived ceria nanoarchitectures: Synthesis, characterization, and electrical properties. *Chemistry of Materials*. 2006;**18**(1):50-58. DOI: 10.1021/cm051385t

- [14] Yang H, Zhang K, Shi R, Tang A. Sol–gel synthesis and photocatalytic activity of CeO₂/TiO₂ nanocomposite. *Journal of American Ceramic Society*. 2007;**90**(5):1370-1374. DOI: 10.1111/j.1551-2916.2007.01540.x
- [15] Shah N, Bhangaonkar K, Pinjari DV, Mhaske ST. Ultrasound and conventional synthesis of CeO₂/ZnO Nanocomposites and their application in the photocatalytic degradation of Rhodamine B dye. *Journal of Advances in Nanomaterials*. 2017;**2**(3):133-145. DOI: 10.22606/jan.2017.23001
- [16] Liu K, Zhong M. Synthesis of monodispersed nanosized CeO₂ by hydrolysis of the cerium complex precursor. *Journal of Rare Earth*. October 2010;**28**(5):680-683. DOI: 10.1016/S1002-0721(09)60178-2
- [17] Jayakumar G, Albert Irudayaraj A, Dhayal Ra A. Particle size effect on the properties of cerium oxide (CeO₂) nanoparticles synthesized by hydrothermal method. *Mechanics Materials Science & Engineering*. 2017;**9**(1):127-131. DOI: 10.2412/mmse.3.4.481.openaccessww.mmse.xyz
- [18] Zhou YC, Rahaman MN. Hydrothermal synthesis and sintering of ultrafine CeO₂ powders. *Journal of Materials Research*. 1993;**8**(7):1680-1686. DOI: 10.1557/JMR.1993.1680
- [19] Mazaheri M, Hassanzadeh-Tabrizi SA, Aminzare M, Sadrnezhad SK. Synthesis of CeO₂ nanocrystalline powder by precipitation method. *Materiały Ceramiczne/Ceramic Materials*. 2010;**62**(4):529-532, www.ptcer.pl/mccm
- [20] Sathyamurthy S, Leonard KJ, Dabestani RT, Parans Paranthaman M. Reverse micellar synthesis of cerium oxide nanoparticles. *Nanotechnology*. 2005;**16**(9):1960-1964. DOI: 10.1088/0957-4484/16/9/089
- [21] Schubert D, Dargusch R, Raitano J, Chan S-W. Cerium and yttrium oxide nanoparticles are neuroprotective. *Biochemical and Biophysical Research Communications*. 2006;**342**: 86-91, www.elsevier.com/locate/ybbrc
- [22] Zhou Y. Nanostructured cerium oxide based catalysts: Synthesis, physical properties and catalytic performance. A Dissertations, and Theses. Chemistry Department, University of Nebraska-Lincoln Digital Commons University of Nebraska–Lincoln, Summer 8 2015. <http://digitalcommons.unl.edu/chemistrydiss/61>
- [23] Berutti FA, Alves AK, Bergmann CP, Clemens FJ, Graule T. Synthesis of CeO₂ and Y₂O₃-doped CeO₂ composite fibers by electrospinning. *Particulate Science and Technology*. 2009;**27**:203-209. DOI: 10.1080/02726350902921681
- [24] Li M, Ren W, Wu R, Zhang M. CeO₂ enhanced ethanol sensing performance in a CdS gas sensor. *Sensors*. 2017;**17**:1577. DOI: 10.3390/s17071577
- [25] Gotte A, Spångberg D, Hermansson K, Baudin M. Molecular dynamics study of oxygen self-diffusion in reduced CeO₂. *Solid State Ionics*. 2007;**178**:1421-1427. DOI: 10.1016/j.ssi.2007.08.003
- [26] Zhao S, Gorte RJ. The effect of oxide dopants in ceria on n-butane oxidation. In: Department of Chemical & Biomolecular Engineering Departmental Papers (CBE). University of

- Pennsylvania; 2003. Published in *Applied Catalysis A: General*. 8 August 2003;**248**(1-2): 9-18. Publisher URL: [http://dx.doi.org/10.1016/S0926-860X\(03\)00102-9](http://dx.doi.org/10.1016/S0926-860X(03)00102-9)
- [27] Durrani SMA, Al-Kuhaili MF, Bakhtiari IA, Haider MB. Investigation of the carbon monoxide gas sensing characteristics of tin oxide mixed cerium oxide thin films. *Sensors*. 2012; **12**:2598-2609. DOI: 10.3390/s120302598
- [28] Xu Q-H, Xu D-M, Guan M-Y, Guo Y, Qi Q, Li G-D. ZnO/Al₂O₃/CeO₂ composite with enhanced gas sensing performance. *Sensors and Actuators B*. 2013;**177**:1134-1141. DOI: 10.1016/j.snb.2012.12.029
- [29] Neri G, Bonavita A, Rizzo G, Galvagno S, Capone S, Siciliano P. Methanol gas-sensing properties of CeO₂-Fe₂O₃ thin films. *Sensors and Actuators B*. 2006;**114**:687-695. DOI: 10.1016/j.snb.2005.06.062
- [30] Pandeewari R, Jeyaprakash BG. CeO₂ thin film as a low-temperature formaldehyde sensor in mixed vapour environment. *Bulletin of Materials Science*. October 2014;**37**(6): 1293-1299. DOI: 10.1007/s12034-014-0074-6
- [31] Pedhekar RB, Raghuwanshi FC. CeO₂ activated ZnO-TiO₂ thick film for CO₂ gas sensor. *International Journal of Engineering Science Invention*. 2017;**6**(8):20-28. www.ijesi.org
- [32] Abdollahzadeh Ghom S, Andreu T, Zamani C, Morante JR. Mesoporous ceria-zirconia solid solutions as oxygen gas sensing material using high temperature hot plates. In: *Proceedings Conference: Semiconductor Conference (CAS)*, Sinaia, Romania, October 15-17, 2012. 2012;**2**:277-280. DOI: 10.1109/SMICND.2012.6400786
- [33] Analog Devices, 30 V, high speed, low noise, low bias current. JFET Operational Amplifier ADA4627-1/ADA4637-1, Data Sheet; 2012
- [34] Sheingold D, editor. *Transducer Interfacing Handbook*. Analog Devices, Incorporated; 1980. Norwood, Massachusetts, U.S.A: Published by Analog Devices, Inc. ISBN 0-916550
- [35] de Oliveira Jardim E, Rico-Francés S, Abdelouahab-Reddam Z, Coloma F, Silvestre-Albero J, Sepúlveda-Escribano A, et al. High performance of Cu/CeO₂-Nb₂O₅ catalysts for preferential CO oxidation and total combustion of toluene. *Applied Catalysis A: General*. 2015;**502**:129-137. DOI: 10.1016/j.apcata.2015.05.033
- [36] Norby T. A Kröger-Vink compatible notation for defects in inherently defective sublattices. *Journal of the Korean Ceramic Society*. 2010;**47**(1):19-25. DOI: 10.4191/KCERS.2010.47.1.019
- [37] Leung E. Mechanistic investigation of novel niobium-based materials as enhanced oxygen storage components and innovative CO oxidation catalyst support for environmental emission control systems [PhD thesis]. Columbia University: Columbia/Academic Commons; 2016. <https://doi.org/10.7916/D8N016FM>
- [38] Raba AM, Bautista-Ruíz J, Joya MR. Synthesis and structural properties of niobium pentoxide powders: A comparative study of the growth process. *Materials Research*. 2016; **19**(6):1381-1387. DOI: 10.1590/1980-5373-MR-2015-0733

- [39] Pîslaru-Dănescu L, Telipan G. Sensing element for CO₂ detector based on CeO₂-Nb₂O₅ mixed semiconductor oxides with interfacing electronic circuit for signal conditioning. In: Proceedings IEEE Sensor Applications, SAS. IEEE; February 23–25, 2010, Limerick, Ireland. Catalog Number: ISBN: CFP10SAS-PRT
- [40] Yen-Pei F. Ionic conductivity and mechanical properties of Y₂O₃-doped CeO₂ ceramics synthesis by microwave-induced combustion. *Ceramics International*. 2009;**35**:653-659. DOI: 10.1016/j.ceramint.2008.01.027
- [41] Yamashita K, Ramanujachary KV, Greenblatt M. Hydrothermal synthesis and low temperature conduction properties of substituted ceria ceramics. *Solid State Ionics*. 1995;**81**(1-2): 53-60. DOI: 10.1016/0167-2738(95)99031-H
- [42] Goto Y, Takahashi K, Omata T, Otsuka-YaoMatsuo S. Synthesis of Y₂O₃-doped CeO₂ nanocrystals and their surface modification. *Journal of Physics: Conference Series*. 2009; **165**:012041. DOI: 10.1088/1742-6596/165/1/012041
- [43] Yue HM, Liu ZL, Wang Y, Yao KL. Electrical properties of nanocrystalline CeO₂-Y₂O₃ thin films prepared by the sol-gel method. *Inorganic Materials*. 2003;**39**(7):720-772. DOI: 0020-1685/03/3907
- [44] Gabriela T, Lucian P-D, Virgil M, Ionela PP, Dragos O. Preparation and characterization of CeO₂-Y₂O₃ binary-oxides and their CO₂ gas-sensing properties. *Sensor Letters*. February 2016;**14**(2):114-121(8). DOI: 10.1166/sl.2016.3604
- [45] Hummers William S, Offeman RE. Preparation of graphitic oxide. *Journal of the American Chemical Society*. March 1958;**80**(6):1339. DOI: 10.1021/ja01539a017
- [46] Mogaldea G, Ion I, Sandu O, Stamatini I, Dumitru BA, Mogaldea M. Structural investigation of the graphite oxide and thermal reduced graphite oxide with terahertz spectroscopy. *Optoelectronics and Advanced Materials–Rapid Communications*. September 2011; **5**(9):973-976
- [47] Ansari SA, Khan MM, Ansari MO, Kalathil S, Leea J, Cho MH. Band gap engineering of CeO₂ nanostructure using an electrochemically active biofilm for visible light applications. *RSC Advances*. 2014;**4**:16782-16791. DOI: 10.1039/c4ra00861h
- [48] Talam S, Karumuri SR, Gunnam N. Synthesis, characterization, and spectroscopic properties of ZnO nanoparticles. *International Scholarly Research Network ISRN Nanotechnology*. 2012;**6**(372505):1-6. DOI: 10.5402/2012/372505
- [49] Goharshadi EK, Samiee S, Nancarrow P. Fabrication of cerium oxide nanoparticles: Characterization and optical properties. *Journal of Colloid and Interface Science*. 2011;**356**: 473-480. DOI: 10.1016/j.jcis.2011.01.063
- [50] Tan LL, Ong WJ, Chai SP, Mohamed AR. Reduced graphene oxide-TiO₂ nanocomposite as a promising visible-light-active photocatalyst for the conversion of carbon dioxide. *Nano-scale Research Letters*. 2013;**8**(1):465. DOI: 10.1186/1556-276X-8-465
- [51] Tongguang X, Zhang L, Cheng H, Zhu Y. Significantly enhanced photocatalytic performance of ZnO via graphene hybridization and the mechanism study. *Applied Catalysis B: Environmental*. January 2011;**101**(3-4):382-387. DOI: 10.1016/j.apcatb.2010.10.007

- [52] Wu Chen TS, Weng SC, Lin CN, Lai CH, Huang YJ, Jeng HT, et al. Dramatic band gap reduction incurred by dopant coordination rearrangement in Co-doped nanocrystals of CeO₂. *Scientific Reports*. 2017;**7**:4715. DOI: 10.1038/s41598-017-05046-0
- [53] Ruiz-Trejo E. The optical band gap of Gd-doped CeO₂ thin films as function of temperature and composition. *Journal of Physics and Chemistry of Solids*. 2013;**74**(4):605-610. DOI: 10.1016/j.jpcs.2012.12.014
- [54] Tsang C, Bulpitt C. Rare earth oxide sensors for ethanol analysis. *Sensors and Actuators B*. 1998;**52**(3):226-235. DOI: 10.1016/S0925-4005(98)00233-0
- [55] El-Sayed AM, Ismail FM, Khder MH, Yakout SM. Effect of ceo₂ doping on the structure, electrical conductivity and ethanol gas sensing properties of nanocrystalline zno sensors. *International Journal on Smart Sensing and Intelligent Systems*. September 2012;**5**(3). DOI: 10.21307/ijssis-2017-498
- [56] Yakout SM. Highly sensing properties sensors based on CeDoped ZnO and SnO₂ nanoparticles to ethanol gas. *IBIMA Publishing Journal of Research in Nanotechnology*. 2016; **2016**:14. <http://www.ibimapublishing.com/journals/NANO/nano.html> Article ID 690025. DOI: 10.5171/2016.690025
- [57] Lungu MV, Vasile E, Lucaci M, Pătroi D, Mihăilescu N, Grigore F, et al. Investigation of optical, structural, morphological and antimicrobial properties of carboxymethyl cellulose capped Ag-ZnO nanocomposites prepared by chemical and mechanical methods. *Materials Characterization*, ISSN 1044-5803. October 2016;**120**:69-81. DOI: 10.1016/j.matchar.2016.08.022
- [58] Lungu M, Gavrilu S, Enescu E, Ion I, Bratulescu A, Marutescu GML, et al. Silver–titanium dioxide nanocomposites as effective antimicrobial and antibiofilm agents. *Journal of Nanoparticle Research*. 2014;**16**:2203. DOI: 10.1007/s11051-013-2203-3
- [59] Li B, Liu T, Wang Y, Wang Z. ZnO/graphene-oxide nanocomposite with remarkably enhanced visible-light-driven photocatalytic performance. *Journal of Colloid and Interface Science*. 2012;**377**:114-121. DOI: 10.1016/j.jcis.2012.03.060
- [60] Debanath MK, Karmakar S. Study of blue shift of optical band gap in zinc oxide (ZnO) nanoparticles prepared by low-temperature wet chemical method. *Materials Letters*. 2013; **111**:116-119. DOI: 10.1016/j.matlet.2013.08.069
- [61] Liewhiran C, Phanichphant S. Effects of palladium loading on the response of a thick film flame-made ZnO gas sensor for detection of ethanol vapor. *Sensors*. 2007;**7**(7):1159-1184. DOI: 10.3390/s7071159
- [62] Hongsith N, Choopun S. Effect of platinum impregnation on ZnO tetrapods for ethanol sensor. *Advanced Materials Research*. 2008;**55**(57):289-292. DOI: 10.4028/www.scientific.net/AMR.55-57.289
- [63] Wongrat E, Pimpang P, Choopun S. Comparative study of ethanol sensor based on gold nanoparticles: ZnO nanostructure and gold: ZnO nanostructure. *Applied Surface Science*. 2009;**256**(4):968-971. DOI: 10.1016/j.apsusc.2009.02.046

- [64] Paraguay FD, Miki-Yoshida M, Morales J, Solis J, Estrada WL. Influence of Al, In, Cu, Fe and Sn dopants on the response of thin film ZnO gas sensor to ethanol vapour. *Thin Solid Films*. 2000;**373**(1-2):137-140. DOI: 10.1016/S0040-6090(00)01120-2
- [65] Zheng K, Gu L, Sun D, Mo X, Chen G. The properties of ethanol gas sensor based on Ti doped ZnO nanotetrapods. *Materials Science and Engineering B*. 2010;**166**(1):104-107. DOI: 10.1016/j.mseb.2009.09.029
- [66] Peng L, Xie T-F, Yang M, Wang P, Xu D, Pang S, et al. Light induced enhancing gas sensitivity of copper-doped zinc oxide at room temperature. *Sensors and Actuators B*. 2008;**131**(2):660-664. DOI: 10.1016/j.snb.2007.12.060
- [67] Li Y-J, Li K-M, Wang C-Y, Kuo C-I, Chen L-J. Low-temperature electrodeposited Co-doped ZnO nanorods with enhanced ethanol and CO sensing properties. *Sensors and Actuators B*. 2012;**161**(1):734-739. DOI: 10.1016/j.snb.2011.11.024
- [68] Navale SC, Ravi V, Mulla IS. Investigations on Ru doped ZnO: Strain calculations and gas sensing study. *Sensors and Actuators B*. 2009;**139**(2):466-470. DOI: 10.1016/j.snb.2009.03.068
- [69] Mohandoss M, Gupta SS, Nelleri A, Pradeep T, Maliyekkal SM. Solar mediated reduction of graphene oxide. *RSC Advances*. 2017;**7**:957-963. DOI: 10.1039/C6RA24696F
- [70] Afzal NC, Sabbatini L, Torsi L. NO_x sensors based on semiconducting metal oxide nanostructures. Progress and perspectives. *Sensors and Actuators B. Chemical*. 2012; **171-172**:25-42. DOI: 10.1016/j.snb.2012.05.026
- [71] Zhang L, Fang Q, Huang Y, Xu K, Ma F, Chu PK. Facet-engineered CeO₂/graphene composites for enhanced NO₂ gas-sensing. *Journal of Materials Chemistry C*. 2017;**5**: 6973-6981. DOI: 10.1039/C7TC01523B
- [72] Zhao F, Zhao Y, Chen N, Qu L. Stimuli-deformable graphene materials: From nanosheet to macroscopic assembly. *Materials Today*. 2016;**19**(3):146-156, <http://creativecommons.org/licenses/by-nc-nd/4.0/>. DOI: 10.1016/
- [73] Chammingkwan P, Matsushita K, Taniike T, Terano M. Enhancement in mechanical and electrical properties of polypropylene using graphene oxide grafted with end-functionalized polypropylene. *Materials*. 2016;**9**:240. DOI: 10.3390/ma9040240
- [74] Zumbahlen H, editor. *Basic Linear Design*. Analog Devices, Incorporated; 2007. Norwood, Massachusetts, U.S.A: Published by Analog Devices, Inc. ISBN 0-916550-28-1
- [75] Sheingold D, editor. *Multiplier Application Guide*. Analog Devices, Incorporated; 1978. Norwood, Massachusetts, U.S.A: Published by Analog Devices, Inc.
- [76] Kester W, editor. *Practical Design Techniques for Sensor Signal Conditioning*. Analog Devices; 1999. Norwood, Massachusetts, U.S.A: Published by Analog Devices, Inc. ISBN-0-916550-20-6
- [77] Sheingold D. *Nonlinear Circuits Handbook*. Analog Devices; 1976. Norwood, Massachusetts, U.S.A: Published by Analog Devices, Inc

Waterborne Acrylic/CeO₂ Nanocomposites for UV Blocking Clear Coats

Miren Aguirre, María Paulis and Jose R. Leiza

Additional information is available at the end of the chapter

<http://dx.doi.org/10.5772/intechopen.81332>

Abstract

The encapsulation of inorganic nanoparticles into polymer particles opens the door to countless applications taking advantage of the properties of both phases. In this chapter the UV absorbing capacity of CeO₂ nanoparticles and the film forming capacity of acrylic polymers are combined. A synthetic route to produce waterborne acrylic/CeO₂ hybrid nanocomposites for UV absorbing coatings applications is presented. This strategy leads to encapsulated morphology of the CeO₂ nanoparticles into the polymer particles and therefore to the lack of agglomeration during film formation. A mathematical model developed for inorganic/organic hybrid systems is able to explain the morphology evolution from the initial monomer droplet to the polymer particles. The films cast from these latexes are transparent and show excellent UV absorption that increases with the amount of cerium oxide nanoparticles in the hybrid latex. Finally, the photoactivity behavior that the CeO₂ nanoparticles may have on the polymeric matrix is studied, discarding additional effects on the acrylic polymer matrix.

Keywords: waterborne polymer dispersions, CeO₂ nanoparticles, hybrid nanocomposites, encapsulation, UV absorption

1. Introduction

The incorporation of metal oxide nanoparticles into polymer matrices opens the way to the production of novel nanocomposite materials due to the synergetic effect of each phase in the final properties, as well as the possibility to use them in many different applications. In this direction, in the last decade, many authors have studied the benefits in properties that could be obtained when combining CeO₂ nanoparticles with polymers. For instance, catalytic [1–3], thermal [4], mechanical [5, 6], optical [7–9], anticorrosion [10–12], and barrier properties [13]

of polymers have been considerably improved with the incorporation of CeO₂ nanoparticles. Moreover, CeO₂ nanocomposites can find application in many different fields such as chemi-sensors and photocatalyst for environmental applications [14–16], temperature and humidity sensors [17] or extractants for yttrium ions [18].

Taking advantage of the excellent UV absorption capacity of the CeO₂ nanoparticles, it is really interesting to incorporate these nanoparticles into polymer matrices in the field of outdoor clear coatings. Waterborne acrylic polymers, synthesized mainly by emulsion polymerization process, are widely used as protective coatings for different surfaces due to their low toxicity and good quality film forming properties [19]. However, the main drawback of these coatings is the photodegradation they suffer under UV light. Traditionally, organic UV absorbers and hindered amine light stabilizers (HALS) were used, but due to the increasing environmental pressure to reduce the volatile organic compounds (VOC) content in coatings, the use of metal oxides such as TiO₂ [20, 21], ZnO [22, 23] and CeO₂ [24, 25] have been considered as an attractive alternative. All of them absorb radiation around 400 nm [26] and possess a band gap energy of around 3 eV [27], which makes them good candidates for UV absorption purposes. There are some works in which TiO₂ [28–31] and ZnO [32–35] nanoparticles have been incorporated into polymer matrices to improve the UV absorbance capacity of the coating. Nevertheless, the photocatalytic activity of CeO₂ nanoparticles is lower than that of TiO₂ and ZnO [36], which might prevent a faster degradation of the acrylic coatings due to the presence of the metal oxide, making CeO₂ nanoparticles ideal candidates for their incorporation into waterborne acrylic coatings.

In waterborne hybrid coatings, the final morphology of the hybrid system is governed by the different nature of the inorganic nanoparticles and polymer. Therefore, the control of the morphology of the hybrid system is challenging. The compatibility between both phases (thermodynamics) as well as the polymerization process (kinetics) will define the final morphology of the nanocomposite and thus, the final application [37]. In the literature a variety of CeO₂ nanoparticles (hydrophilic or hydrophobically modified) have been incorporated following different polymerization processes.

For instance, Fischer [2] and Mari [3] synthesized CeO₂/polystyrene (PS) and CeO₂/polymethylmethacrylate (PMMA) hybrids with raspberry like morphology, following the same procedure. They synthesized PS and PMMA latexes incorporating active groups (acrylic, methacrylic or phosphate groups) on the surface of either the PS or PMMA polymer particles, synthesized previously by miniemulsion polymerization. These active groups served as nucleating agents for the crystallization of the CeO₂. As the CeO₂ nanoparticles were generated in the surface of the polymer particles, this morphology was very favorable to take advantage of the catalytic behavior of the CeO₂, giving for instance very efficient catalyst for the hydration reaction of 2-cyanopyridine to 2-picolinamide.

Another possibility to obtain pickering morphology is to use the inorganic nanoparticles to stabilize the polymer particles. CeO₂ nanoparticles were used as pickering stabilizers in the miniemulsion polymerization of acrylates by Zgheib et al. [38]. It was found that at least 35 wt% of CeO₂ nanoparticles were necessary to obtain stable hybrid latexes at intermediate solids content (25 wt%). Therefore, the large amount of nanoparticles used and the solids content obtained, limited their application as coating. However, using other inorganic nanoparticles,

such as SiO₂ or TiO₂, it has been possible to obtain high solids content latexes [39]. The ability of these hybrid nanocomposites with Pickering morphology as protective coatings [40, 41] has been successfully proved.

Hawsett was the first one adsorbing amphiphilic macro-RAFT agents on the surface of inorganic nanoparticles and starting the polymerization from the macro-RAFT agents to obtain encapsulation of the inorganic nanoparticles [42, 43]. Garnier [44, 45], Warrant [46] and Zgheib [47] followed this method to encapsulate CeO₂ nanoparticles. The hybrid acrylic/ CeO₂ latexes were obtained by semibatch emulsion polymerization starting the polymerization from the macro-RAFT agent modified CeO₂ nanoparticles. In general, good distribution of the CeO₂ nanoparticles in the polymer particles was obtained and the CeO₂ nanoparticles were located close to particle-aqueous phase interface and even encapsulated in some examples.

In this Chapter, a polymerization approach to produce waterborne hybrid (polymer/CeO₂) dispersions with encapsulated CeO₂ nanoparticles will be presented. The prediction of the evolution of the morphology during the polymerization will be illustrated by means of a mathematical model and finally the UV absorbing properties of the clear coatings produced from these hybrid latexes and the potential photochemical degradation of the coatings will be discussed.

2. Synthesis of acrylic/CeO₂ hybrid nanocomposites by seeded semibatch (mini)emulsion polymerization

In the production of waterborne binders (for coatings), emulsion polymerization is the most popular process. However, when it comes into hybrid waterborne binders, miniemulsion polymerization emerged as an alternative process, to overcome the limitations of emulsion polymerization when the inorganic material must be incorporated into the polymer particles [48–50]. Moreover, equilibrium morphology simulations have demonstrated that if the nanoparticles present good wettability in the monomer phase, they can be encapsulated in monomer nanodroplets and hence hybrid latexes with encapsulated morphology can be produced [51].

The approach presented here to produce waterborne acrylic/CeO₂ nanocomposite dispersions uses a two-step seeded semibatch (mini)emulsion polymerization process. The approach is well suited to produce hybrid latexes with CeO₂ contents spanning between 0.5 and 5 wt% based on the polymer [52, 53]. In the first step, hybrid seed particles are synthesized by batch miniemulsion polymerization. In the second step the solids content and the final concentration of the CeO₂ nanoparticles can be tuned by controlling the composition of the feed of the semibatch process. Two feeding strategies can be used:

- (i) Neat monomer preemulsion feeding. A preemulsion is fed containing monomers, emulsifier and water, to grow the already formed seed hybrid particles. In this case, all the CeO₂ nanoparticles present in the final hybrid are only added in the seed prepared in the first step. Hybrid latexes with 40–50% solids content were synthesized [53, 54] with CeO₂ contents up to 1 wt% in the final hybrid composite.

- (ii) Hybrid monomer/CeO₂ miniemulsion feeding. The same formulation of the miniemulsion used to synthesize the seed is used as feed allowing higher concentration of CeO₂ in the final latex. Hybrid latexes with CeO₂ contents up to 5 wt% were obtained at 40% of solids content [55].

Figure 1 presents the transmission electron microscopy (TEM) images of relevant latexes with low (1 wt%) and high (5 wt%) content of CeO₂ nanoparticles produced using the two feeding strategies discussed above, respectively. As it can be seen, the polymer particle size

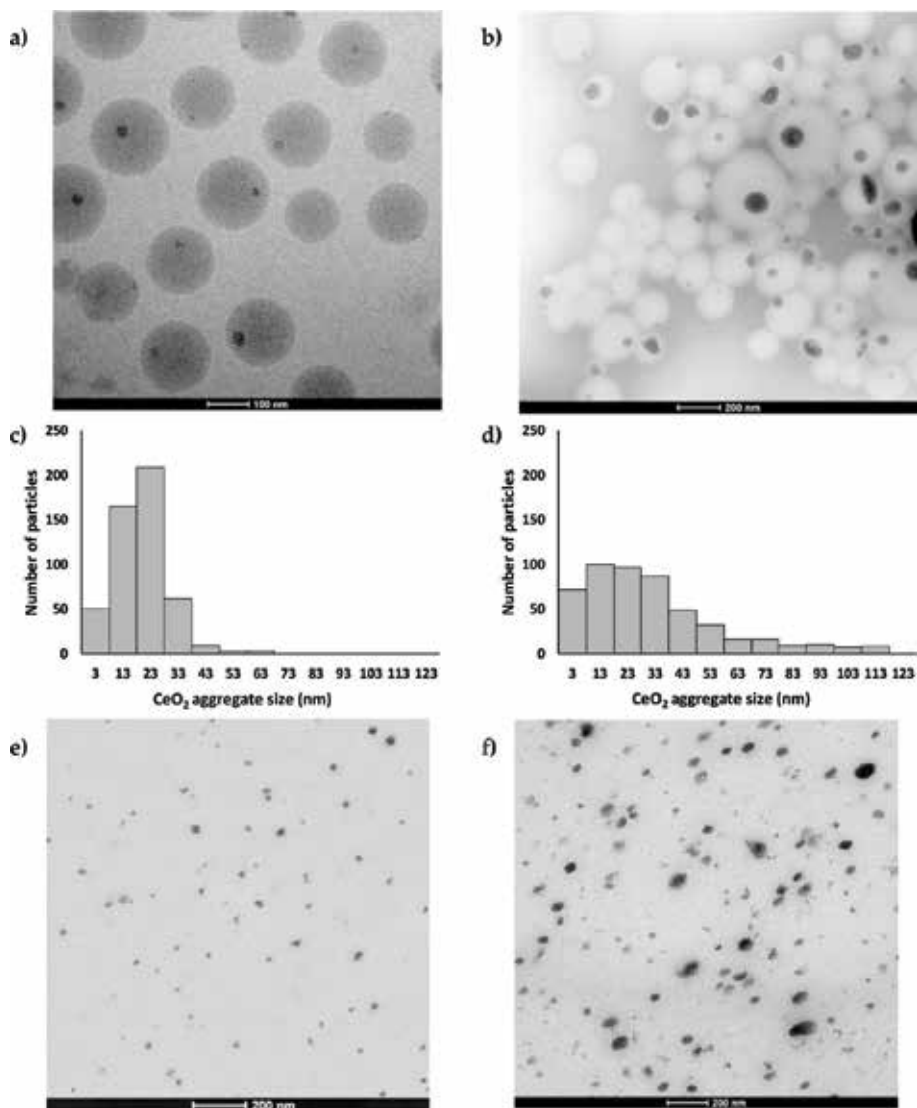


Figure 1. (a) Cryo-TEM image and (b) TEM image of the latexes, (c) and (d) CeO₂ aggregate size distributions in the hybrid latex and (e) and (f) TEM of the hybrid films for the sample containing 1% CeO₂ and 40% SC produced by neat monomer preemulsion feeding strategy (a,c,e) and for the sample containing 5% CeO₂ and 40% SC synthesized using the hybrid miniemulsion feeding (b,d,f).

distribution (PSD) obtained by both feeding strategies is different. Even if the PSD obtained for the hybrid seed is the same for both cases, with particles around 100 nm, the final PSD differs depending on the feeding strategy. When neat monomer preemulsion is fed (**Figure 1a**) the final PSD is narrow, suggesting lack of secondary nucleation during the semibatch process. Nevertheless, the PSD obtained when feeding the miniemulsion (second strategy) is broader, as particles between 25 and 600 nm can be found (**Figure 1b**). This is related to the miniemulsion stability and to the monomer droplet nucleation efficiency in the reactor. According to Rodriguez et al., the nucleation efficiency in a seeded semibatch miniemulsion polymerization is related to the stability of the miniemulsion fed (the higher the stability, the higher the nucleation of the entering droplets), and also to the ratio of the number of entering droplets with respect to the number of particles in the seed (the higher this ratio, the higher the number of fed droplets nucleate because their efficiency for capturing radical is higher) [56]. In **Figure 1b**, very small polymer particles can be seen containing nanoceria, which is an indication that hybrid monomer droplets serve as monomer reservoirs when they enter into the reactor, but they do not lose their identity and finally they end up nucleating [55, 57].

In any case, the CeO₂ nanoparticles (darker spots) are all present in the polymer particles in both cases (**Figure 1a** and **b**), and no one is present in the continuous water phase. It can be seen that the CeO₂ nanoparticles aggregates are more centered in the polymer particles synthesized using the first strategy whereas they are more close to the border of the polymer particle in the hybrids synthesized using the second strategy. The difference comes from the feeding strategy used in each case. When the neat monomer preemulsion strategy is used, the monomer entering the reactor in the semicontinuous process covers the hybrid seed particles containing the CeO₂ nanoparticles. However, in the case of the miniemulsion feeding, a large fraction of the entering hybrid droplets nucleates, and hence not all the fed monomer is used to grow the seed particles and as a consequence CeO₂ nanoparticles aggregates are not fully encapsulated.

Nevertheless, the encapsulation of inorganic nanoparticles inside polymer particles cannot be proved just by TEM images, as sometimes the micrographs are not conclusive enough. Therefore, TEM Tomography studies were carried out to a representative area of the hybrid latexes prepared following the seeded semibatch (mini)emulsion strategy presented so far. The results demonstrated that the CeO₂ nanoparticles were surrounded by polymer in all directions in both, the seed and the final polymer particles, demonstrating beyond any doubt the encapsulated morphology [54].

Furthermore, it is remarkable that every polymer particle contains one CeO₂ nanoparticle aggregate in average. In **Figure 1a** and **b** it can be seen that the number of polymer particles with zero, two and three nanoparticles is very small. It is observed that the CeO₂ aggregate size increases with the nanoceria content in the formulation of the hybrid nanocomposite; namely, the higher the CeO₂ content, the larger the aggregates. **Figure 1c** and **d** presents the quantification of the CeO₂ aggregate sizes in the hybrid latexes containing 1 and 5% of CeO₂ nanoparticles. As it can be seen, aggregate sizes between 3 and 73 nm can be found for the hybrid latex containing 1% of CeO₂ nanoparticles, whereas aggregate sizes between 3 and 123 nm can be found for the nanocomposite containing 5% of CeO₂ nanoparticles. Volume average aggregate sizes are 26 and 50 nm, respectively. However, it should be mentioned that the initial average size of the CeO₂ nanoparticles dispersed in the monomer mixture was 12 nm (measured by

dynamic light scattering). Therefore, it seems that all the nanoparticles present in each monomer droplet aggregate during the first stages of the polymerization process to form a CeO₂ aggregate per polymer particle. This effect will be discussed deeply in the following section.

One of the main advantages of having inorganic nanoparticles encapsulated in polymer particles is the lack of agglomeration during the film formation process, obtaining homogeneous distribution of the nanoparticles in the polymeric film and avoiding their leaching during the lifetime of the coating. **Figure 1e** and **f** show the hybrid films obtained after drying hybrid latexes with 1 and 5% of CeO₂ nanoparticles. It can be seen that after film formation the nanocerium aggregates are homogeneously dispersed in the polymer matrix in both cases. The average CeO₂ aggregate size was also analyzed and it was found that the average size in volume of the CeO₂ nanoparticles in the film is 26 nm for the film containing 1% of CeO₂ and 46 nm for the film with 5% of CeO₂. Therefore, the average size of the CeO₂ aggregates does not change during the film formation process in which the polymer particles coalesce between them, indicating that the encapsulation is an efficient method to avoid the agglomeration of the inorganic nanoparticles in the final film.

3. Evolution of particle morphology during the synthesis of acrylic/CeO₂ hybrid nanocomposites synthesized by miniemulsion polymerization

The morphology obtained in a hybrid nanocomposite may affect directly the final application of the composite material as it has been shown in Section 1 of this chapter. The particle morphology will develop during the polymerization and the final particle morphology will be determined by the interplay of thermodynamics and kinetics. The equilibrium morphology is the one that minimizes the total interfacial energy (θ) of the system, for an organic/inorganic system being the organic phase polymer (monomer), and it is given by:

$$\theta = A_{PW} \cdot \gamma_{PW} + A_{IW} \cdot \gamma_{IW} + A_{IP} \cdot \gamma_{IP} + A_{II} \cdot \gamma_{II} \quad (1)$$

where, A_{ij} and γ_{ij} are the interfacial area and interfacial tensions respectively, between phase i and j , where P, I and W are polymer (monomer), inorganic material, and aqueous phase, respectively. In this particular case the CeO₂ inorganic nanoparticles were previously modified in order to make them hydrophobic and more compatible with the monomers, so the interfacial tension γ_{II} should be very low because when the inorganic particles come into contact, the contact occurs between the same hydrophobic materials. Neglecting γ_{IW} Eq. (1) reduces to an equation that has the same mathematical form that the equation used to calculate equilibrium morphologies of two phase polymer-polymer systems [58–60]. Using the morphology map developed in these studies, Asua showed a similar one (see **Figure 2**) adapted to a polymer/inorganic system [61], where the gray phase represents the inorganic material and the white the polymer (monomer).

According to this morphology map presented in **Figure 2**, the possible equilibrium morphologies that can be obtained in a polymer/inorganic hybrid nanocomposite are core-shell

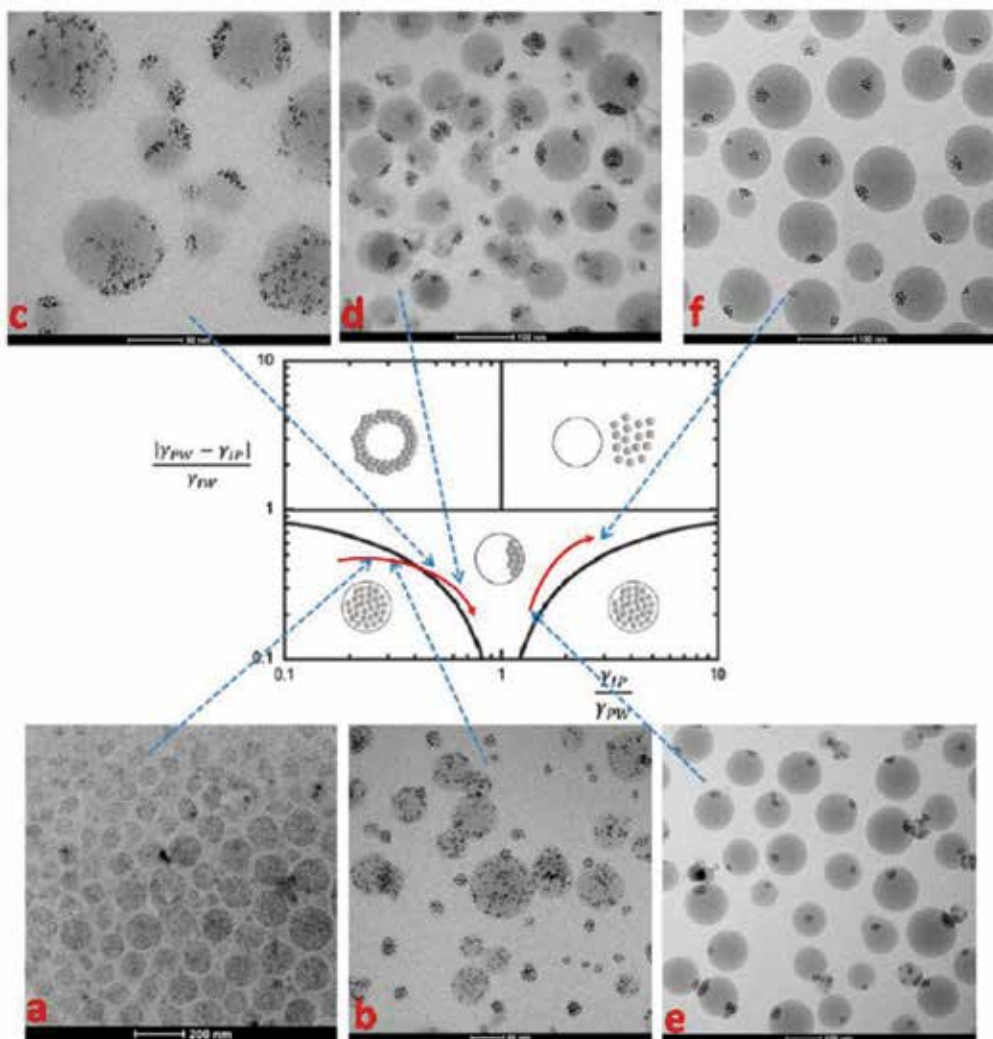


Figure 2. Morphology map and evolution of the particle morphology for (a) acrylic/CeO₂ monomer droplets, (b) 1% monomer conversion, (c) 8% monomer conversion, (d) 18% monomer conversion, (e) 40% monomer conversion, and (f) 100% conversion. Reprinted from [67] with permission from ACS Publications.

(encapsulated), inverted core-shell, hemispherical or separated particles. During the miniemulsion polymerization, the system and thus, the composition of the monomer droplets, are changing as polymerization proceeds. The monomer becomes polymer, initiator or other compounds may incorporate into the polymer and grafting might occur between the polymer being formed and the inorganic material. All these factors will alter the interfacial tensions between the phases and hence, the final equilibrium morphology. In this way, it would be possible to shift from encapsulated morphologies in the initial miniemulsion to hemispherical or separated phases after polymerization. There are some examples in the literature in which the initiator type [62, 63], emulsifier amount [64] and monomer type [65] variations affected strongly the final particle morphology.

In order to analyze the effect that polymerization may have on the morphology of the system described in this chapter, the evolution of the acrylic/CeO₂ nanocomposite is followed during the polymerization process (the hybrid seed preparation by batch miniemulsion polymerization) by cryo-TEM, analyzing samples withdrawn from the reactor at different monomer conversion, and the morphology map (**Figure 2**) is used as a reference to explain the different morphologies obtained, even if some of the morphologies presented are not at equilibrium. It can be observed that at the beginning in the miniemulsion, the CeO₂ nanoparticles are well dispersed in the monomer droplets (**Figure 2a**). This means that the compatibility of the nanocerium with the monomer mixture is really good in the monomer droplets or in other words, that the interfacial tension between the acrylic monomers and the inorganic material, γ_{IP} is low and the interfacial tension between the CeO₂ nanoparticles and water, γ_{IW} is high. This morphology is presented by the core-shell morphology on the left side where $\gamma_{IP}/\gamma_{PW} < 1$ and $|\gamma_{PW} - \gamma_{IP}|/\gamma_{IW} < 1$. It should be mentioned that the nanoparticles are sterically stabilized by the hydrophobic modification they bear in the monomer droplets.

In **Figure 2b** the acrylic/CeO₂ nanocomposite system at 1% of conversion is shown. The morphology observed is completely different, as the nanoparticles tend to aggregate, which means that the incompatibility between the newly formed polymer and the surface of the CeO₂ nanoparticles has increased or that γ_{IP} has become higher. This change in the morphology with the presence of polymer is observed too when the acrylic/CeO₂ hybrid miniemulsion is prepared adding a polymer in order to increase the stability of the miniemulsion [66]. At 8% of conversion, the difference becomes more evident, the nanoparticles are more aggregated and they tend to move towards the border of the polymer particles. The fraction of the polymer increases and thus, γ_{IP} increases. This way, the equilibrium morphology evolves following the red arrow crossing to the hemispherical region as shown in **Figure 2**. At 18 and 40% of conversion the CeO₂ aggregates are more compact and most of the aggregates are situated in the border of the polymer particle (equilibrium position). It should be mentioned that all these morphologies are not at equilibrium, since more than one nanocerium aggregate can be found in the polymer particles. However, when full conversion is achieved, one single aggregate can be seen in each polymer particle, which corresponds to the hemispherical equilibrium morphology.

In the literature there are some mathematical models to predict equilibrium morphologies of hybrid systems [51, 59, 61]. However, these models are not enough to explain the evolution of the acrylic/CeO₂ hybrid nanocomposites, since equilibrium morphology is not obtained until 40% of conversion is reached. Recently, Hamzelou et al. [67] developed a mathematical model for the dynamic evolution of this particular nanocomposite system. This approach provides the distribution of particle morphologies in the whole population of polymer particles. The distribution of particle morphologies is described by a distribution of clusters of CeO₂ nanoparticles (aggregates) dispersed in the monomer phase (see **Figure 3**). According to their position in the particles, the clusters are divided into two different categories: those at equilibrium positions (red dashed line in **Figure 3**) and clusters at non-equilibrium positions (blue line in **Figure 3**). Thermodynamics are used to calculate the equilibrium morphology and all relevant kinetic events of the system including cluster nucleation, polymerization, polymer diffusion and cluster aggregation are taken into account. **Figure 3** shows the simulated weight distributions for the CeO₂ aggregates (clusters). It is shown that at 1% of conversion, most of the nanocerium aggregates are in nonequilibrium positions. At 18% of conversion, most of

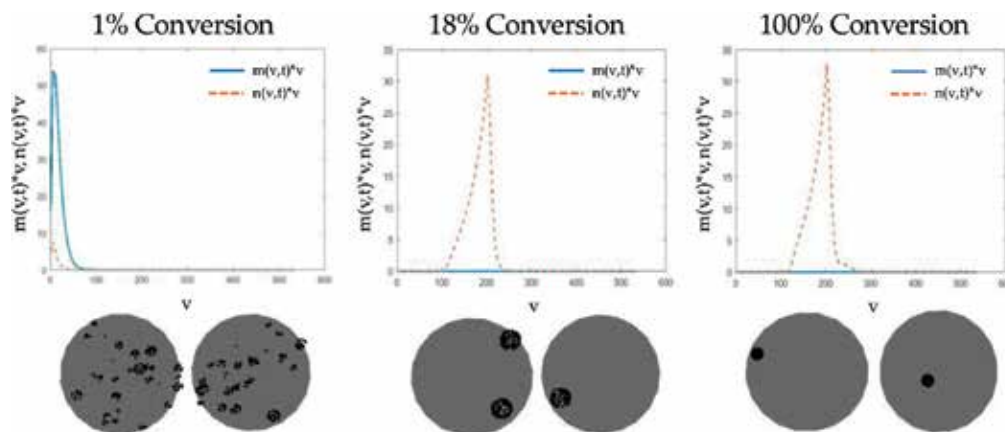


Figure 3. Simulated weight distributions (m and n represent aggregates in non-equilibrium and equilibrium positions, respectively) and the TEM-like images obtained from the distributions. Reprinted from [67] with permission from ACS Publications.

the aggregates are at equilibrium, however, in some of the polymer particles more than one aggregate can be found. At 100% conversion all the nanoceria aggregates are in equilibrium. TEM-like images are generated and they can be compared to the cryo-TEM images presented in **Figure 2**. It can be seen that CeO₂ nanoparticles aggregates follow the same evolution in the experimental cryo-TEM images and in the TEM-like images generated from the model.

To summarize, the morphology evolution of the whole acrylic/CeO₂ nanocomposite is as follows. During the first step, homogeneous distribution of the CeO₂ nanoparticles in the monomer droplets is obtained in the hybrid miniemulsion. During the miniemulsion polymerization, the CeO₂ nanoparticles aggregate and migrate to the surface of the polymer particles. Up to 40% of conversion, the concentration of monomer is high enough and the nanoparticles are able to move inside the monomer droplets towards equilibrium positions. Thus, the nanoceria aggregates are at the edge of the polymer particles, mostly surrounded by polymer, but not always encapsulated [66]. During the second step (neat monomer feeding), the migration of the CeO₂ aggregates is constrained due to the high internal viscosity of the particles. The monomer feeding is done under starved conditions and thus, the seed hybrid particles are covered by a shell of polymer leading to an encapsulated morphology. The proposed mechanism is graphically described in **Figure 4**.

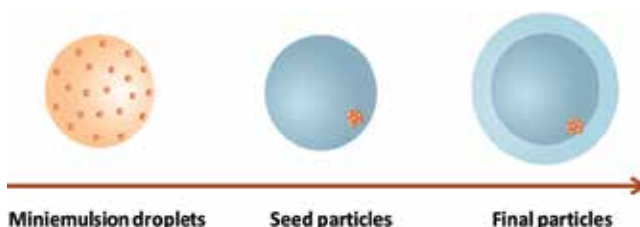


Figure 4. Schematic representation of the morphology evolution of the acrylic/CeO₂ nanocomposite system.

4. UV absorption properties of acrylic/CeO₂ hybrid nanocomposites

One of the main reasons to incorporate the CeO₂ nanoparticles into waterborne clear coatings is their excellent UV absorption capacity. This can be assessed by measuring the UV absorbance of 50 μm thick hybrid films. It should be mentioned that all the hybrid films are transparent and yellowish (Figure 5). The color of the films increases with the CeO₂ nanoparticle content from 1 to 5 wt% and hence, the transparency decreases. Even if the dispersion of the nanoparticles is good in all the hybrid films, the large sizes measured for the hybrid film containing 5% of CeO₂ nanoparticle affect the transparency.



Figure 5. Picture of films cast at room temperature for different CeO₂ loadings: (a) 0% CeO₂, (b) 1% CeO₂ and (c) 5% CeO₂.

Figure 6 shows that the UV absorption of the hybrid films is higher in the presence of the nanocerium in the whole spectrum range (250–600 nm), but the absorption enhancement is most noticeable above 300 nm, where the pristine copolymer absorption is negligible. Furthermore, the higher the amount of CeO₂ nanoparticles, the higher the absorption. However, scattering is observed for the film containing 5% of CeO₂ nanoparticles due to the large size of aggregates obtained for this nanocomposite.

Photodegradation of the hybrid film is a major concern due to the photocatalytic activity of the CeO₂ nanoparticles. In the literature, the photodegradation of hybrid acrylic coatings has been studied in different substrates such as glass, stone or wood [68–71]. In these cases, the hybrid film was tested in a substrate and there might be two sources of radicals. One coming from the substrate and the other one from the nanoparticles present in the polymer matrix. To skip this problem the degradation behavior of the bare acrylic/CeO₂ hybrid films was analyzed. Accelerated weathering tests were conducted in a solar box, for the nanocomposite film without nanoparticles and for the one containing 1% of CeO₂. Different properties of the hybrid films exposed to UV light were measured [72]. Thermal properties reveal one step thermal degradation (around 380°C) and negligible changes in the glass transition temperature (T_g) values for all the hybrid films before and after the exposure. Regarding the microstructure, molecular weight distributions (MWD) and the formation of cross-linked or gel structures were also analyzed. The results show that there is degradation of the polymeric film since the cross-linked fraction increases in the films, but there is no additional effect in the films containing metal oxide nanoparticles. On the other hand, neither the Fourier Transform Infrared Spectra (FTIR) nor the TEM micrographs show any significant difference in the films. It is therefore concluded that the possible photodegradation that CeO₂ nanoparticles may produce in the bare hybrid films is negligible, owing to the similar properties obtained for the blank film and the hybrid film containing 1% CeO₂ nanoparticles after the UV irradiation.

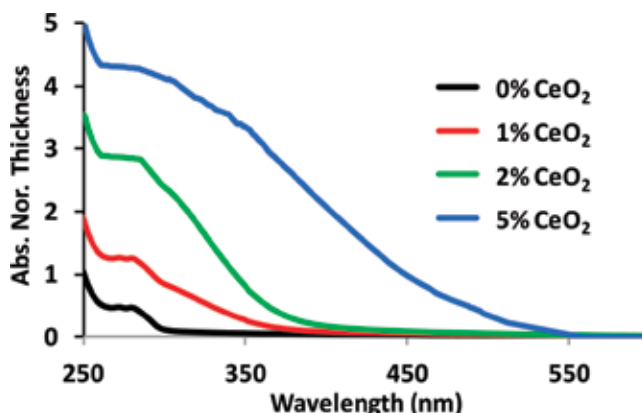


Figure 6. UV-vis absorption capacity of 50 μm hybrid films.

To study the effect of different metal oxides nanoparticles, a nanocomposite film with 1% ZnO nanoparticles was also synthesized following the same seeded semibatch polymerization approach as described in Section 2 [34]. The morphology obtained in the final hybrid films was different to that obtained for the CeO₂ hybrid films. The ZnO nanoparticles aggregate sizes were much bigger (~75 nm), preventing the homogeneous distribution of the nanoparticles in the film. However, the acrylic/ ZnO hybrid films presented higher UV absorption above 350 nm than the counterpart hybrids with CeO₂. In the photodegradation studies carried out in the work mentioned above [72], even if it is known that the photocatalytic activity of the ZnO is larger than that of the CeO₂, as it was mentioned in the introduction, the behavior of the hybrid films containing both types of nanoparticles did not differ significantly.

5. Conclusions and future perspectives

A polymerization strategy to synthesize waterborne hybrid acrylic/CeO₂ nanocomposites for their application as UV blocking coatings has been discussed in this Chapter. The designed two-step polymerization approach is able to produce different loadings of CeO₂ nanoparticles with industrially relevant solids content. Moreover, the strategy ensures the encapsulation of the nanoparticles in the polymer particles that avoids agglomeration during film formation process and provides good UV absorption properties, making these coatings good candidates as clear coats for outdoor applications. A mathematical model developed to predict the evolution of the particle morphology for polymer-polymer systems has been applied for the polymer-CeO₂ hybrids and it is able to predict the evolution of the morphology of the two stage semicontinuous polymerization opening the door to the use of the model for optimization and control of waterborne polymer-inorganic particle morphology purposes.

The designed strategy opens the possibility to encapsulate other nanoparticles and extend the application region. The incorporation of hydrophobically modified ZnO nanoparticles has also been tested, providing film forming hybrid latexes with improved UV absorption capacity [73]. Moreover, with the incorporation of a fluorinated monomer to the acrylic/ZnO hybrid system,

anticorrosion properties have been improved. It was demonstrated that the incorporation of the ZnO nanoparticles by blending was not enough to improve the corrosion protection, whereas when the nanoparticles were encapsulated and hence, well distributed in the polymeric film, the benefits were substantial [74]. Recently, many authors' investigation has been directed to improve anticorrosion properties with the incorporation of CeO₂ nanoparticles. For instance, polyurethane coatings containing CNT/CeO₂ [10], polyacrylic acid/CeO₂ coatings [11], CeO₂/graphene-epoxy nanocomposite coatings [12] and water based polyurethane/ CeO₂ coatings [13]. None of these works obtained encapsulated morphology and hence, the possible aggregation of the nanoparticles during film formation and leaching could be a problem, even though the anticorrosion properties were improved in all the cases. This means that combining the strategy developed in this work, with the appropriate monomers and the anticorrosion properties that CeO₂ nanoparticles exhibit in all the works mentioned above, synergetic effects could be obtained making these nanocomposites ideal candidates for corrosion protection.

Very recently, De San Luis et al. [75] incorporated quantum dots into core-shell particles made of polystyrene/divinyl benzene (DVB) as core and PMMA/DVB as shell. The cross-linked polymeric phases were synthesized in two stages following the strategy developed in this Chapter. Thanks to the encapsulated morphology obtained, the fluorescence emission of the QD containing core-shell particles was preserved for more time than any other work published so far. The same authors incorporated CeO₂ nanoparticles obtaining PS/QD/CeO₂/PMMA hybrid particles. Interestingly, the films casted from these hybrid particles exhibit increasing fluorescence under sunlight exposure [76]. This opens the possibility to use CeO₂ nanoparticles to enhance the optical properties of different technological devices.

Acknowledgements

Financial support from the Basque Government ELKARTEK KK-2016/00030 and KK-2017/00089 is greatly acknowledged. Miren Aguirre thanks the financial support given by the European Union (Woodlife project FP7-NMP-2009-SMALL-246434), the UPV/EHU (2984/2014) "Doktore berriak kontratatze eta horiek doktorego ondoko prestakuntza programetan sartzeko laguntza" and also the financial support received from Ministerio de Economía y Competitividad de España, Juan de la Cierva en Formación (FJCI-2014-22336). The SGIker UPV/EHU for the electron microscopy facilities of the Gipuzkoa unit is acknowledged. Programa de Grupos Consolidados from the Basque Government (IT999-16) is also gratefully acknowledged.

Author details

Miren Aguirre*, María Paulis and Jose R. Leiza

*Address all correspondence to: miren.aguirre@ehu.eus

POLYMAT and Kimika Aplikatua Saila, Kimika Zientzien Fakultatea, University of the Basque Country UPV/EHU, Donostia-San Sebastián, Spain

References

- [1] Yamaguchi I, Watanabe M, Shinagawa T, Chigane M, Inaba M, Tasaka A, et al. Preparation of core/shell and hollow nanostructures of cerium oxide by electrodeposition on a polystyrene sphere template. *ACS Applied Materials & Interfaces*. 2009;**1**(5):1070-1075
- [2] Fischer V, Lieberwirth I, Jakob G, Landfester K, Muñoz-Espí R. Metal oxide/polymer hybrid nanoparticles with versatile functionality prepared by controlled surface crystallization. *Advanced Functional Materials*. 2013;**23**:451-466
- [3] Mari M, Müller B, Landfester K, Muñoz-Espí R. Ceria/polymer hybrid nanoparticles as efficient catalysts for the hydration of nitriles to amides. *ACS*. 2015;**7**(20):10727-10733
- [4] Anjana PS, Deepu V, Uma S, Mohanan P, Philip J, Sebastian MT. Dielectric, thermal, and mechanical properties of CeO₂-filled HDPE composites for microwave substrate applications. *Journal of Polymer Science Part B: Polymer Physics*. 2010;**48**(9):998-1008
- [5] Chen Y, Mu W, Lu J. Young's modulus of PS/CeO₂ composite with core/shell structure microspheres measured using atomic force microscopy. *Journal of Nanoparticle Research*. 2012;**14**(2):696
- [6] Hu J, Zhou Y, He M, Yang X. Novel polysiloxane@CeO₂-PMMA hybrid materials for mechanical application. *Materials Letters*. 2014;**116**:150-153
- [7] Ansari AA, Khan MAM, Khan MN, Alrokayan SA, Alhoshan M, Alsalhi MS. Optical and electrical properties of electrochemically deposited polyaniline/CeO₂ hybrid nanocomposite film. *Journal of Semiconductors*. 2011;**32**(4):043001-1-043001-6
- [8] Incel A, Güner T, Parlak O, Demir MM. Null extinction of ceria@silica hybrid particles: Transparent polystyrene composites. *Applied Materials & Interfaces*. 2015;**7**:27539-27546
- [9] Hu J, Zhou Y. The properties of nano (ZnO-CeO₂) polysiloxane core-shell microspheres and their application for fabricating optical diffusers. *Applied Surface Science*. 2016;**365**:166-170
- [10] Kumar AM, Rahman MM, Gasem ZM. A promising nanocomposite from CNTs and nano-ceria: Nanostructured fillers in polyurethane coatings for surface protection. *RSC Advances*. 2015;**5**:63537-63544
- [11] Eduok U, Jossou E, Tiamiyu A, Omale J, Szpunar J. Ceria/acrylic polymer microgel composite: Synthesis, characterization, and anticorrosion application for API 5L X70 substrate in chloride-enriched medium. *Industrial and Engineering Chemistry Research*. 2017;**56**:5586-5597
- [12] Xia W, Zhao J, Wang T, Song L, Gong H, Guo H, et al. Anchoring ceria nanoparticles on graphene oxide and their radical scavenge properties under gamma irradiation environment. *Physical Chemistry Chemical Physics*. 2017;**19**:16785-16794
- [13] Ferrel-Álvarez AC, Domínguez-Crespo MA, Torres-Huerta AM, Cong H, Brachetti-Sibaja SB, López-Oyama AB. Intensification of electrochemical performance of AA7075 aluminum alloys using rare earth. *Polymers (Basel)*. 2017;**9**(178):1-23

- [14] Khan SB, Faisal M, Rahman MM, Jamal A. Exploration of CeO₂ nanoparticles as a chemi-sensor and photo-catalyst for environmental applications. *Science of the Total Environment*. 2011;**409**(15):2987-2992
- [15] Faisal M, Khan SB, Rahman MM, Jamal A, Akhtar K, Abdullah MM. Role of ZnO-CeO₂ nanostructures as a photo-catalyst and chemi-sensor. *Journal of Materials Science and Technology*. 2011;**27**(7):594-600
- [16] Arshad T, Khan SA, Faisal M, Shah Z, Akhtar K, Asiri AM, et al. Cerium based photocatalysts for the degradation of acridine orange in visible light. *Journal of Molecular Liquids*. 2017;**241**:20-26
- [17] Khan SB, Karimov KS, Chani MTS, Asiri AM, Akhtar K, Fatima N. Impedimetric sensing of humidity and temperature using CeO₂-Co₃O₄ nanoparticles in polymer hosts. *Microchimica Acta*. 2015;**182**(11-12):2019-2026
- [18] Marwani HM, Bakhsh EM, Khan SB, Danish EY, Asiri AM. Cerium oxide-cadmium oxide nanomaterial as efficient extractant for yttrium ions. *Journal of Molecular Liquids*. 2018;**269**:252-259
- [19] Katangur P, Patra PK, Warner SB. Nanostructured ultraviolet resistant polymer coatings. *Polymer Degradation and Stability*. 2006;**91**:2437-2442
- [20] Jaroenworoluck A, Sunsaneeyametha W, Kosachan N, Stevens R. Characteristics of silica coated TiO₂ and its UV absorption for sunscreen cosmetic applications. *Surface and Interface Analysis*. 2006;**38**:473-477
- [21] Nagasawa H, Xu J, Kanezashi M, Tsuru T. Atmospheric-pressure plasma-enhanced chemical vapor deposition of UV-shielding TiO₂ coatings on transparent plastics. *Materials Letters*. 2018;**228**:479-481
- [22] Weichelt F, Emmler R, Flyunt R, Beyer E, Buchmeiser MR, Beyer M. ZnO-based UV nanocomposites for wood coatings in outdoor applications. *Macromolecular Materials and Engineering*. Nov. 2010;**295**:130-136
- [23] Zhao H, Li RKY. A study on the photo-degradation of zinc oxide (ZnO) filled polypropylene nanocomposites. *Polymer (Guildf)*. Apr. 2006;**47**(9):3207-3217
- [24] Masui T, Yamamoto M, Sakata T, Mori H, Adachi GY. Synthesis of BN-coated CeO₂ one powder as a new UV blocking material. *The Royal Society of Chemistry*. 2000;**10**:353-357
- [25] Aguirre M, Paulis M, Leiza JR. UV screening clear coats based on encapsulated CeO₂ hybrid latexes. *Journal of Materials Chemistry A*. 2013;**1**(9):287-292
- [26] Althues H, Henle J, Kaskel S. Functional inorganic nanofillers for transparent polymers. *Chemical Society Reviews*. Sep. 2007;**36**(9):1454-1465
- [27] Chiu F-C, Lai C-M. Optical and electrical characterizations of cerium oxide thin films. *Journal of Physics D: Applied Physics*. 2010;**43**(7):075104
- [28] Christensen PA, Dilks A, Egerton TA. Infrared spectroscopic evaluation of the photodegradation of paint. Part I. The UV degradation of acrylic films pigmented with titanium dioxide. *Journal of Materials Science*. 1999;**34**:5689-5700

- [29] Du J, Sun H. Polymer/TiO₂ hybrid vesicles for excellent UV screening and effective encapsulation of antioxidant agents. *ACS Applied Materials & Interfaces*. 2014;**6**(16):13535-13541
- [30] Hu J, Gao Q, Xu L, Zhang M, Xing Z, Guo X, et al. Significant improvement in thermal and UV resistances of UHMWPE fabric through in situ formation of polysiloxane-TiO₂ hybrid layers. *ACS Applied Materials & Interfaces*. 2016;**8**(35):23311-23320
- [31] Hu J, Gao Q, Xu L, Wang M, Zhang M, Zhang K, et al. Functionalization of cotton fabrics with highly durable polysiloxane-TiO₂ hybrid layers: Potential applications for photo-induced water-oil separation, UV shielding, and self-cleaning. *Journal of Materials Chemistry A*. 2018;**6**(14):6085-6095
- [32] Li YQ, Fu SY, Mai YW. Preparation and characterization of transparent ZnO/epoxy nanocomposites with high-UV shielding efficiency. *Polymer*. Mar. 2006;**47**(6):2127-2132
- [33] Lu H, Fei B, Xin JH, Wang R, Li L. Fabrication of UV-blocking nanohybrid coating via miniemulsion polymerization. *Journal of Colloid and Interface Science*. Aug. 2006;**300**(1):111-116
- [34] Aguirre M, Barrado M, Iturrondobeitia M, Okariz A, Guraya T, Paulis M, et al. Film forming hybrid acrylic/ZnO latexes with excellent UV absorption capacity. *Chemical Engineering Journal*. 2015;**270**:300-308
- [35] Wang H, Qiu X, Liu W, Fu F, Yang D. A novel lignin/ZnO hybrid nanocomposite with excellent UV absorption ability and its application in transparent polyurethane coating. *Industrial and Engineering Chemistry Research*. 2017;**56**(39):11133-11141
- [36] Bennett SW, Keller AA. Comparative photoactivity of CeO₂, γ-Fe₂O₃, TiO₂ and ZnO in various aqueous systems. *Applied Catalysis B: Environmental*. Feb. 2011;**102**(3-4):600-607
- [37] Bourgeat-Lami E, Lansalot M. Organic/inorganic composite latexes: The marriage of emulsion polymerization and inorganic chemistry. *Advances in Polymer Science*. 2010;**233**:53-123
- [38] Zgheib N, Putaux JL, Thill A, D'Agosto F, Lansalot M, Bourgeat-Lami E. Stabilization of miniemulsion droplets by cerium oxide nanoparticles: A step toward the elaboration of armored composite latexes. *Langmuir*. 2012;**28**(14):6163-6174
- [39] González-Matheus K, Leal GP, Tollan C, Asua JM. High solids pickering miniemulsion polymerization. *Polymer*. 2013;**54**:6314-6320
- [40] González E, Bonnefond A, Barrado M, Casado Barrasa AM, Asua JM, Leiza JR. Photoactive self-cleaning polymer coatings by TiO₂ nanoparticle pickering miniemulsion polymerization. *Chemical Engineering Journal*. 2015;**281**:209-217
- [41] Bonnefond A, Ibarra M, Gonzalez E, Barrado M, Asua JM, Leiza JR, et al. Photocatalytic and magnetic titanium dioxide/polystyrene/magnetite composite hybrid polymer particles. *Polymer Chemistry*. 2016;**54**:3350-3356
- [42] Hawkett BS, Such CH, Nguyen DN, Farrugia JM, MacKinno OM. Surface polymerization process using RAFT agent for manufacture of polymer-encapsulated particulates. *WO2006037161*; 2006

- [43] Hawkett BS, Such CH, Nguyen DN. Polymer-encapsulated particulate material and interfacial polymerization process using RAFT agent. WO2007112503; 2007
- [44] Garnier J, Warnant J, Lacroix-Desmazes P, Dufils PE, Vinas J, Vanderveken Y, et al. An emulsifier-free RAFT-mediated process for the efficient synthesis of cerium oxide/polymer hybrid latexes. *Macromolecular Rapid Communications*. 2012;**33**(16):1388-1392
- [45] Garnier J, Warnant J, Lacroix-Desmazes P, Dufils PE, Vinas J, Van Herk A. Sulfonated macro-RAFT agents for the surfactant-free synthesis of cerium oxide-based hybrid latexes. *Journal of Colloid and Interface Science*. 2013;**407**:273-281
- [46] Warnant J, Garnier J, van Herk A, Dufils PE, Vinas J, Lacroix-Desmazes P. A CeO₂/PVDC hybrid latex mediated by a phosphonated macro-RAFT agent. *Polymer Chemistry*. 2013;**4**(23):5656-5663
- [47] Zgheib N, Putaux JL, Thill A, Bourgeat-Lami E, D'Agosto F, Lansalot M. Cerium oxide encapsulation by emulsion polymerization using hydrophilic macroRAFT agents. *Polymer Chemistry*. 2013;**4**(3):607
- [48] Weiss CK, Landfester K. Miniemulsion polymerization as a means to encapsulate organic and inorganic materials. *Hybrid Latex Part*. 2010;**233**:185-236
- [49] Asua JM. Challenges for industrialization of miniemulsion polymerization. *Progress in Polymer Science*. 2014;**39**(10):1797-1826
- [50] Paulis M, Asua JM. Knowledge-based production of waterborne hybrid polymer materials. *Macromolecular Reaction Engineering*. 2016;**10**:8-21
- [51] Reyes Y, Paulis M, Leiza JR. Modeling the equilibrium morphology of nanodroplets in the presence of nanofillers. *Journal of Colloid and Interface Science*. 2010;**352**(2):359-365
- [52] Asua JM. Miniemulsion polymerization. *Progress in Polymer Science*. 2002;**27**(7):1283-1346
- [53] Aguirre M, Paulis M, Leiza JR. UV screening clear coats based on encapsulated CeO₂ hybrid latexes. *Journal of Materials Chemistry A*. 2013;**1**:3155
- [54] Aguirre M, Paulis M, Leiza JR, Guraya T, Iturrondobeitia M, Okariz A, et al. High-solids-content hybrid acrylic/CeO₂ latexes with encapsulated morphology assessed by 3D-TEM. *Macromolecular Chemistry and Physics*. 2013;**214**:2157-2164
- [55] Aguirre M, Paulis M, Leiza JR. Particle nucleation and growth in seeded semi-batch miniemulsion polymerization of hybrid CeO₂/acrylic latexes. *Polymer*. 2014;**55**(3):752-761
- [56] Rodríguez R, Barandiaran MJ, Asua JM. Particle nucleation in high solids miniemulsion polymerization. *Macromolecules*. 2007;**40**:5735-5742
- [57] Aguirre M, Barrado M, Paulis M, Leiza JR. (Cryo)-TEM assessment of droplet nucleation efficiency in hybrid acrylic/CeO₂ semibatch miniemulsion polymerization. *Macromolecules*. 2014;**47**(23):8408-8410
- [58] González-Ortiz LJ, Asua JM. Development of particle morphology in emulsion polymerization. I. Cluster dynamics. *Macromolecules*. 1995;**28**:3135-3145

- [59] González-Ortiz LJ, Asua JM. Development of particle morphology in emulsion polymerization. II. Cluster dynamics in reacting systems. *Macromolecules*. 1996;**29**:383-389
- [60] González-Ortiz LJ, Asua JM. Development of particle morphology in emulsion polymerization. III. Cluster nucleation and dynamics in polymerizing systems. *Macromolecules*. 1996;**29**:4520-4527
- [61] Asua JM. Mapping the morphology of polymer-inorganic nanocomposites synthesized by miniemulsion polymerization. *Macromolecular Chemistry and Physics*. 2014;**215**(5): 458-464
- [62] Mori Y, Kawaguchi H. Impact of initiators in preparing magnetic polymer particles by miniemulsion polymerization. *Colloids and Surfaces. B, Biointerfaces*. 2007;**56**(1-2):246-254
- [63] Staudt T, Machado TO, Vogel N, Weiss CK, Araujo PHH, Sayer C, et al. Magnetic polymer/nickel hybrid nanoparticles via miniemulsion polymerization. *Macromolecular Chemistry and Physics*. 2013;**214**:2213-2222
- [64] Gong T, Yang D, Hu J, Yang W, Wang C, Lu JQ. Preparation of monodispersed hybrid nanospheres with high magnetite content from uniform Fe₃O₄ clusters. *Colloids and Surfaces A: Physicochemical and Engineering Aspects*. 2009;**339**:232-239
- [65] Qiao X, Chen MIN, Zhou J, Wu L. Synthesis of raspberry-like silica/polystyrene/silica multilayer hybrid particles via miniemulsion polymerization. *Journal of Polymer Science, Part A: Polymer Chemistry*. 2006;**45**:1028-1037
- [66] Aguirre M, Paulis M, Barrado M, Iturrondobeitia M, Okariz A, Guraya T, et al. Evolution of particle morphology during the synthesis of hybrid acrylic/CeO₂ nanocomposites by miniemulsion polymerization. *Journal of Polymer Science, Part A: Polymer Chemistry*. 2014;**53**:792-799
- [67] Hamzehlou S, Aguirre M, Leiza JR. Dynamics of the particle morphology during the synthesis of waterborne polymer-inorganic hybrids. *Macromolecules*. 2017;**50**:7190-7201
- [68] Lazzari M, Scalarone D, Malucelli G, Chiantore O. Durability of acrylic films from commercial aqueous dispersion: Glass transition temperature and tensile behavior as indexes of photooxidative degradation. *Progress in Organic Coatings*. 2011;**70**(2-3):116-121
- [69] Saha S, Kocaefe D, Krause C, Larouche T. Effect of titania and zinc oxide particles on acrylic polyurethane coating performance. *Progress in Organic Coatings*. 2011;**70**:170-177
- [70] Saha S, Kocaefe D, Boluk Y, Pichette A. Surface degradation of CeO₂ stabilized acrylic polyurethane coated thermally treated jack pine during accelerated weathering. *Applied Surface Science*. 2013;**276**:86-94
- [71] Serra CL, Tulliani JM, Sangermano M. An acrylic latex filled with zinc oxide by miniemulsion polymerization as a protective coating for stones. *Macromolecular Materials and Engineering*. 2014;**299**:1352-1361
- [72] Aguirre M, Goikoetxea M, Alberto L, Paulis M, Leiza JR. Accelerated ageing of hybrid acrylic waterborne coatings containing metal oxide nanoparticles: Effect on the microstructure. *Surface and Coating Technology*. 2017;**321**:484-490

- [73] Aguirre M, Barrado M, Iturrondobeitia M, Okariz A, Guraya T, Paulis M, et al. Film forming hybrid acrylic/ZnO latexes with excellent UV absorption capacity. *Chemical Engineering Journal*. 2015;**270**:300-308
- [74] Chimenti S, Vega JM, Aguirre M, Garcia-Lecina E, Diez JA, Grande H-J, et al. Effective incorporation of ZnO nanoparticles by miniemulsion polymerization in waterborne binders for steel corrosion protection. *Journal of Coatings Technology and Research*. 2017;**14**(4):829-839
- [75] De San Luis A, Bonnefond A, Barrado M, Guraya T, Iturrondobeitia M, Okariz A, et al. Toward the minimization of fluorescence loss in hybrid cross-linked core-shell PS/QD/PMMA nanoparticles: Effect of the shell thickness. *Chemical Engineering Journal*. 2017;**313**:261-269
- [76] Luis ADS, Paulis M, Leiza JR. Co-encapsulation of CdSe/ZnS and CeO₂ nanoparticles in waterborne polymer dispersions: Enhancement of fluorescence emission under sunlight. *Soft Matter*. 2017;**13**(44):8039-8047



Edited by Sher Bahadar Khan and Kalsoom Akhtar

This book focuses on the chemical structure and applications of CeO_2 . It covers the recent developments in a wide range of CeO_2 applications, particularly catalysis corrosion protection, fuel cells, sensors, and UV-blocking. It also provides a concise but thorough coverage of the chemical structure and applications of CeO_2 . Thus, this book provides an overview of chemical structure, applications, and recent attributes of CeO_2 for a broad audience, including beginners, graduate students, and specialists in both academic and industrial sectors.

Published in London, UK

© 2019 IntechOpen
© Mcastrom / iStock

IntechOpen

